STUDIES ON SUPEROXIDE DISMUTASE INHIBITION AND APPLICATION OF METHODS TO STUDY METAL ION PARTICIPATION IN COMPLICATION OF DIABETES

A thesis presented to the faculty of the Graduate School of
Western Carolina University in partial fulfillment of the
requirements for the degree of Masters of Science in Chemistry.

By

Benjamin Hickman

Director: Dr. Jack Summers
Associate Professor of Chemistry
Department of Chemistry and Physics

Committee Members: Dr. Scott Huffman, Dr. Arthur Salido

May 30, 2012

ACKNOWLEDGEMENTS

I would like to thank my committee members and director for their advice and assistance. In particular, Dr. S. Huffman for his help with algorithms used to process spectral data, Dr. Salido for his help with the mass spectrometer and ICP-OES, and Dr. Summers for deciphering my writing and translating it into something more comprehensible.

I would also like to thank Megan Arrington, Mariah Honrnby, Sherri Barborich and others in the Summers Lab who contributed to the Studies on Superoxide Dismutase Inhibition project.

TABLE OF CONTENTS

LIST OF TABLES

Table Page

LIST OF FIGURES

Figure Page

ABSTRACT

STUDIES ON SUPEROXIDE DISMUTASE INHIBITION AND APPLICATION OF METHODS TO STUDY METAL ION PARTICIPATION IN COMPLICATION OF DIABETES

Benjamin Hickman

Western Carolina University (May 2012)

Director: Dr. Jack Summers

Studies on Superoxide Dismutase Inhibition

We used NMR relaxation rates to study reactions of the enzyme superoxide dismutase (SOD) with low molecular weight polyphenolic compounds. While the compounds appeared to inhibit SOD, we discovered evidence that the reaction proceeds with electron transfer from the polyphenols to the enzyme, giving a form of the SOD that was inactive in the assay but retained enzymatic activity. The reaction was highly dependent on the aggregation and protonation states of the compounds.

Application of Methods to Study Metal Ion Participation in Complication of Diabetes

Diabetics display increases in chemical modification of proteins and also increased levels of oxidative stress. Alderson *et al*. reports one of these modifications involves reaction of the

sulfhydryl group of cysteine residues with the Krebs Cycle intermediate fumarate. It has been proposed that the product, S-(2-Succinyl)cysteine (2SC), can bind metals, and may catalyze reactions such as the Haber-Weiss cycle. It is possible that 2SC will catalyze the disproportionation of superoxide. To study the possible link between 2SC and oxidative stress we synthesized two model compounds and studied their reactions. One of these is S-(2-succinyl)-N-acetlycysteine (2SAC). We have shown the 2SAC will bind copper with a stability constant of log(K)= 3.59 ± 0.05. Also we have shown that the compound 2SAC-Cu will catalyze the Haber-Weiss reaction but not the disproportination of superoxide. Furthermore, since glutathione concentrations in vivo can reach up to 10 mM it seems likely that reduced glutathione will react with fumerate to give S-(2-succinyl)-glutathione (2SGT). To study its possible role in vivo, we synthesized 2SGT. For the 2SGT compound, the binding constant of Cu-2SGT was determined to be log(K)=10.9 ± 0.2. Likewise, we have found that 2SGT binds to copper in such a way as to prevent catalysis of further reactions. Our attempts to study the iron complexes for these compounds have been unsuccessful due to their low solubility.

INTRODUCTION

In this thesis two projects are discussed. The first is Studies on Superoxide Dismutase Inhibition and the second being Application of Methods to Study Metal Ion Participation in Complication of Diabetes. The background, experimental methods, and results and discussion are given for the Studies on Superoxide Dismutase Inhibition project, followed by the background, experimental methods, and results and discussion for the Application of Methods to Study Metal Ion Participation in Complication of Diabetes project.

STUDIES ON SUPEROXIDE DISMUTASE INHIBITION

Studies on Superoxide Dismutase Inhibition Background

During natural metabolism, some molecular oxygen is converted to the superoxide radical ($O_2^{\cdot -}$), leading to oxidative stress.[2] This is done by the superoxide radical being converted to the hydroxyl radical ($OH^{\cdot}$) through the Haber-Weiss reaction (equation 1 and 2).[1] Hydroxyl radical is a reactive oxygen species that may react with proteins or nucleic acids to alter or prevent their function, and may eventually lead to cell apoptosis.[2,3]

$$Fe^{3+} + O_2^{\cdot -} \rightarrow Fe^{2+} + O_2 \quad (1)$$

$$Fe^{2+} + H_2O_2 \rightarrow Fe^{3+} + OH^- + OH^{\cdot} \quad (2)$$

The superoxide dismutase (SOD) enzymes catalyze the disproportionation of superoxide radicals. This neutralization occurs via a cyclic redox reaction of a metal in the SOD's active site. When the superoxide radical contacts the metal it is converted into either molecular oxygen or hydrogen peroxide as described in equation 3 and 4.[4]

$$M^{n+} + O_2^{\cdot -} \rightarrow M^{(n-1)+} + O_2 \quad (3)$$

$$M^{(n-1)+} + O_2^{\cdot -} + 2H^+ \rightarrow M^{n+} + H_2O_2 \quad (4)$$

In this study we used bovine CuZn SOD enzyme which has copper and zinc as cofactors. In the CuZn SOD, it is the copper that cycles from its +2 and +1 oxidation states and participates in the redox reaction described above.

Inhibiting the SOD would increase oxidative stress in a cell. For this reason, inhibitors of SOD are of interest as potential anti-cancer and anti-bacterial drugs. Cancer cells have an increased cell metabolism compared to normal cells, causing the oxidative stress to be high.[5] This inherently high oxidative stress level should make cancer cells sensitive to SOD inhibition. Bacterial cells are thought to rely on SOD to survive oxidative burst by immune cells, for this purpose bacterial cells up regulate the production of SOD which should also make them sensitive to SOD inhibition.[6,7]

Huang *et al.* showed in 2000 that the estrogen derivative 2-methoxyestradiol was able to inhibit SOD in leukemia cells.[8] This inhibition was able to kill the leukemia cells while preserving the healthy cells; showing that inhibitors of SOD can be used to selectively target cancer cells.

Traditionally, screening for SOD inhibitors involved the generation and detection of the highly reactive superoxide radical ($O_2^{\cdot}$).[9] These assays produce the superoxide radical via enzymatic (xanthine oxidase) or non-enzymatic (Nicotinamide adenine dinucleotide (NADH)/ Phenazine methosulfate (PMS)) sources in a solution with the SOD and inhibitor(s).[9] A detector molecule such as nitroblue tetrazolium (NBT) or ferricytochrome c is added and then reduced by the reactive superoxide radical. The extent to which the detector molecules are reduced can be measured via UV/Vis spectroscopy indicating how well the inhibitors were able to prevent the neutralization of these superoxide radicals by the SOD.[9] It has been reported that these traditional methods give false positive results due to unwanted interactions between assay components.[8,10] These unwanted interactions can occur by either the intended SOD inhibitors inhibiting the superoxide source or they can themselves react with the superoxide radicals.[8,10]

Vigilino *et al.*[11] showed that the ^{19}F NMR resonance of the fluoride ion ($^{19}F^-$) was highly affected by the presence of small quantities of oxidized (Cu^{2+}) form of SOD (as low as 10^{-7} M

SOD).[11] This effect on the fluoride ion resonance results when the fluoride coordinates with paramagnetic copper in the SOD's active site. Since the superoxide radical also coordinates copper in the SOD's active site in the disproportionation reaction, the fluoride ion makes a good probe to model the superoxide radical.[12] By observing the fluoride NMR signal in the presence of SOD, it should be possible to determine whether access to SOD's active site is blocked by an inhibitor. However, this assay will break down if the copper in the active site dos not remain in the paramagnetic form (Cu^{2+}) since the diamagnetic form (Cu^{1+}) does not affect the NMR assay.

From the result of Huang *et al.* Dr. Summers's group decided to look at phytoestrogens for anti-SOD activity. Previously our group looked at a number of phytoestrogens and found that some molecules from the class of flavonols showed apparent SOD inhibition.[26] In this study we used ^{19}F NMR to study apparent anti-SOD activity by a selection of flavonols. From apparent inhibition data we developed a structure-activity relationship (SAR) for the flavonols. Computational work was performed in an attempt to rationalize the SAR developed from the flavonol inhibition data. From the SAR developed using the falvonols we found other small phenolic molecules that also displayed apparent anti-SOD behavior. However further studies on these compounds show that inhibition is not occurring. Rather, a redox reaction occurs between the polyphenols and the copper cofactor in the SOD.

Superoxide Dismutase Inhibition Experimental

Inhibition determined by $^{19}F^-$ NMR. Apparent SOD inhibition was characterized by monitoring the effects of SOD on the $^{19}F^-$ NMR T_2 relaxation rate of the fluoride ion. The assay

uses the Carr-Purcell- Meiboom- Gill (CPMG) NMR experiment to measure the transverse relaxation rate of the fluoride signal (R_2), which is the inverse of the transverse relaxation time (T_2) (Equation 5). The rate of relaxation for the fluoride ion is given by equation 6. Where I_0 is the initial intensity of the fluoride signal and I_{obs} is the intensity of the fluoride signal after a relaxation delay time, *t*. By taking the natural log of both sides equation 7 is obtained. Using equation 7 the relaxation rate (R_2) is equal to the slope, from lest squares regression, when the natural log of the fluoride signal intensity is plotted as a function of time (Figure 1a and 1b).

$$R_2 = \frac{1}{T_2} \tag{5}$$

$$I_{obs} = I_0 e^{-R_2 t} \tag{6}$$

$$\ln(I_{obs}) = \ln(I_0) - R_2 t \tag{7}$$

When the fluoride contacts the paramagnetic copper it loses coherence with the rest of the fluoride ions. This loss of coherence causes the net fluoride signal to be smaller, giving faster relaxation rate (R_2) compared to solutions without paramagnetic copper, or solutions in which access to the copper is blocked by an inhibitor.

The fraction of SOD that retains NMR activity in an assay can be found using equations 8 and 9. Where $R_{2\ observed}$ is the relaxation of a sample with SOD and inhibitor,

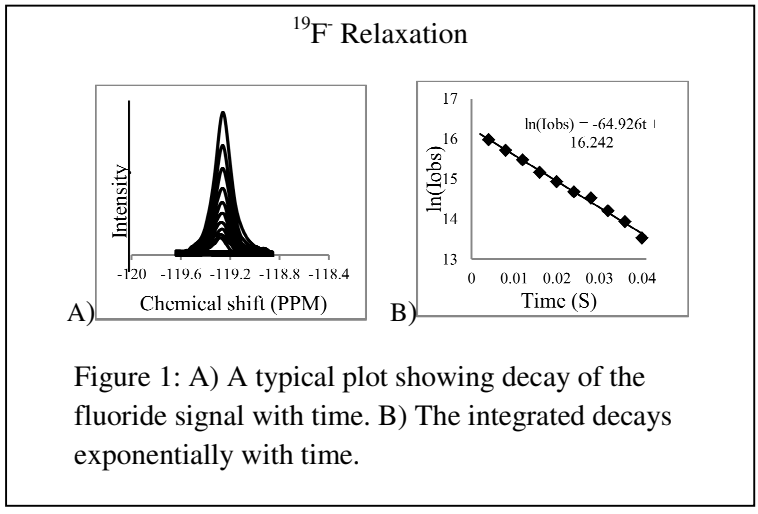

Figure 1: A) A typical plot showing decay of the fluoride signal with time. B) The integrated decays exponentially with time.

$R_{2\ neg.\ control}$ is the relaxation of a sample with no inhibitor or SOD, and $R_{2\ pos.\ control}$ is the relaxation of a sample with SOD but no inhibitor. (Originally, we thought the inactive SOD had an inhibitor bound to the active site. If this were the case, then dissociation constant for an inhibitor is given by equation 10.)

$$1 = \frac{[SOD_{active}] + [SOD_{inactive}]}{[SOD_{total}]} \tag{8}$$

$$[SOD_{active}] = \frac{R_{2\ observed} - R_{2\ neg.control}}{R_{2\ pos.control} - R_{2\ neg.control}} \tag{9}$$

$$K_d = \frac{[SOD_{active}][free\ inhibitor]}{[SOD_{inactive}]} \tag{10}$$

$$\left(\frac{1}{K_d}\right)[inhibitor] = \frac{1}{[SOD_{active}]} - 1 \tag{11}$$

Using equations 9 and 10 equation 11 can be obtained. From equation 11 a plot of $\frac{1}{[SOD_{active}]} - 1$ as a function of inhibitor concentration should be linear, with a slope of $\left(\frac{1}{K_d}\right)$. It should be noted that for the flavonols, these plots typically show curvatures at higher concentrations. We attribute this curvature to aggregation of the inhibitor (discussed later).

Superoxide dismutase. Bovine CuZn SOD was obtained from MP Biomedicals LLC and used without further purification.

$^{19}F^-$ NMR buffers. Buffers were chosen depending on the desired pH. Table 1 show a list of buffers used. Buffer solutions were made to contain 20mM buffer, 20mM sodium fluoride, and

10% by volume deuterium oxide in HPLC water. The buffers were adjusted with minimal amounts of 1N NaOH or HCl to reach the desired pH.

pK_a	Buffer
4.8	Acetate
4.8	Citrate
6.8	Pipes
8.3	Tris
9.6	Glycine
10.7	Triethylamine

Table 1: Buffers used and their pK_as

$^{19}F^-$ NMR controls. 10 μL of DMSO and 490 μL the buffer solution described above was taken for a negative control. To the remaining buffer SOD was added to obtain an R_2 value between 50 and 100 S^{-1} (approximately $2x10^{-8}$ M SOD was required per R_2 value. The amount varied with pH and SOD batch). A 500 μL sample of buffer with SOD was taken for a positive control.

$^{19}F^-$ NMR inhibitor solutions. Inhibitor solutions containing 50 times the desired NMR sample concentration were made in DMSO. NMR samples were made by adding 10 μL of inhibitor solutions to 490 μL of the buffer solution containing SOD; which gives samples containing 2% DMSO and the desired inhibitor concentration.

Computational studies.

Enzyme structure energy minimization. From the Protein Data Bank, the 1PU0 CuZn SOD crystal structure was downloaded into MOE. The first monomer of the 5 dimer aggregate was isolated, and all the residual water molecules were deleted. The structure was then protonated to correspond to a pH of 8 using the protonate 3D application in MOE. The energy of the system was minimized while tethering heavy atoms with a restoring force of 500 in the energy minimize application of MOE. The partial charges of the atoms were calculated with the partial charge calculate application of MOE.

Moe flavonol-SOD docking simulation. The flavonols (Table 4) were built in MOE, and put into a database (the flavonols were deprotonated at the 4' position to correspond to a pH of 8). The structures of the flavonols were adjusted to minimize their energy using the energy minimize application.

The active site of the SOD was selected to be the residues within approximately 12 Å of the copper atom (this was done because the length of a flavonol is about 12 Å). The flavonols were then docked to the selected active site using the Triangle Matcher placement method. The docked poses were then energy minimized using the Force Field minimization option in MOE. The binding energies of the energy minimized poses were then scored using the London DG scoring method. Each of the poses was put into a database containing the 3D structures and the resulting binding scores.

MOE SOD dynamics simulation. Starting from the energy minimized structure the MOE dynamics application was then used to simulate molecular movement for ten nanoseconds. During the simulation volume and temperature were held constant at 43557 Å and 300 K respectively. A molecular file of the enzyme was collected every ten picosecond and stored in a database.

MOE simulation of flavonol/SOD chelate interactions. Flavonols were fit into the active site of the energy minimized SOD so that the 3' and 4' hydroxyl groups could chelate to the copper atom. The 3' and 4' hydroxyls were then fixed so that they would not move during an

energy minimization. The energy of the system was then minimized, and the binding energy was noted.

Flavonol fluorescence. Buffer solutions were prepared using 20 mM Tris in HPLC water, and adjusted to pH 8 using 1M NaOH. Flavonols were dissolved in a minimal amount of buffer, which varied with the solubility of the flavonols. A dilution using buffer was performed to obtain a 512 μM flavonol solution. Nine 1:2 serial dilutions of flavonols were performed starting at 512 μM and going down to 1 μM. Fluorescence spectra of the flavonol solutions were obtained using a Perkins Elmer LS 55 Luminescence Spectrometer.

Principal component analysis of flavonol fluorescence data. Using Matlab2011a, the fluorescence data for each of the flavonols were loaded into a matrix. The matrix was arranged into *n* rows and *m* columns, where *n* is the number of spectra and *m* is the spectral intensity at each wavelength. The principal component analysis was done using a matlab code developed by Dr. S. Huffman of Western Carolina University (Appendix A).

Gallic ester synthesis. Gallic acid and five pentyl alcohol isomers (3-methyl-2-butyl, neopentyl, isoamyl, 2-methyl-1-butyl, 1-pentyl, 3-pentyl alcohol) were obtained from Acros Organics and used without further purification. To a 10 mL tear drop flask, approximately 0.1 g of gallic acid was added. To this flask approximately 2 mL of the desired alcohol was added with a magnetic stir bar and gently stirred. An equal molar amount (relative to gallic acid) of concentrated sulfuric acid was added drop wise. A condenser was fitted to flask and the solution was heated until the gallic acid dissolved and refluxed for 2-3 hours. Upon reaction, the solution

changed from colorless to pale yellow for each ester. Approximately 90 percent of the excess alcohol was evaporated off using a rotovap. Solutions were not evaporated to dryness so as not to over-concentrate the sulfuric acid. The remaining solution was transferred into a separatory funnel using a minimal amount of ethyl acetate. Saturated sodium bicarbonate was added until the pH was neutral (pK_{a1} of the esters is about 8) and then separated from the organic layer. The organic layer was then washed 2 times with deionized water. Then the organic layer was transferred to a round bottom flask and the ethyl acetate was rotovaped off. The remaining crude product was evacuated overnight to remove residual alcohol starting material. Samples were characterized by ^{1}H NMR (Table 2)

Ester	^{1}H NMR chemical shift (ppm) ($DMSO_{d6}$), multiplicity, integration
3-methyl-2-butyl gallate	0.90 (d,6H), 1.20 (d, 3H), 1.80 (m,1H), 4.85 (m, 1H)
Neopentyl Gallate	0.95 (s, 9H), 3.87 (S, 2H)
Isoamyl gallate	0.90 (d, 6H), 1.55 (q, 2H), 1.75 (m, 1H), 4.20 (t, 2H)
2-methyl-1-butyl gallate	0.90 (m, 6H), 1.20 (m, 1H), 1.45 (m, 1H), 1.75 (m, 1H), 4.05 (m, 2H)
1-pentyl gallate	0.92 (t, 3H), 1.40 (m, 4H), 1.72 (m, 2H), 4.25 (t, 2H)
3-pentyl gallate	0.85 (t, 6H), 1.60 (m, 4H), 4.79 (m, 1H)

Table 2: Pentyl gallate esters ^{1}H NMR data.

SOD metal sequestering. To 2 mL glycine buffer (20 mM, pH 10) approximately 4400 units of SOD were added. 1 mL of this buffer/SOD solution was put into an Eppondorf tube with 16.2 μL of a 123 mM methyl 3,4-dihydroxybenzoate (MDHB figure 17) solution in DMSO. To the remaining 1 mL of buffer/SOD 16.2 μL of DMSO was added for a control. The control and MDHB solutions were allowed to equilibrate overnight at room temperature. After equilibration, 500 μL of the MDHB and control solutions were filtered through an YM-10 membrane filtration device (10 KDa molecular weight cutoff) (Millipore). The filtered and unfiltered MDHB and control solutions were each treated with 150 μL of concentrated HNO_3, and dilute with 2.35 mL of HPLC H_2O. Copper concentrations of each solution were found using a Perkins Elmer ICP-OES Optima 4100 DV spectrometer.

Enzyme concentration dependence of inhibition on quercetin. 10 mL of a NMR buffer at pH 8 (prepared as described above for $^{19}F^-$ NMR buffers), 1 mL of a 1.5 mM quercetin in DMSO solution, and a solution containing approximately 4400 units of SOD dissolved in 200 μL of HPLC water were made. NMR samples were prepared containing between 44 and 308 units of SOD (Table 3). Using the control samples (samples A-C), the predicted relaxation rates were extrapolated for the higher concentrations of SOD.

Sample	μL buffer	μL quercetin in DMSO	μL DMSO	μL SOD
A	588	0	12	2
B	588	0	12	4
C	588	0	12	8
D	588	12	0	2
E	588	12	0	4
F	588	12	0	8
G	588	12	0	10
H	588	12	0	12
I	588	12	0	14

Table 3: Solution contents for the enzyme concentration dependence experiment.

SOD redox activity with superoxide and quercetin. A pH 8 NMR buffer was prepared as described above and SOD was added until the sample had an R_2 value of approximately 100 s^{-1}. Two aliquots of this buffer/SOD solution (500 μL) were taken and one was treated with 10 μL of a 1.5 mM quercetin solution in DMSO to give a final quercetin concentration of 30 μM. The other was used as a control. From concentrated stock solutions NADH and PMS were added to the two samples to give final concentrations of 78 and 3.3 μM respectively with a negligible effect on the total volume. The time after the NADH and PMS addition was monitored with a stopwatch. The ^{19}F NMR relaxation rate (R_2) was monitored using the CPMG experiment until it stabilized.

Studies on Superoxide Dismutase Inhibition Results and Discussion

Table 4 shows apparent inhibition data obtained from the ^{19}F NMR assay for a selection of the flavonols.[26] Due to the aggregation of the inhibitors it was not possible to accurately determine K_d for some of the inhibitors. However, IC_{50} values (concentration at which 50% of the SOD is inhibited) are also reported, which can be determined without quantifying the aggregation of the inhibitor (discussed later).

Flavonol	IC_{50} (μM)	Kd (μM)	$Kdim^{-1}$ (μM)	Flavonol	IC_{50} (μM)	Kd (μM)	$Kdim^{-1}$ (μM)
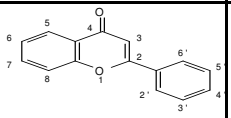 Generic	N/A	N/A	N/A	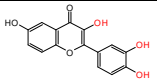 3,6,3‘,4'TetHF	140	10±5	2.0±1.5
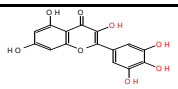 Myricetin	6.7	6.8±1.6	24±6	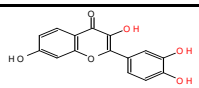 Fisetin[a]	69		
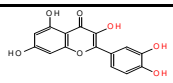 Quercetin	12	12±4	30±15	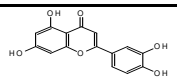 Luteolin[a,b]	>1000		
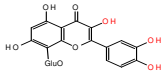 Gossypin	39	13±5	15±6	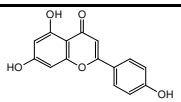 Apigenin[b]	>1000	>200	59
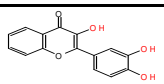 3,3‘,4'TriHF[b]	820	19±5	7±3	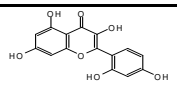 Morin[b]	>1000	>200	330

Table 4: Inhibition and dimerization data of selected flavonols at pH 8.
a) K_{dim} could not be determined accurately from fluorescence data.
b) IC_{50} estimated by extrapolation of reciprocal activity versus $[inh]^{0.5}$ plot.

More recently we found evidence that inhibitors reduce the paramagnetic copper (II) to diamagnetic copper (I) rather than binding to the active site. This appears to be the mechanism by which the compounds inhibit NMR relaxation by the SOD enzyme (discussed later).

Flavonols structure-activity relationship. We found that some flavonols inhibit SOD NMR relaxation while others similar compounds have no activity. All the active flavonols

(defined as one that has an apparent K_d less than 100 μM) had the 3', 4' and 3 position hydroxyl groups present (red hydroxyl groups in Table 4) while flavonols, without all of these groups, showed no activity.

We originally suspected that the 3' and 4' hydroxyl groups participate in inhibition by chelating to the copper. More recent data suggest the 3' and 4' hydroxyl groups may be oxidized to the stable quinone moiety. Flavonols containing catechhol groups have lower oxidation potentials than flavonols lacking this group. This necessity of the 3' and 4' hydroxyl is illustrated by the comparing the activities of morin, apigenin, and quercetin. The structures of morin and quercetin differ in that the 3' hydroxyl group in quercetin is shifted to the 5' position in morin; this shift would prevent morin from chelating (or forming the stable quinone moiety). The effect of this shift in hydroxyl group position is dramatic, causing the apparent inhibition constant of morin to decrease by more than an order of magnitude compared to quercetin. Comparison of apigenin to quercetin shows that apigenin, which has the same structure as quercetin except for the lack of the 3 and 3' hydroxyl group, has a loss in apparent binding affinity nearly an order of magnitude.

Similarly the 3 hydroxyl group is present in all active flavonols. This hydroxyl group might participate in hydrogen bonding to one of the residues in the active site, or might contribute to apparent inhibition by lowering the oxidation potential. The importance of this group is demonstrated in the comparison of luteolin with quercetin. The two compounds are identical except for the 3 hydroxyl group which luteolin does not have. The effect of this additional hydroxyl group can be shown in the comparison of the compounds apparent IC_{50}'s, which again show nearly an order of magnitude difference.

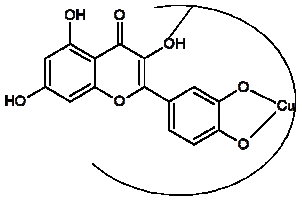

Figure 2: Proposed binding method of active flavonols to SOD's active site.

Myricetin, which has a third hydroxyl group on its B ring, shows the greatest inhibitory activity for the SOD enzyme compared to the other flavonols examined in this study. We suspect this third hydroxyl group participates in hydrogen bonding to a residue in the active site. This increased binding affinity for the gallol moiety over the catechol moiety is also apparent in other smaller molecules (discussed later).

From this structure activity relationship, Dr. Summers proposed that the active flavonols fit into SOD's active site and chelate to the copper with the 3' and 4' hydroxyl groups, and the 3 hydroxyl group binds to a residue as shown in Figure 2.

Flavonol computational work. We used the Molecular Operation Environment (MOE) program from the Chemical Computing Group to dock the nine flavonols shown in Table 4 to the active site of an SOD enzyme (1PU0 from the PDB). The active site used in this study is shown in Figure 3 with a red surface.

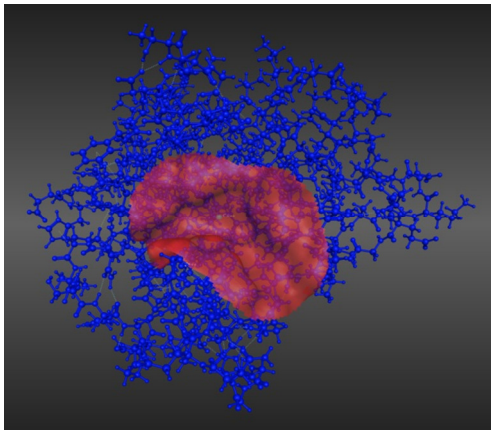

Figure 3: Active site (red) used for the docking simulation of the flavonols.

In the simulation, the nine flavonols in Figure 2, were deprotonated at the 4' position (to correlate to a pH of 8) and docked to the active site of an SOD monomer (red surface in Figure 3). Figure 4 shows typical poses when quercetin is docked to the isolated active site from Figure 3. Almost all the poses had the flavonols bound to residues around the perimeter of the active site. One percent of the docking poses resulted in an interaction with the copper atom in the pocket of the active site.

For each of the docking poses, a binding energy was generated. As shown in Figure 5, the average theoretical binding energies for each of the flavonols did not correlate with the IC_{50} values determined experimentally. This could be due to the MOE generated poses not being representative of the actual way in which the flavonols bind to the enzyme, MOE's algorithm not being designed not handling transition metals, or to active site in the crystal having different geometry than in solution. However, it is likely that the discrepancy in the results is caused by inhibition being due to redox chemistry rather than inhibitor binding.

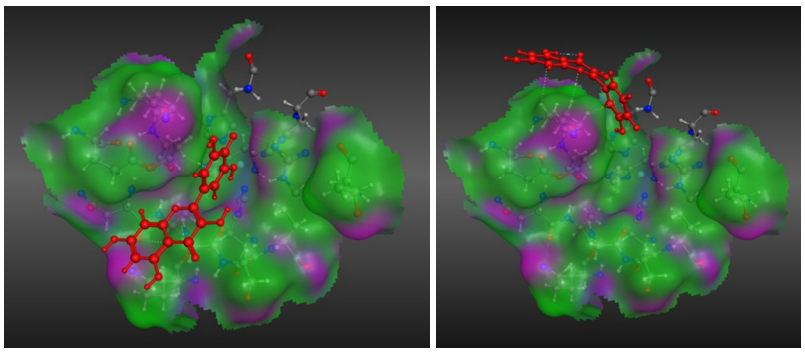

Figure 4: Poses of myricetin (left) and quercetin (right) docked to the active site (red surface from figure 4). The poses show no interaction with the copper atom inside the pocket of the active site.

The difference in the geometry of the active site in the crystal model versus its solution analogue was addressed using the molecular dynamics (MD) simulation in MOE. The simulation examined how freely the atoms of the SOD enzyme are able to move during normal molecular motion. This MD simulation generated poses of the SOD every 10 ps during a 10 ns simulation. From the poses generated, the root mean square distance (RMSD) the atoms moved from their original position was calculated and plotted as a function of

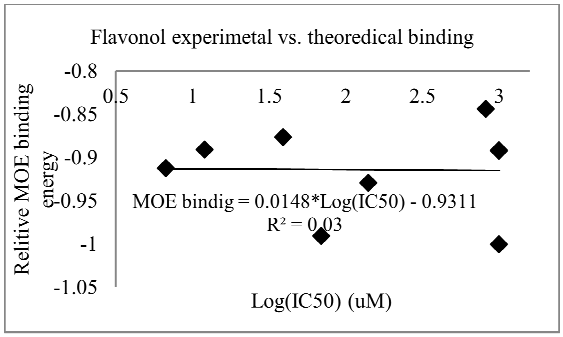

Figure 5: MOE generated relative binding energy's vs. Log(IC_{50}) values obtained experimentally. The low R^2 value (.03) suggest there is no correlation between the two values

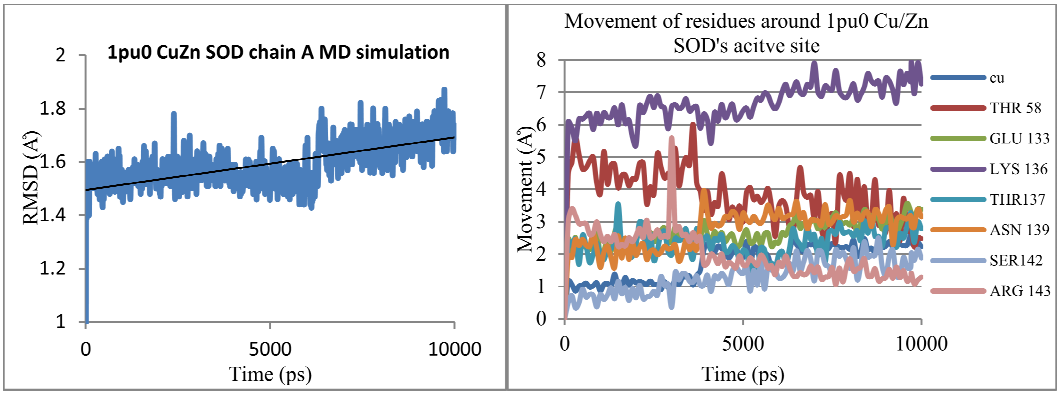

Figure 6: A) The RMSD movement of chain A of the 1PU0 CuZn enzyme over a 10ns MD simulation. B) Movement of the terminal atom of the residues around 1pu0 SOD's active site recorded every 100 ps during a dynamics 10 ns simulation.

time (Figure 6A). The RMSD values generated with MOE for the 1PU0 CuZn SOD were nearly identical to the ones Khare and Dokholyan report[21] for wild type SOD using a different software package.

To understand how these motions affect the active site geometry, the movements of the residues that "guard" the active site (Figure 7A) were examined. Figure 7B shows the pose of the residues that had the maximum deviation (blue residues) compared to their initial positions (red residues). Figure 6B show the distanced moved of the terminal atoms of these residues over the course of the simulation. The Lys 143 residue demonstrated the largest displacement with around an 8 Å maximum deviation from its initial position, and rotating 90 degrees out of the active site; while the majority of the residues moved between 1 and 4 Å.

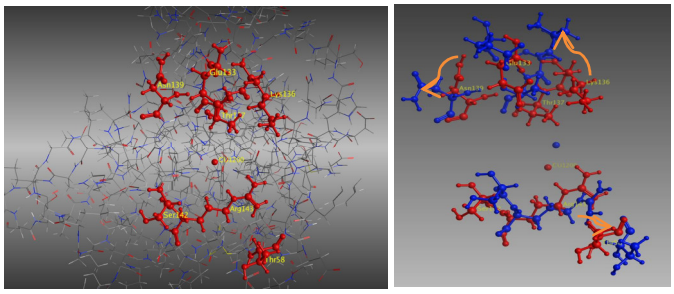

Figure 7: A) Residues in red "guard" the active site, and were examined for movement in the MD simulation. B) Residues in red are initial positions. Blue residues are the residues at the maximum deviation during the MS simulation. Orange arrows show direction of movement.

The geometry of the active site opened up during the course of the simulation as shown in Figure 7B. Using poses of the SOD with the active site least hindered, the docking simulation was performed again. The results of the docking experiment were similar to the first in that they showed effectively no poses of flavonols that "fit" into the active site and bound to the copper (results not shown).

Since the MOE program would not generate docking poses that were consistent with metal binding, the flavonols were chelated to the copper atom and the energies of the resulting system were minimized with MOE's energy minimization function. After minimizing the energy of the system, the binding energies were calculated. From these binding poses, we were able to determine that our proposed binding method (Figure 2) is sterically possible and shows favorable binding energies. Since the MOEs algorithm does not take into account the added stability a chelate provides, the chelate was artificially imposed. However even without the chelate imposed, favorable binding energies were observed in poses that were similar to chelated poses, but with only one of the flavonol's hydroxyl groups bound to the copper atom.

Figure 8 shows typical results of myricetin placed in the active site, chelated to the copper. From the simulations we saw that the residues Arg 143, Gly 141, Lys 136, and Glu 133 are available to participate in hydrogen bonding with the flavonol's 3 hydroxyl groups depending on the pose, with Lys 136

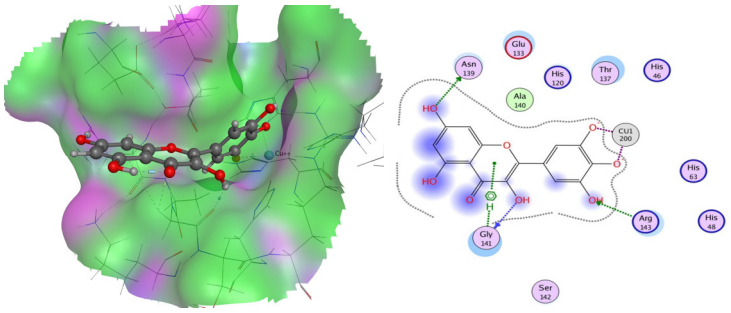

A. B.

Figure 8: A) MOE 3D model of myricetin chelated to the copper in SOD's active site. B) Interactions map of myricetin bound in panel A.

interacting most often. Also the extra hydroxyl group on myricetin's B ring tended to interact with the Arg143 residue; which is close enough to the copper atom to allow simultaneous chelation to the copper atom and hydrogen bonding to the Arg 143 residue.

To further investigate the proposed structure activity relationship (SAR), we used the MOE program to search a database of 650,000 lead like compounds for compounds that had the same essential components (chelating moiety and a flavonol 3 position equivalence) in a similar position (within 0.6 Å) as the active flavonols. From this database, 184 compounds were found to be similar to the active flavonols, of which five were selected and purchased. All five of the selected compounds were found to have apparent inhibition in the $^{19}F^-$ assay, having IC_{50}'s in the 100 to 600 μM range. This indicates that other compounds with similar structural features should also inhibit the SOD enzyme. Also, we tested compounds that lacked the hydroquinone group for SOD inhibition. These were not active inhibitors.

Flavonol aggregation. It has been reported that the aggregation state of flavonols affects their activity.[13,14] From our inhibition data, we also note that the SOD inhibition activity of the flavonols are dependent on aggregation state. Inhibition activities appear to decrease as aggregation of the flavonols increase.

For most flavonols, the plots of $\frac{1}{[SOD_{active}]} - 1$ versus inhibitor concentration were not linear, but showed curvature at the higher concentrations (Figure 9). This indicates that at higher concentrations the flavonols are less effective inhibitors than at lower

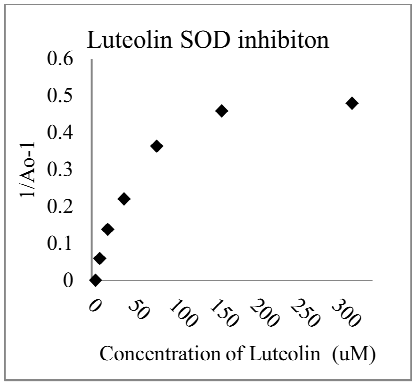

Figure 9: Curvature in the concentration vs. 1/Ao-1 plot for luteolin. This curvature is believed to be due to aggregation.

concentrations. We attribute this behavior to aggregation since it is thought that the monomers are the active inhibitor. At higher concentrations aggregation of these monomers is occurring and this aggregation would therefore remove the active inhibitors from solution, giving a lower activity than expected.

By plotting the square root of the inhibitor concentration versus $\frac{1}{[SOD_{active}]} - 1$ we are able to see a linear relationship for most of the flavonols (Figure 10 shows a representative example). From these square root plots, IC_{50} values for each of the flavonols were extrapolated. However, to find K_d values we had to quantify amount of aggregation that was occurring.

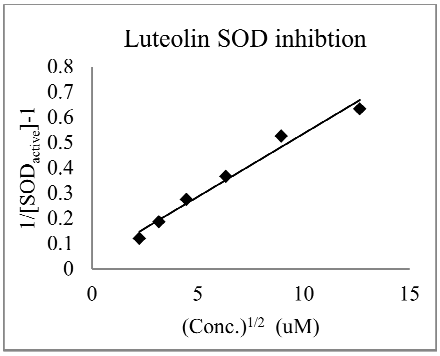

Figure 10: By taking the square root of concentration a linear relationship can be seen when plotted against $1/[SOD_{active}]-1$.

While the extent of aggregation over the entire range of our data is not certain, the square root dependence in Figure 10 argues that dimers (Equation 12) are the major form of aggregates over the concentration ranges of the inhibition studies. When this is the case the dimerization constant (Equation 13) can be used to find the active inhibitor species. Using equations 12, 13, and 14, equation 15 can be determined from NMR data if K_{dim} is known.

$$2monomer \rightleftharpoons dimer \tag{12}$$

$$K_{dim} = \frac{dimer}{monomer^2} \tag{13}$$

$$F = monomer + 2dimer \tag{14}$$

$$\frac{-1 \pm \sqrt{1 + 8K_{dim}[F]}}{4(K_{dim})(K_d)} = \frac{1}{A_{active}} - 1 \tag{15}$$

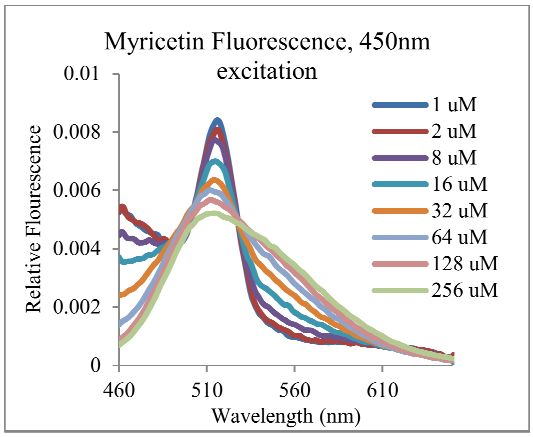

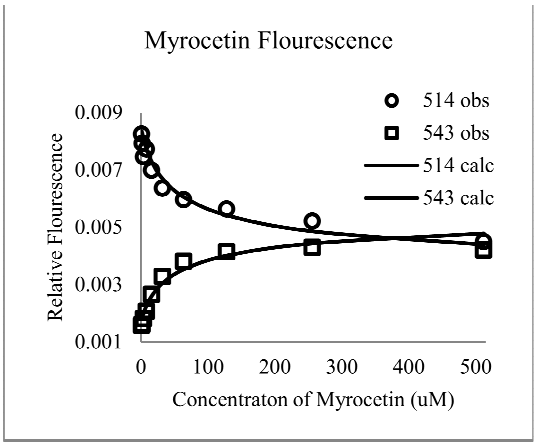

Figure 11: A) Fluorescence spectra of myricetin over the concentration range of 1 to 256 µM. B) Least squares analysis using 514 and 543 nm fluorescence data to calculate K_{dim}.

Flavonol aggregation was studied using fluorescence spectroscopy. The fluorescence spectra of most of the flavonols showed concentration dependence in the same range as the observed curvature in the plots of $\frac{1}{[SOD_{active}]} - 1$ versus inhibitor concentration (Figure 11A). The fluorescence spectra were normalized to the area under the curve to account for inner filter effects. Using multiple wavelengths the fluorescence data for each of the flavonols were fit, using the method of least squires, to the best fit values of the dimerization constant (Figure 11B), (some of the flavonols showed no variance in the fluorescence spectrum so the K_{dim} was not found). This dimerization constant and NMR data was then used with equation 15 to find the K_d's of the flavonols.

A principal component analysis was performed to determine the validity of our assumption that dimerization is the extent of aggregation on the fluorescence spectra of each flavonol. This analysis was done by using the factorization technique of singular value decomposition (SVD). The SVD method factors an *n* by *m* spectral matrix **A** (where *n* is the

number of spectra and *m* is the area normalized fluorescence intensity at a given wavelength), into an orthogonal basis set of its column and row vectors **S** and $\mathbf{U}^{\mathbf{T}}$ respectively, and where **V** is a diagonal matrix of the singular values arranged by decreasing size (equation 16). The column vectors in $\mathbf{U}^{\mathbf{T}}$ represent the principal components of the spectral data in decreasing order of significance. For a two component system, only the first two columns of $\mathbf{U}^{\mathbf{T}}$ would represent principal components, the rest of the columns in $\mathbf{U}^{\mathbf{T}}$ would represent noise in the data.

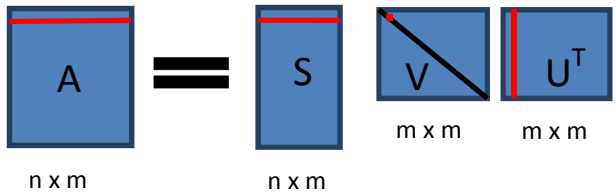

(16)

Equation 16: SVD decomposition of the spectral matrix **A**. Red lines/box represents the intuitive orientation of the data in the respective matrices.

By decomposing **A** into the $\mathbf{SVU}^{\mathbf{T}}$ factorization, and then recalculating **A** using only the desired number of principal components (for an *n* component system using only the first *n* rows of $\mathbf{U}^{\mathbf{T}}$ and *n* columns of the product of **SV**) the number of principal components can be analyzed by the percent of **A** represented by $\mathbf{A}_{calc}$. This was done using equation 17 (where $\sum\mathbf{A}$ and $\sum\mathbf{A}_{calc}$ is the sum of all the components of the respective matrix).

$$\%\ \mathbf{A}\ represented = \left(1 - \frac{|\sum A_{calc} - \sum A|}{|\sum A|}\right) * 100 \tag{17}$$

While the number of pure components (species in solution) may in theory be different than the number of principal components (those with independent spectra). The evidence suggests that two principal components account for the vast majority of the compounds over the concentration range studied.*

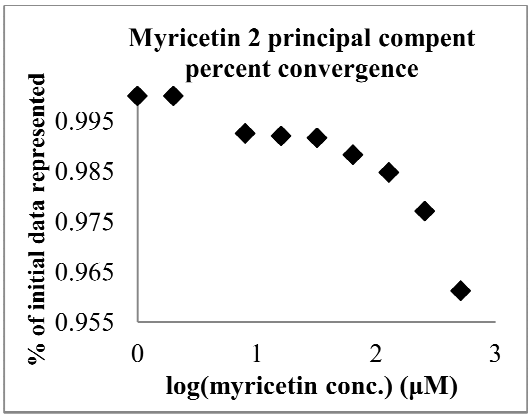

Figure 12: Percentage convergence of Myrocetin's fluorescence data using only two principal components.

In the concentration range where the monomer and dimer are the only species, each fluorescence spectrum contains only two pure components. Therefore calculating $\mathbf{A}_{calc}$ using only two principal components should regenerate **A** with nearly 100 percent of the data represented.

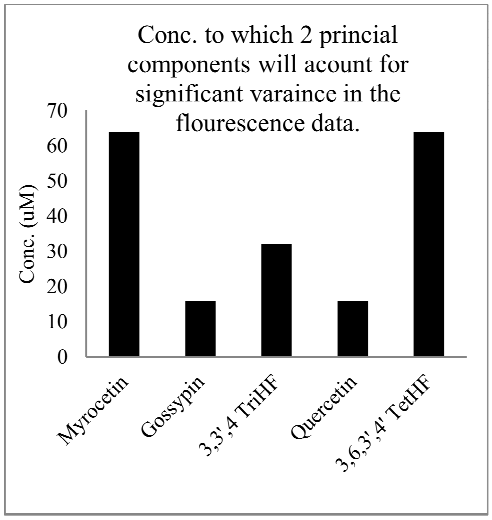

Figure13: Concentrations to which the principal component analysis using 2 components accounted for all the significant variance in the fluorescence data for each of the flavonols.

The percentage of the flavonol fluorescence data (**A**) represented by $\mathbf{A}_{calc}$ using only two principal components was calculated starting with the spectrum that represented the lowest concentration, then recalculating with each additional spectrum that represented the next highest concentration. Figure 12 shows this

* This could occur when a pure species has no spectral response, or because a pure species is not linearly independent over the range of the spectra (i.e. shows a constant spectral response). We assumed that the linearly independent species at the lower end of the concentration range is the monomer, and the next spectral species with increasing concentration is the dimer. Since the dimerization model gives a good fit to our NMR assay results in this concentration range, this assumption is thought to be valid.

analysis preformed on the myricetin data. This data could be represented by two principal components with 99 percent accuracy up a concentration 64 μM myricetin. Above this concentration the percent convergence started to drop off quickly indicating the addition of another species.

This principal component analysis shows that 2 principal components could only account for the variance in the fluorescence data in the lower concentrations for the flavonols. Figure 13 shows the concentration to which the variance in the fluorescence data could be accounted for by two species. Above these concentrations the percent convergence began to drop sharply as shown in higher concentrations in Figure 12 (due to different amounts of noise in the data the percentage at which this occurred varied).

Inhibition by low molecular weight phenolic compounds. The structure activity relationship developed from the flavonol experiment led us to study interactions of the enzyme with smaller molecules having the essential components for binding. These components included a catechol or gallol group able to bind to the copper and a hydrogen bond donor/acceptor in a similar position as the 3 hydroxyl group in the flavonols.

We looked at several compounds that fit these criteria. Some of the more effective inhibitors are shown in Figure 14. While many of the compounds

Compound	IC_{50}	Compound	IC_{50}
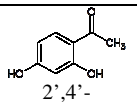 2',4'-Dihydroxyacetophenone	≈2.5 mM	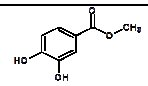 Methyl 3,4-Dihydroxybenzoate (MDHB)	≈1 mM
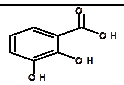 2,3-Dihydroxybenzoic acid	≈5.5 mM	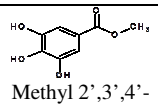 Methyl 2',3',4'-Trihydroxybenzoate (MTHB)	≈0.5 mM
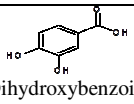 3,4-Dihydroxybenzoic acid	≈1.5 mM	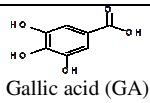 Gallic acid (GA)	<0.1 mM

Figure 14: Small phenolic compounds that we have investigate, and show activity against SOD.

showed some apparent SOD inhibition, the most effective inhibitors had the gallol moiety. This was also observed in the flavonols that were studied, where myricetin was most active. We note that the compounds without the ability to chelate showed higher IC_{50} values then the compounds that could chelate (IC_{50} was used rather than K_d because the aggregation observed in these compound has not been investigated). (As for 2,3-dihydroxybenzoic acid, which appears to be able to chelate, its IC_{50} is thought to be much higher than other chelators because of steric interactions with the active site hindering its ability to chelate to the copper.) This is also supported with MOE modeling which generated poses with either the carboxylic acid or 3 hydroxyl (depending on how the chelation is imposed) clashing with the walls of the active site when chelated to the copper.

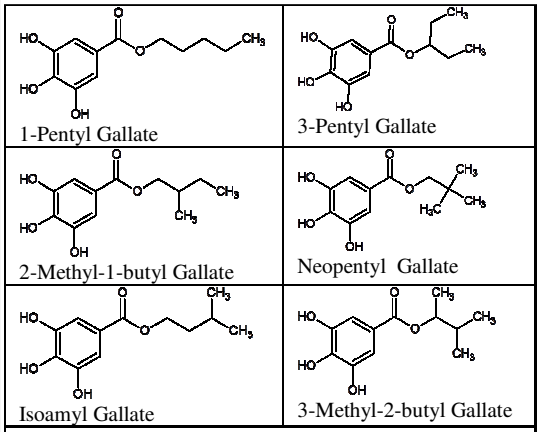

Figure 15: Synthesized isomers of pentyl gallate. The bulkier the alkyl chained esters shows lower binding affinity then the straighter alkyl chained esters.

To address the question of whether or not our compounds were binding to the SOD enzyme in the manner predicted (by chelating to the copper in the active site) or inhibiting through another mechanism; we synthesized six isomers of pental gallate (Figure 15). We reasoned that if the compounds inhibited by binding to the copper in the active site, then the esters with bulkier alkyl chains (i.e. neopental gallate and 3-pental gallate) should show a lower binding affinity for the enzyme than esters that have straighter alkyl chains. This is because the bulkier esters would encounter steric hindrance while trying to fit into the pocket of the active site.

To test our hypothesis, the binding affinity of the gallate esters were first calculated using the MOE program. This was done by placing the compounds in SOD's active site in such a way that they chelate to the copper by their 3 and 4 hydroxyl groups; then the energy of the system was minimized with the MOE energy minimization application. The MOE program was used to calculate the binding energies of the lowest energy state for the bound ligand. The computational results supported our hypothesis that the bulkier esters were sterically hindered from fitting into the pocket of the active site; leaving the hydrophobic alkyl chain in the aqueous surroundings, and lowering their binding affinity. The more flexible, straighter chained esters were able to conform to the contours of the active site, allow the alkyl chains to fit into the hydrophobic pocket of the enzyme (Figure 16).

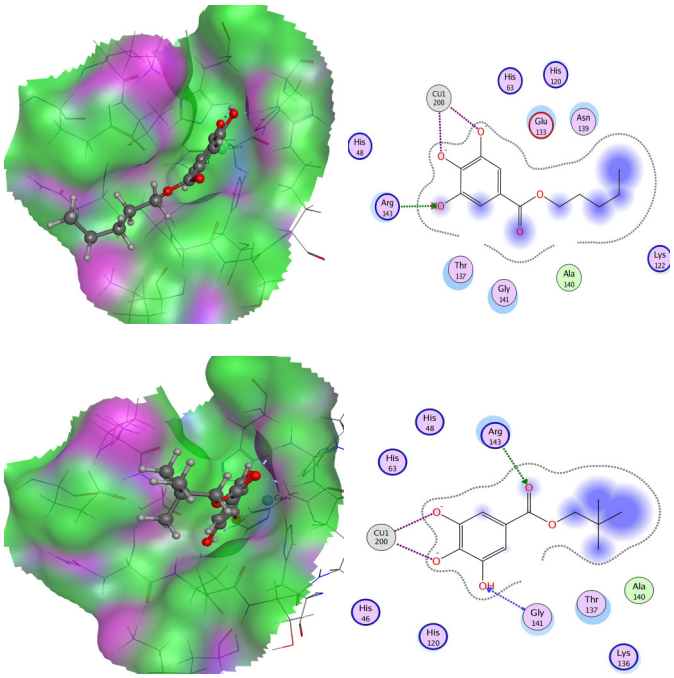

Figure 16: MOE modeling of 1-pental gallate (top panel), and Neopetyl gallate (bottom panel). The modeling show the bulkier alkyl chain is less able to fit into the active site then the straight chained 1-pently gallate.

The esters were prepared and tested for inhibition against the enzyme using the $^{19}F^{-}$ NMR assay previously described. While the concentration dependence of inhibition was consistent with aggregation of the inhibitors, assuming the aggregation constants are similar, the relative binding affinities from the experimental data correlate with the calculated binding results from the MOE program (Figure 17). This correlation between the experimental and calculated results suggest

that the MOE poses that were used in the calculated results are representative of the actual inhibition method, supporting the hypothesis that the compounds must fit into the pocket of the active site to inhibit the NMR activity.

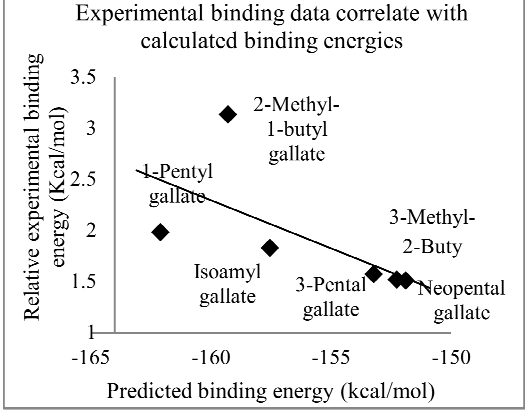

Figure 17: Predicted (MOE calculation) versus experimental (^{19}F assay) binding data for the synthesized esters. The correlation suggests the proposed binding method is accurate.

The pH dependence of inhibition. It has been reported that SOD's catalytic activity is constant in the pH range from 5 to 10.[16] However, our inhibition data shows a pH dependence within this 5 to 10 pH range. We attributed this variation to the protonation state of the inhibitors. When the pH increases above 10, it is thought that one of the residues in SOD's active site is deprotonated making the enzyme more vulnerable to inhibition.[16]

To see how the protonation state of an inhibitor affects inhibition Sherri Barborich, a member of our group, looked at inhibition over the 5 to 10 pH range where SOD activity is constant. The compound used for this experiment was 3',4',5'- methyl trhihydroxybenzoate (MTHB, Figure 14) .[16] MTHB has its first pK_a at 7.88 for its 4' hydroxyl group which is at one of its metal chelating positions.[17] Figure 18 shows the

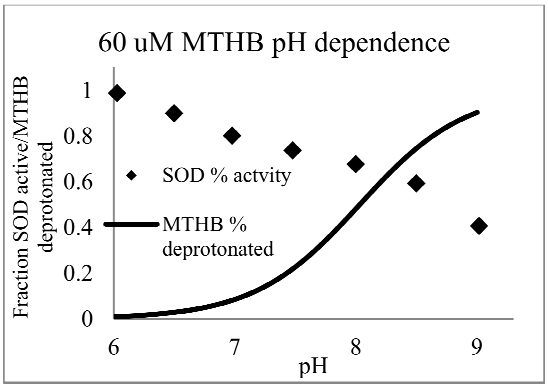

Figure 18: pH dependence on enzyme inhibition (diamonds) correlating to deprotonation of MTHB's 4' hydroxyl group (line).

enzyme activity with 60 μM MTHB, as well as the percentage of deprotonated MTHB, in the pH range of 6 to 9. Our results demonstrate that as the percentage of deprotonated MTHB increases, the percent of active enzyme decreases. Furthermore, when MTHB is fully protonated there is nearly no inhibition.

Figure 19 shows an identical experiment run with Gallic acid (GA Figure 14). GA has its first pK_a at 3.13 for its carboxylic acid, and its second pK_a at 8.84 for its 4 position hydroxyl group.[17] In the pH range of the experiment, GA's carboxylic acid is fully deprotonated. However from the inhibition data (Figure 19) it is apparent that it is not until deprotonation of the 4 position hydroxyl group, which is in a copper chelating position, that inhibition occurs. These results indicate that deprotonation at one of the catechol hydroxyl groups is essential to inhibition and that deprotonation at non-metal binding sites has little effect on inhibition. However, deprotonation in non-metal binding sites would affect the solubility and aggregation state of inhibitors.

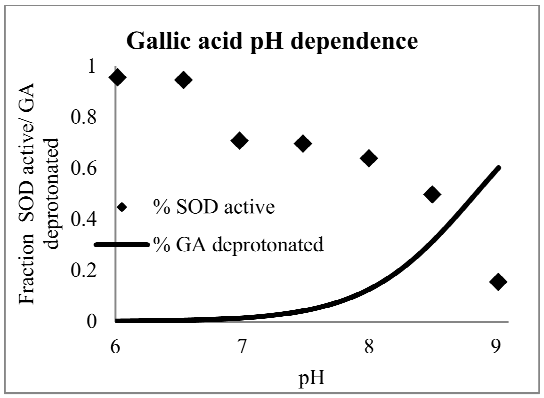

Figure 19: The pH dependence of inhibition for GA is due to the deprotonation of the 4 position hydroxyl (pK_a 8.84) and not the carboxylic acid (pK_a 3.13); showing the importance of deprotonation in a metal binding site.

SOD inhibition mechanism. We investigated four possible mechanisms by which low molecular weight compounds could inhibit the ^{19}F NMR activity of SOD. They could act by an aggregate mediated mechanism, by blocking the active site, metal sequestering or by reducing the

paramagnetic copper atom. Results of this study indicate reduction of diamagnetic copper to be the cause of the loss of ^{19}F NMR activity.

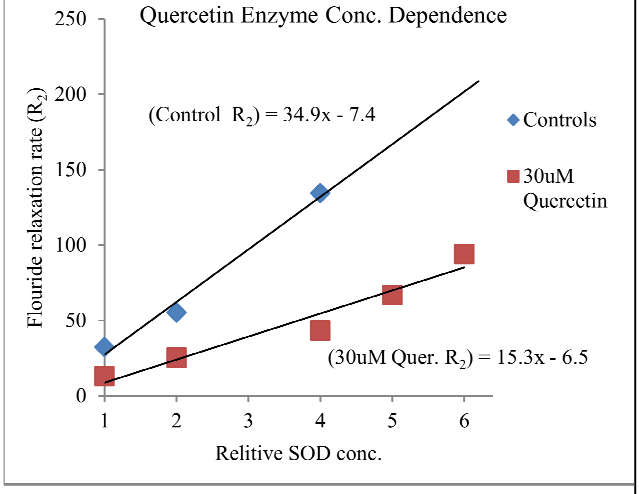

Figure 20: Six fold SOD concentration dependence on Quercetin inhibition. The inhibition remained constant at around 60%, suggesting inhibition is not occurring by aggregation.

Studies of aggregate based mechanism. It has been reported that quercetin forms aggregates that are large enough for the enzyme β-lactamase to bind too through van der Walls forces.[15] Inhibition can occur as enzymes bind to these aggregates and then become partially denatured.[13]

To test whether flavonols inhibit by this mechanism we examined the inhibition of 30 μM quercetin over a six-fold concentration range of SOD. If inhibition involves inhibitor aggregates, then inhibition constants should be dependent on the concentration of SOD.[14] This dependence on SOD concentration is due to the aggregates becoming saturated with enzyme. Figure 20 shows the fluoride relaxation rate of controls with no quercetin (blue diamonds) and samples with 30 μM quercetin (red squares). From this data it can be seen that, within experimental error, the apparent enzyme activity in the sample with quercetin retains around 40 percent activity compared to the control sample. This constant inhibition percentage regardless of SOD concentration indicates that inhibition of SOD by quercetin does not occur by an aggregation based method in this concentration range. Since both the K_d's and K_{dim} are on the same order of

magnitude for all the active flavonols, this result for quercetin is likely to hold for the other active compounds as well.

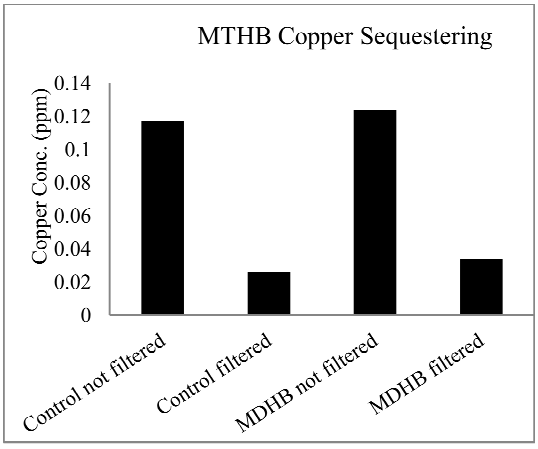

Figure 21: Copper concentrations of SOD solution without (control) and with MDHB before and after filtering with an YM-10 filter. The similar concentrations between the control and MDHB solutions suggest metal sequestering is not occurring.

It has been reported that catechols form stable metal complexes.[27] Also the compound quercetin is known to bind copper via its catechol group.[28] From this we hypothesized that inhibition of SOD may occur by metal binding and subsequent sequestering of the copper from SOD's active site. To address this we looked at whether or not sequestering was occurring for the compound MDHB at pH 8. If sequestering by MDHB was occurring, it would also suggest that compounds that have a higher affinity to copper could inhibit by sequestering the copper from SOD.

To investigate whether or not sequestering was occurring we used inductively coupled plasma optical emission spectroscopy (ICP-OES) to determine copper concentrations of SOD solutions with and without MDHB. In these experiments solutions were allowed to equilibrate overnight to ensure adequate time for reaction to occur. Solutions were prepared either with or without MDHB and fractionated with a Millipore YM-10 centrifugal concentration device. This excludes species larger than 10,000 Daltons. Since the SOD has a molecular weight of 32,500 Daltons, the YM-10 filter should retain the SOD, but allow low molecular weight copper complexes to pass through. Once separated, the copper concentrations were determined by ICP-OES.

Figure 21 shows the ICP-OES results from this experiment. Within experimental error, addition of MTHB did not lead to an increase in copper in the low molecular weight fraction of the control (73 and 78 percent respectively of the copper removed by the filter). This indicates that inhibition by MDHB does not result from sequestration of the copper from SOD.

Thiol vs. Hydroxyl inhibition. Since sulfur has a greater affinity for copper then oxygen, substituting sulfurs for hydroxyl groups in metal binding sites of inhibitors should increase inhibition; if inhibition involves binding to the copper in SOD's active site. [18]

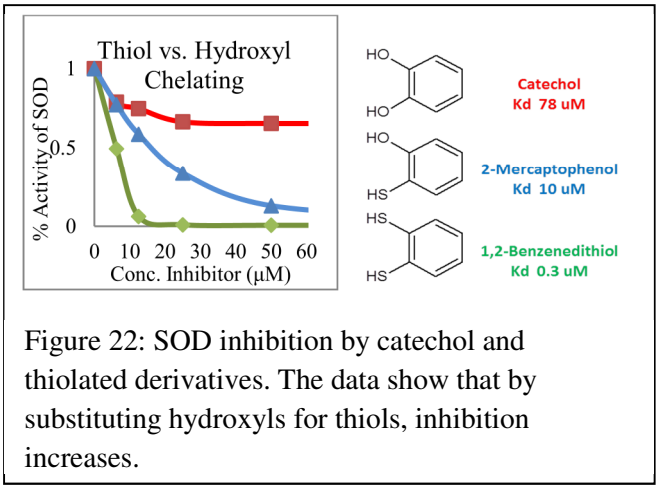

Figure 22: SOD inhibition by catechol and thiolated derivatives. The data show that by substituting hydroxyls for thiols, inhibition increases.

To test this hypothesis we looked at catechol, and two thiolated derivatives: 2-mercaptophenol, and 1,2-benzenedithiol (Figure 22). Figure 22 shows the SOD activity as a function of each of the inhibitor concentrations. The data in Figure 22 shows that as the hydroxyl groups are replaced by sulfurs apparent inhibition increases. We note that sulfur's greater reduction potential could also cause the increase in apparent inhibition.

SOD redox reaction with inhibitors. To investigate whether inhibitors bind to copper in SOD's active site, we collaborated with the research group of Julia L. Brumaghim from Clemson University to determine whether inhibitors affect the EPR signal of the copper in SOD. Figure 23 shows EPR data for MTHB (Figure 23 A and B) and MDHB (Figure 23 C and D) with copper (II) at pH 8 and 11. Before adding inhibitors, the EPR signal consists of a series of peaks for the oxidized, paramagnetic form of the copper. Upon addition of MTHB the spectrum changes to a series of lines at different frequencies and slowly decays with time, virtually disappearing after 24 hours in the MTHB samples. The change in signal indicates change in the coordination environment of the copper, presumably binding MTHB. The decay of the signal indicates that the copper has been reduced to the diamagnetic +1 oxidation state. In contrast, signal is not lost in the

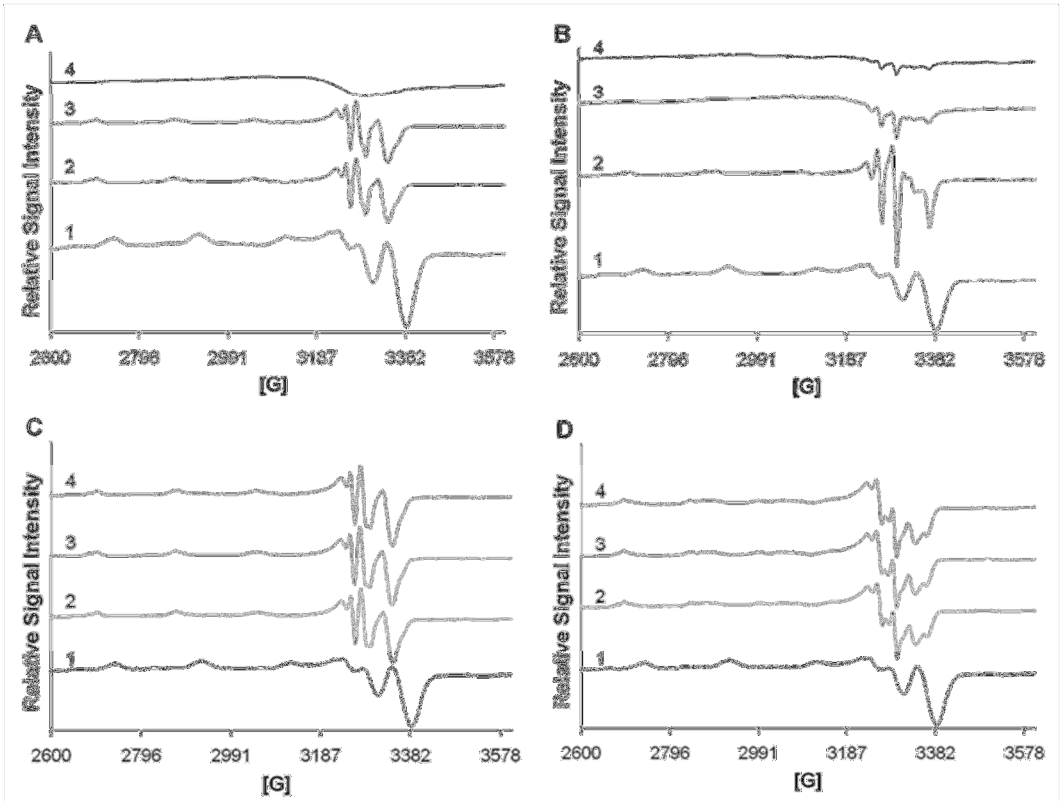

Figure 23: EPR spectra of $CuCl_2$ without polyphenol (1); with polyphenol after 1 min (2); with polyphenol after 1 h (3); and with polyphenol after 24 h (4) for A) MTHB at pH 8; B) MTHB at pH 11; C) MDHB at pH 8; and D) MDHB at pH 11.

MDHB treated samples. Figure 24 shows a similar experiment where SOD was used instead of copper (II). The data in Figure 24 also shows a reduction in the intensity for the copper (II) peak upon incubation with MTHB at both pH 8 and 11and MDHB at pH 11. At pH 8, treatment with MDHB shown a new set of frequencies similar to those observed with MDHB and free copper (II) at pH 8 indicating coordination to the copper. While this could indicate lose of copper (II) from SOD, filtration experiments data indicates that this is not occurring. We conclude that compounds bind copper in SOD's active site and undergo an election transfer to reduce the copper (II) in SOD.

The reduction of the copper in the presence of these inhibitors raises the question: does the redox activity of the inhibitors determine their effectiveness as SOD inhibitors in the ^{19}F

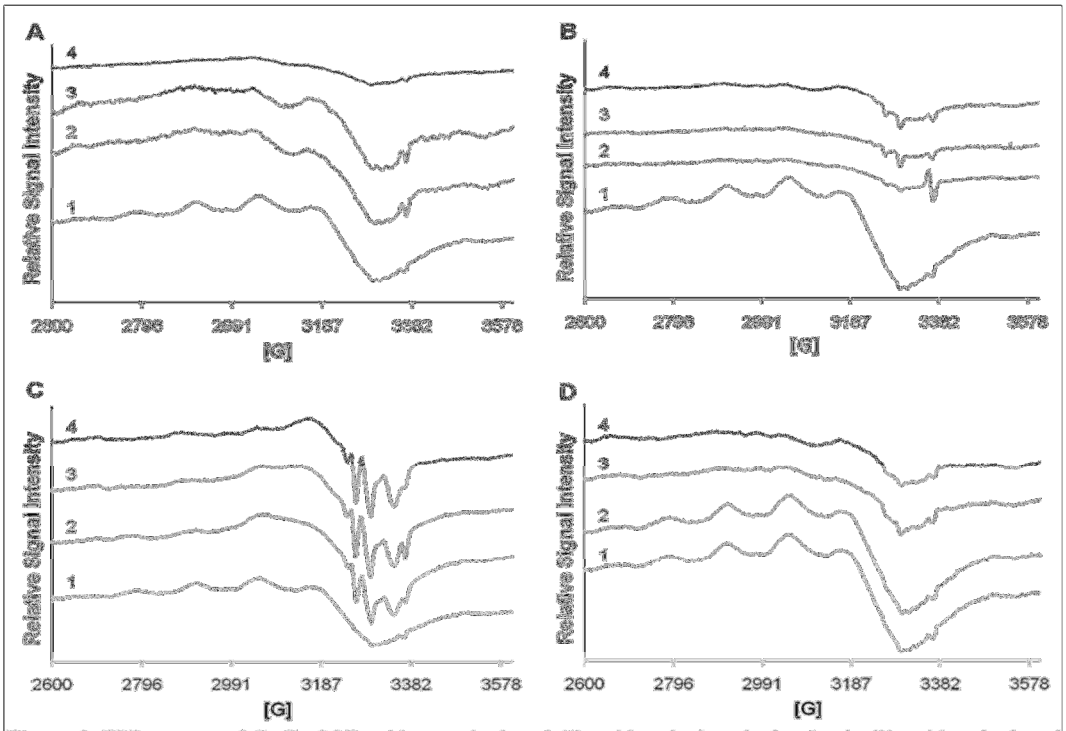

Figure 3. EPR spectra of Cu,Zn-SOD without polyphenol (1); with polyphenol after 1 min (2); with polyphenol after 1 h (3); and with polyphenol after 24 h (4) for A) MTHB at pH 8; B) MTHB at pH 11; C) MDHB at pH 8; and D) MDHB at pH 11.

Figure 24: EPR spectra of Cu,Zn-SOD without polyphenol (1); with polyphenol after 1 min (2); with polyphenol after 1 h (3); and with polyphenol after 24 h (4) for A) MTHB at pH 8; B) MTHB at pH 11; C) MDHB at pH 8; and D) MDHB at pH 11.

NMR assay?

If the flavonols are coordinating with, and reducing the copper (Equation 18) as suggested by the MTHB and MDHB EPR data, inhibition constants should be related to the oxidation potentials of the flavonols by Equation 20. Pietta[19] noted that the antioxidant activities of flavonols have a SAR that is nearly identical to the SAR we developed for SOD inhibition by flavonols.

$$Inhibitor_{RED} + SOD_{OX} \rightleftharpoons Inhibitor_{OX} + SOD_{RED} \quad (18)$$

$$E^0_{rx} = \frac{RT}{nF} lnK \quad (19)$$

$$E^0_{Inhib\ Ox} = \frac{-RT}{nF} lnK + E^0_{SOD\ RED} \quad (20)$$

$$E^0_{Inhib\ Ox} = \frac{RT}{nF} \ln(IC_{50}) + E^0_{SOD\ RED} \quad (21)$$

Figure 25 shows our experimental IC_{50} values plotted against published half peak oxidation potentials[20] (IC_{50}'s were used rather than K_d because dimerization constants were not found for all the flavonols of interest. Since IC_{50} is proportional to 1/K, Equation 20 can be modified to give equation 21). Figure 25 shows a linear relationship between our experimental IC_{50} data and half peak oxidation potentials, with a slope of 35.3 mV. This value of 35.3 mV found by the slope of the graph in Figure 25 is close to the value of $\frac{RT}{nF}$ (25.69 mV assuming n=1). This shows that the apparent inhibition correlates with the reduction potential of the flavonols.

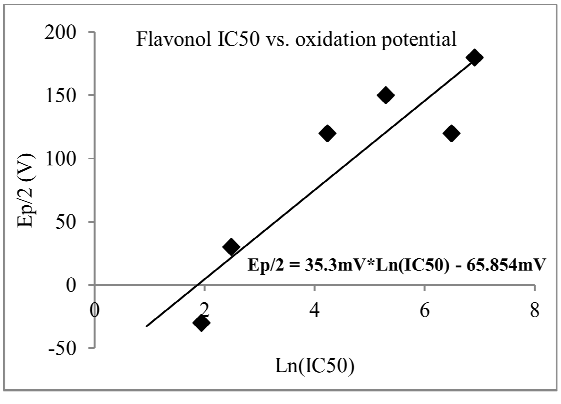

Figure 25: Flavonol NMR inhibition correlates with oxidation potentials.

Since the EPR data shows copper being reduced from the oxidized

paramagnetic copper (II) to the diamagnetic copper (I) form, and since the reduction potential of the flavonols correlates with apparent inhibition, we hypothesized that inhibitors might only reduce the copper and not block SOD's active site. This reaction would account for the observed inhibition in the $^{19}F^-$ NMR assay, since the diamagnetic form of the copper does not affect the fluoride's relaxation rate. We note that inhibition of NMR assay by this mechanism would not cause loss of SOD's enzymatic activity since the copper (I) form is an intermediate in the catalytic cycle.

To test whether the compounds affect SOD's redox cycling, we conducted an experiment where partially inhibited enzyme was treated with compounds known to generate superoxide (NADH and PMS). In the absence of inhibitor, superoxide reacts with the SOD as described by Equations 3 and 4. In the reaction with $O_2^{\cdot}$, SOD cycles between oxidized and reduced forms and reaches a steady state where the ratio of paramagnetic to diamagnetic copper is constant. This ratio can be monitored with the $^{19}F^-$ CPMG experiment. If an inhibitor, such as quercetin, binds to and blocks the active site of the SOD, then inhibited SOD will be effectively removed from solution and the addition of NADH/PMS will cause the remaining uninhibited SOD to react with the $O_2^{\cdot}$ and reach a steady state having the same percentage paramagnetic and diamagnetic copper as the solution without quercetin. In contrast, if quercetin does not inhibit SOD activity, then the addition of NADH/PMS will cause the solution to reach the same steady state as solutions without quercetin.

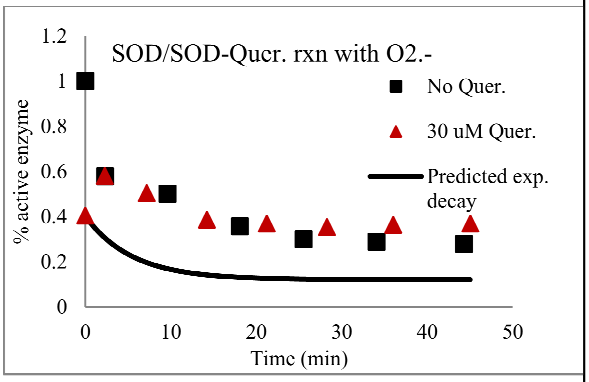

Figure 26: Effect of $O_2^{\cdot -}$ on the oxidation state of SOD, and SOD with 30 μM Quercetin over time.

Figure 26 shows the experimental data from the SOD redox experiment. The black squares in this figure show the effect of $O_2^{\cdot}$ on ^{19}F relaxation by SOD. As shown, in the absence of inhibitor, a steady state is reached with around 30 percent of the SOD in the paramagnetic form in the absence of quercetin. The red triangles show the results of the same experiment performed in the presence of quercetin. The red triangle at time zero shows that prior to addition of PMS/NADH the SOD relaxation in the quercetin sample was approximately 40 percent that of the control. The black line shows the predicted behavior for the case where quercetin bound to and blocked the active site and the remaining uninhibited SOD reached a steady state with 30 percent paramagnetic copper. The red triangles show the actual behavior of a 30 μM quercetin solution upon addition of NADH/PMS. As shown in Figure 24, the quercetin containing sample reached the same steady state as the sample without quercetin (within experimental error) when treated with $O_2^{\cdot}$. This result is consistent with the hypothesis that quercetin reduces the copper to the diamagnetic form and that the diamagnetic form retains its enzymatic activity.

Studies on Superoxide Dismutase Inhibition Conclusion

Using the $^{19}F^{-}$ assay, we have found that a number of flavonols and small phenolic and thiol compounds inhibit SOD's NMR relaxation activity. The apparent inhibitory activities of these compounds show a dependence on their structure, aggregation state, and pH. However this apparent NMR inhibition did not correlate with inhibition of the enzyme's activity. We believe that NMR activity results from reduction of the copper in the active site.

The activity of the flavonols was found to depend on the presence of the 3, 3' and 4' hydroxyl groups which were present in all the active compounds. From these structure activity relationships we hypothesized that the flavonols bind to the enzyme by chelating to the copper atom in the active site with the 3' and 4' hydroxyls and that the 3 position hydroxyl group participated in hydrogen bonding to one of the residues in the active site. Using computational software, it was determined that our proposed mechanism was viable, and produced favorable binding energies. However, our hypothesis for the binding method has been shown to be incorrect; or at least insignificant because the inhibitors do not bind to the active site, but rather reduce the copper without permanent binding.

From the $^{19}F^-$ assay we noted that as the concentration of some of the inhibitors increased, their effectiveness as inhibitors decreased. This behavior was attributed to aggregation. The fluorescence spectra of these compounds, which showed concentration dependence in same range as in the $^{19}F^-$ assay. From the dependence of the fluorescence spectra on concentration, we characterized the aggregation of most of the flavonols we studied. Principal component analysis indicated that dimerization alone cannot account for the aggregation observed in the higher concentrations of our assay. At the lower concentrations, however, the monomer/dimer equilibrium represented our data well.

The inhibitors activities were also pH dependant. We have shown that below pH 10, this pH dependence arises from the deprotonation of the inhibitors, and that the activity of the enzyme is more or less constant. [16] This behavior might be attributed to the increased solubility or affinity for a negatively charged inhibitor for the copper cation, or to the oxidation of the inhibitors becoming more thermodynamically favored once they are deprotonated.

While we initially thought that the NMR inhibition was due to binding of the inhibitors to the copper inside SOD's active site, the EPR and superoxide reactivity studies indicate that this

apparent anti-SOD activity arises from reduction of SOD's paramagnetic copper to diamagnetic copper. The observation that samples with and without an inhibitor reaches the same steady state after addition of superoxide generating species (NADH and PMS) shows that the compounds did not inhibit the enzymatic activity of the SOD.[26]

APPLICATION OF METHODS TO STUDY METAL ION PARTICIPATION IN COMPLICATION OF DIABETES

Studies of Species Implicated in Complications of Diabetes Background

Diabetics display increased chemical modification of proteins and lipids that occur through the Mallard reaction with sugars. For proteins, this leads to the formation of advanced glaciation end-products (AGEs).[22] Products of reactions with lipids are called advanced lipoxidation end-products (ALEs).[23] While most modifications of proteins involve amine groups, Alderson *et al.*[24] reports that the chemical modification of sulfhydryl groups also occurs.[24] This modification appears to occur by a Michael addition of sulfhydryl groups to the Krebs Cycle intermediate fumarate (Equation 22). The product of this reaction is a S-(2-Succinyl)cysteine (2SC) modified protein.[28] Since glutathione concentrations in vivo can reach up to 10 mM it seems likely that reduced glutathione would also react with fumarate to give S-(2-succinyl)-glutathione (2SGT, Figure 27B).[31] In diabetic patients concentrations of AGE/ALE correlate with concentrations of modified sulfhydryl groups. This protein modification might arise due to the up regulation of fumarate in diabetics due to impaired mitochondrial metabolism.[24]

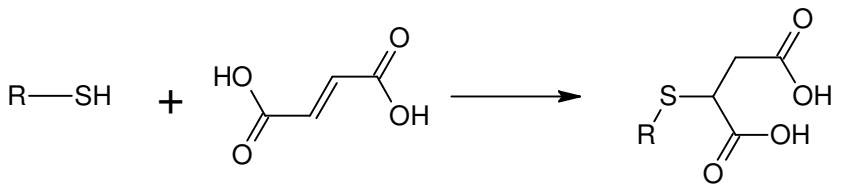

(22)

Protein Sulfhydryl Fumarate 2SC Modified Protein

Since succinic acid binds metals with a log(K) = 6.88 for iron (III) and log(K) = 2.6 for copper (II), and copper succinate is known to catalyze the disproportionation of superoxide, it has been proposed that 2SC modified proteins in vivo might influence oxidative stress by binding metal ions.[25, 34] In this study we investigated the possibility that the 2SC/2SGT species bind metals in a way that allows them to participate in metal catalyzed reactions.

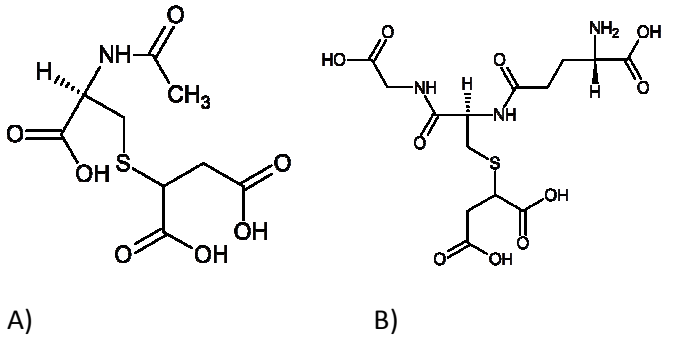

Figure 27: Synthesized compounds used to study possible 2SC reactions in vivo. A) S-(2-succinyl)-N-acetlycysteine B) give S-(2-succinyl)-glutathione.

We synthesized S-(2-succinyl)-N-acetlycysteine (2SAC, Figure 27) and 2SGT to study metal binding by cysteine residues and their subsequent redox chemistry.

We were specifically interested in redox activates of metals bound to 2SAC/2SGT. These reactions include of superoxide cycling (Equation 1 and 2) and the Haber-Weiss Cycle (Equations 3 and 4) which produces the hydroxyl radical. The ability of these metal complexes to catalyze the Haber-Weiss cycle is of particular interest since complications of diabetes have been linked to increased oxidative stress.

Reactions of 2SAC-Cu complexes with superoxide are likely to require access of solution to the metal center. We used ^{19}F NMR methods to determine whether the metal ion is accessible to solution. Earlier we have shown that the $^{19}F^-$ ion can predict rates at which metal complexes react with superoxide radicals. The ^{19}F NMR resonance is highly affected by the presence of paramagnetic metals (discussed above for SOD inhibition). If fluoride can contact the metal, then

other small molecules such as superoxide and H_2O_2 should be able to as well, and, if thermodynamically possible, undergo metal catalyzed redox reactions.

Electrochemical behaviors of the 2SAC/2SGT compounds were studied using cyclic voltammetry. As described by Boukhalfa *et al*.[29] a metal complex with a redox potential between -160 and +460 mV vs. NHE may catalyze the Haber-Weiss Cycle (Equations 1 and 2).

Reactions of 2SAC and 2SGT copper complexes with superoxide were studied with ^{19}F NMR. The production of the hydroxyl radicals from hydrogen peroxide was studied by monitoring the effects of 2SAC/2SGT-Cu on the visible spectrum of rhodamine B.

Application of Methods to Study Metal Ion Participation in Complication of Diabetes

Experimental

2SAC synthesis. Maleic acid (Sigma-Aldrich) and N-acetyl-L-cysteine (Alfa Aesar) were obtained and both used without further purification. Approximately 2 g of maleic acid and c.a. 2.8 g of N-acetyl-L-cysteine (4:3 ratio of maleic acid to N-acetyl-L-cysteine) were dissolved in c.a. 50 mL of H_2O and the solution was adjusted to a pH of 7.4 with 1 M NaOH. The solution was stirred under inert atmosphere and low heat (c.a. 35 ˚C) for 48 hr. The solution was then acetified to a pH of 0.9 with 2 M HCl and put into a separatory funnel. The solution was then washed 5 times with ethyl ether to remove excess maleic acid. The solution was transferred to a RBF and the solvent removed under reduced pressure to give a white solid. Acetone was added to

the crude product to dissolve the desired product while leaving NaCl as a precipitate. The solid NaCl was filtered off and the filtrate evaporated under reduced pressure leaving behind the desired 2SAC product. Products were characterized by ^{1}H and ^{13}C NMR and Mass Spec. The ^{1}H NMR assignments in figure 28 were established by COSY, HSQC, and HMBC NMR (Appendix B).

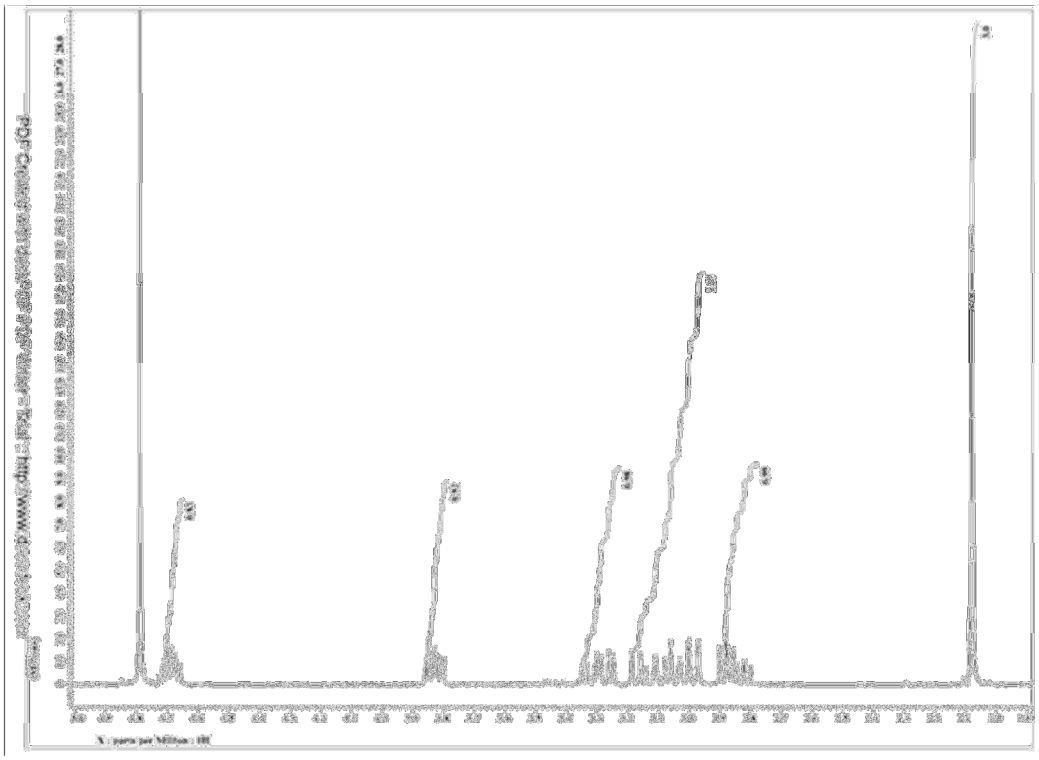

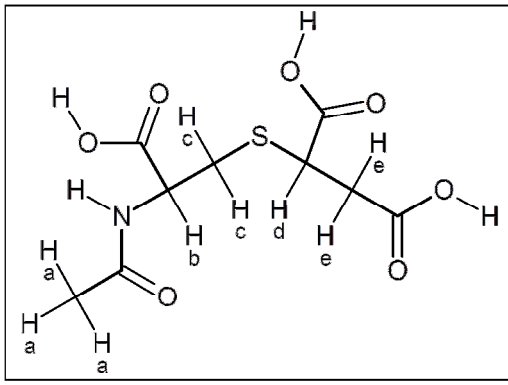

Peak	Shift (ppm)
a	2.08
b	4.69
c	3.11
c'	3.28
d	3.83
e	2.88
e'	3.00

Figure28: ^{1}H NMR spectrum assignments for 2SAC. For peaks *c* and *e* stereochemistry was not assigned.

2SGT synthesis. Maleic acid (Sigma-Aldrich) and reduced glutathione (Amresco) were obtained from commercial sources and used without further purification. Maleic acid (2 g) and c.a. 4 g of glutathione (4:3 ratio of maleic acid to glutathione) were dissolved in 50 mL of H_2O and the solution was adjusted to a pH of 0.9 with 2 M HCl. The solution was stirred under vacuum and low heat for 48 hr. The solution was then transferred to a separatory funnel and washed 5 times with ethyl ether to remove excess maleic acid. The solution was evaporated under reduced pressure to give a 2SGT as a white solid. The product was confirmed by ^{1}H and ^{13}C NMR and mass spectrometry. The ^{1}H NMR assignments are given in figure 29. The ^{1}H NMR assignments given in figure 29 were determined by COSY, HSQC, and HMBC NMR (Appendix B).

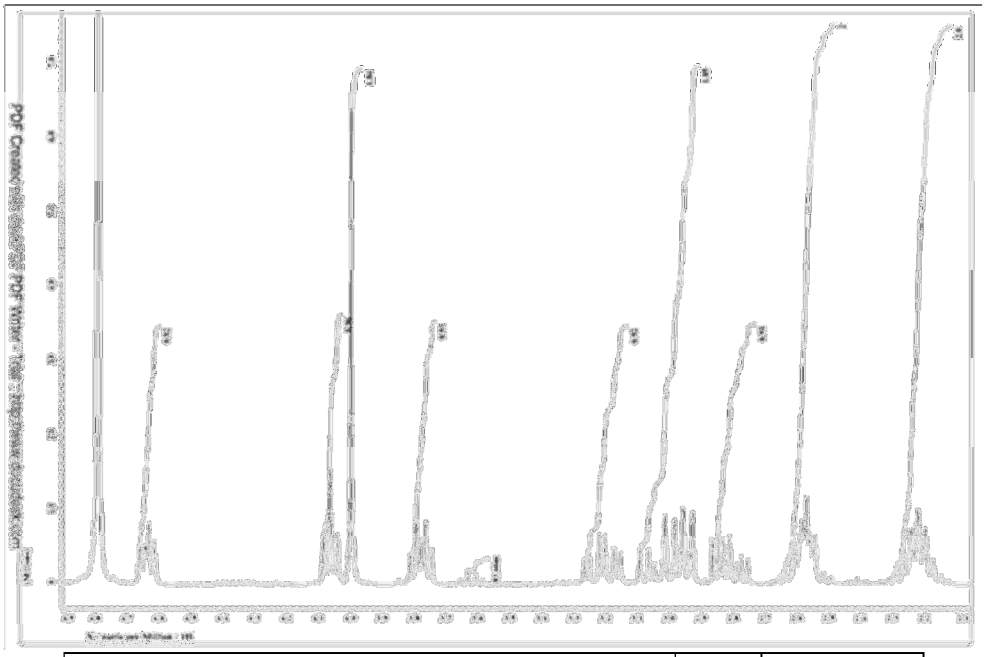

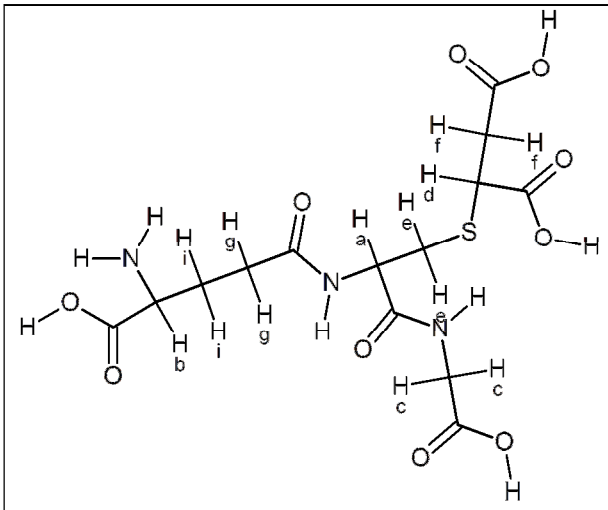

Peak	Shift (ppm)
a	4.63
b	4.07
c	4.00
d	3.78
e	3.22
e'	3.02
f	2.95
f'	2.81
g	2.57
h	2.22

Figure 29: ^{1}H NMR spectrum assignments for 2SGT. For peaks *e* and *f* stereochemistry was not assigned.

Determination of acid dissociation constants (pK_as) for 2SAC and 2SGT. Protonation constants of 2SAC and 2SGT were found by titration of a 10 mM solution of either 2SAC or 2SGT with a sodium hydroxide solution while moitoring the pH (Hanna Instruments HI2215). A detailed description of the experimental setup is given in Appendix C. The ionic strength was mantained at 0.1 M with either KNO_3 or KCl. The filled black diamonds in Panels A and C of Figure 30 shows representative titrations of 2SAC and 2SGT with sodium hydroxide. From the titraiton curve three protonation constants were found for 2SAC. These are attributed to the deprotonation of 2SAC's three carboxylic acids. Five protonation constents were found for 2SGT, corrosponding to the four carboxylic acids and the amine. The equilibrium equations for

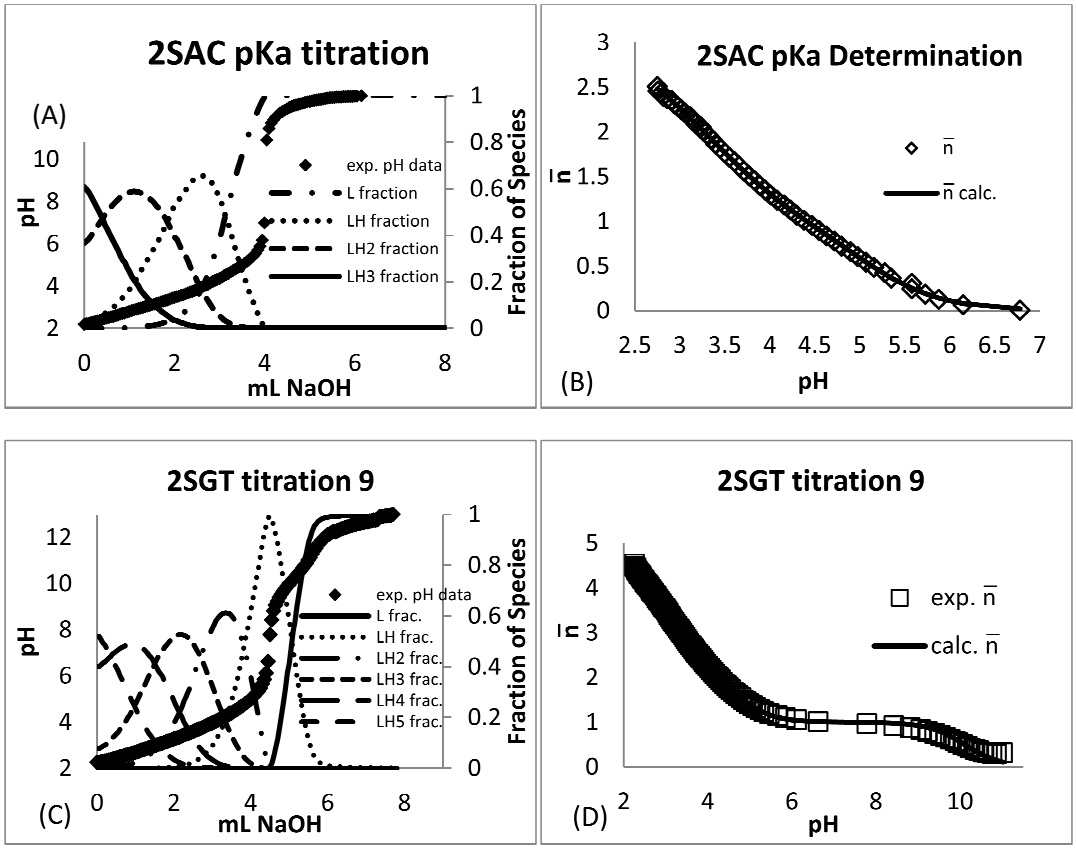

Figure 30: Effects of added base on pH of solutions containing 2SAC and 2SGT

these reactions can be described by Equation 23 where LH_i is an acidic protonatied species L, with *i* acidic protons.

$$LH_i + H^+ \rightleftharpoons LH_{i+1} \tag{23}$$

The equilibria, described by equation 23, are subject to mass balance described in Equation 24 and are characterized by the protonation equilibrium constants (K_{Hi}, Equation 25) can be found.

$$[L]_{total} = \sum_{i=0} LH_i \tag{24}$$

$$K_{Hi} = \frac{[LH_{i+1}]}{[LH_i][H^+]} \tag{25}$$

Protonation constants for 2SAC and 2SGT were determined from the titration curves using the $\bar{n}$ method.[30] According to this method $\bar{n}$ is defined as the average number of acidic protons bound to an acid and is described by Equation 26.[30] Experimentally $\bar{n}$ can be found at any point in the titration by subtracting the number of free protons from the total number of available protons and dividing by the total ligand concentration. As described in Equation 27, $\bar{n}$ is calculated by adding the number of acidic protons on the acid, j (e.g. for a diprotic acid j=2), to the number of protons from the dissociation of water minus the amount of sodium hydroxide added minus the amount of free protons. By rearranging equations 24 and 25 $\bar{n}$ can also be found using protonation constants and pH, and is given by Equation 28 (β is the term for the cumulative protonation constant e.g. $\beta_2 = K_{H1}K_{H2}$).

$$\bar{n} = \frac{\sum i[LH_i]}{[L]_{total}} \quad (26)$$

$$\bar{n} = \frac{j[L]_{total} + [OH^-] - [Na^+] - [H^+]}{[L]_{total}} \quad (27)$$

$$\bar{n} = \frac{\beta_i[H^+]}{\sum_{i=0} \beta_i[H^+]^i} \quad (28)$$

Protonation constants were estimated using Solver® (Excel 2011) to minimize the sum of the squares of the residuals between the experimental and calculated values of $\bar{n}$. Experimental and calculated values of $\bar{n}$ after optimization are compared in panels B and D of Figure 28 for representative titrations of 2SAC and 2SGT respectively.

Stoichiometry of copper(II)-ligand complexes. Stoichiometries of the metal ligand complexes were determined using Job's method of continuous variation.[32] We measured the absorbance spectra of solutions containing different metal to ligand ratios while keeping the total concentration of the two species constant. As shown in Figure 31, both 2SGT and 2SAC showed the greatest absorbance when the ratios of copper

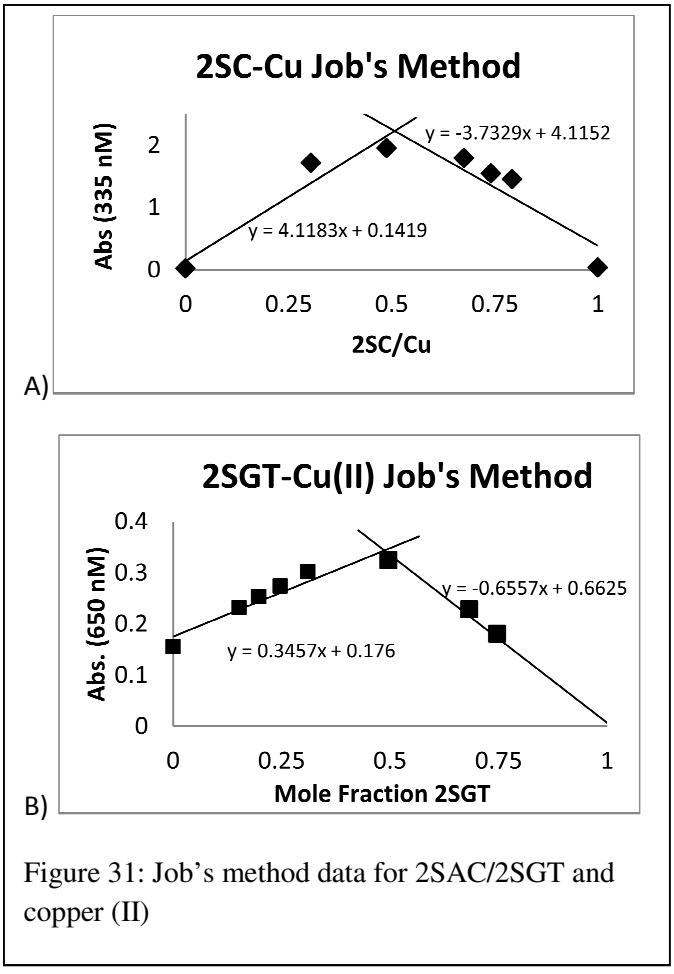

Figure 31: Job's method data for 2SAC/2SGT and copper (II)

to ligand was 1 to 1. The experiments were performed at a pH of 5 so that the carboxylic acids of the major species were fully deprotonated. Since the stoichiometry for both metal complexes was found to be 1:1 the equilibrium equations for the 2SAC/2SGT copper binding is given by Equations 29 and 30. From the equilibrium equations, equations for the stability constants ($K_{2SAC\text{-}Cu}$ and $K_{2SGT\text{-}Cu}$) are given by Equations 31 and 32.

$$2SAC^{3-} + Cu^{2+} \rightleftharpoons (2SAC - Cu)^{-} \quad (29)$$

$$2SGT^{4-} + Cu^{2+} \rightleftharpoons (2SGT - Cu)^{2-} \quad (30)$$

$$K_{2SAC-Cu} = \frac{[(2ASC - Cu)^{-}]}{[2SAC^{3-}][Cu^{2+}]} \quad (31)$$

$$K_{2SGT-Cu} = \frac{[(2SGT - Cu)^{2-}]}{[2SGT^{4-}][Cu^{2+}]} \quad (32)$$

Determination of copper/ligand complex stability constants. Stability constants for copper (II) binding by 2SAC and 2SGT were determined by titrations of equal molar ligand and copper (II) (2 mM each) with sodium hydroxide whilst monitoring both pH (Hanna Instruments HI2215) and the UV/Vis spectra (BW-Tek *i*-Trometer using a BD5130 UV/Vis/NIR light source). A detailed description of the procedure is given in Appendix C. The ionic strength was maintained at 0.1 with either KNO_3 or KCl. Stability constant were demined from the titration data using a method similar to Bjerrum's.[30] While we attempted to determine the stability constants for 2SAC and 2SGT complexes of iron (II), a precipitate formed at approximately pH 2-3. The copper complexes of 2SAC and 2SGT were more amenable to work with, remaining soluble up to a pH of approximately 6 for 2SAC and throughout the titration (pH of 13) for 2SGT.

The concentrations of species present during the titration were determined from UV/Vis spectra using an Alternating Least Squares Multi Curve Resolution (ALS-MCR) algorithm in the Matlab program (Appendix A). This algorithm begins be estimating extinction coefficients of absorbing species (using the initial and finial spectra from the titration). Concentrations of each species at each point in the titration were calculated using Beer's law, using the experimental spectra and the estimated extinction coefficients of for the pure species. Constraints were applied to prevent the calculated concentrations from becoming negative and to maintain mass balance. The spectra for the pure components were then recalculated from the experimental spectra using the newly found concentrations. The calculated concentrations and extinction coefficients were used to predict the observed spectra. The difference between the experimental and calculated spectra was minimized by repeating this process until the calculated spectra were within a specified tolerance of the experimental spectra.

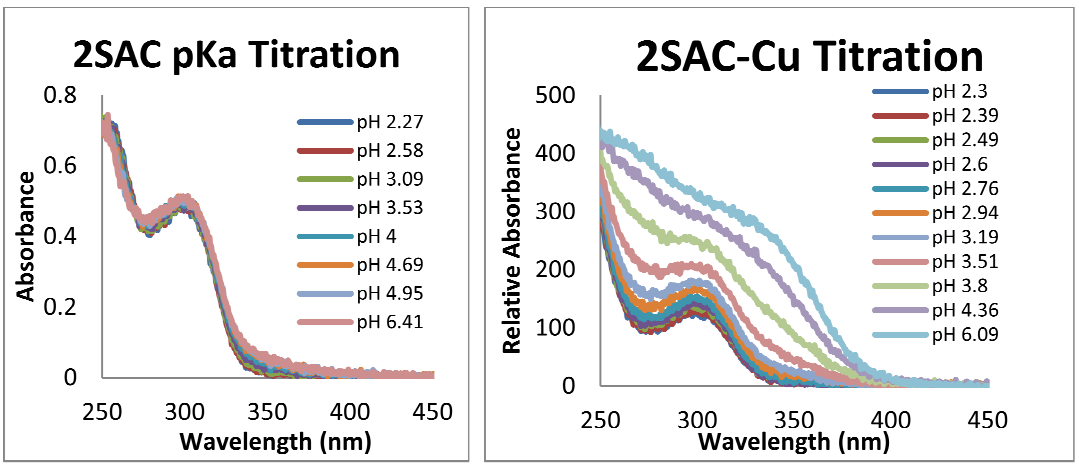

Figure 32: UV/Vis spectra for A)2SAC B) 2SAC and copper (II).

The ALS-MCR algorithm requires that the number of absorbing species be known. A Principal Component Analysis (PCA) of the spectra was performed to determine the number of absorbing species present when 2SAC is titrated in the presence or absence of copper (II). This analysis was described earlier for flavonol aggregation (algorithm given in Appendix A). As

shown in Figure 32A, the UV/Vis spectra of 2SAC in the absence of copper (II) changes very little during titration with base. From this experiment the principal component analysis found that 96% of the spectra could be accounted for with just one absorbing component (Figure 33). In contrast, two components are required to account for the spectra when one equivalence of copper is present (Figure 32B). In this experiment, 97% of the spectra could be accounted for with two species. No significant increase in the fit was observed with more than two species for either titration. This indicates that 2SAC and 2SAC-Cu are the only two absorbing species are present in the 2SAC-Cu titrations.

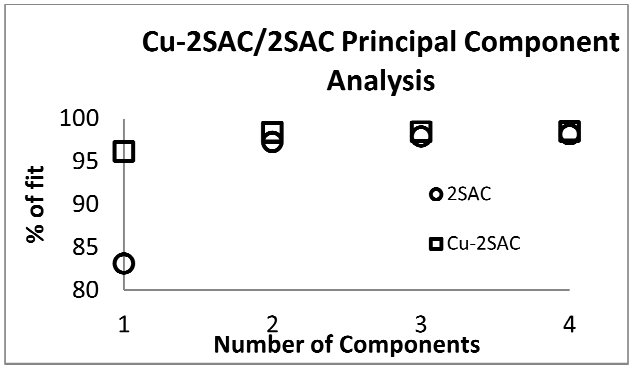

Figure 33: Principal component analysis for 2SAC and 2SAC-Cu(II) spectra

The concentrations of each absorbing species in the titrations were calculated using the ALS-MCR algorithm. Figure 34 shows the fraction of species obtained from this calculation on the 2SAC-Cu data and is shown overlaid on the experimental pH data for one of the titrations.

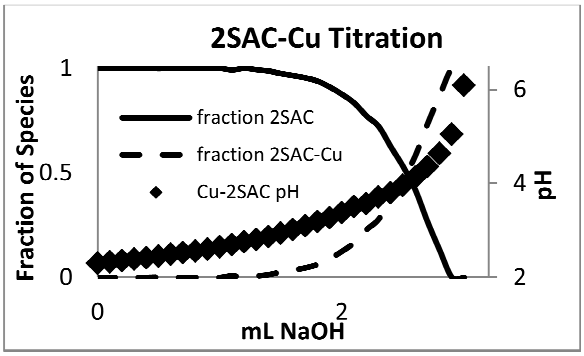

Figure 34: Fraction of each species calculated for titrations of 2SAC-Cu overlaid on the experimental pH data.

From the spectra, concentration of the metal complex ([*L-metal*]) can be determined for each pH and, the concentration of unbound ligand ($[L]_{free}$) can be found from the mass balance equation (Equation 33).

$$[L]_{free} = [L]_{total} - [L - metal] \quad (33)$$

The concentration of the unbound ligand in any of its protonation states can be found by Equation 34 which uses $[L]_{free}$, the pH, and the protonation constants.

$$\boldsymbol{\alpha}_0 = \frac{[LH_i]}{[L]_{free}} = \frac{\beta_{Hi}[H^+]^i}{\sum_{j=0}\beta_{Hi}[H^+]^i} \quad (34)$$

Where $\boldsymbol{\alpha}$ is the fraction of species, β_{Hi} is the i^{th} cumulative protonation constant (*e.g.* $\beta_{H2} = K_{H0} * K_{H1} * K_{H2}$), and $\beta_{H0} = 1$.

To find the copper (II) stability constants described in Equations 31 and 32 another term $\boldsymbol{\theta}$ is introduced, which is analogous to $\bar{\boldsymbol{n}}$ and is defined as the concentration of metal bound ligand divided by the total metal concentration. For a 1:1 metal to ligand complex $\boldsymbol{\theta}$ is given by Equation 35 (where L^{n-} is either $2SAC^{3-}$ or $2SGT^{4-}$ and K_s is either $K_{2SAC\text{-}Cu}$ or $K_{2SGT\text{-}Cu}$).

$$\boldsymbol{\theta} = \frac{[L - metal\,]}{[metal]_{total}} = \frac{K_s[L^{n-}]}{1 + K_s[L^{n-}]} \quad (35)$$

$$\boldsymbol{\theta} = K_s([L^{n-}] - \boldsymbol{\theta}[L^{n-}]) \quad (36)$$

By rearranging Equation 35 to obtain Equation 36 there should be a linear relationship between $\boldsymbol{\theta}$ and ($[L^{n-}]$- $\boldsymbol{\theta}[L^{n-}]$) with the slope being equal to K_S. Figure 35 shows a representative graph.

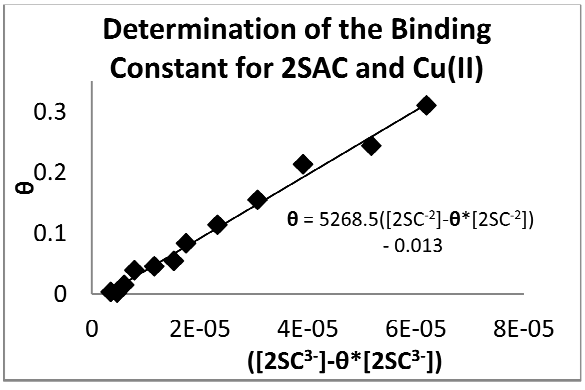

Figure 35: Slope of the above graph gives the binding constant between 2SAC and copper (II)

Alternating least squares multi curve resolution analysis. Spectral data from the titrations were loaded into a matrix in Matlab. A matrix was made of the estimated extinction coefficients for each absorbing component in solution. The ALS-MCR algorithm (Appendix A) was used to adjust extinction coefficients and concentration values to obtain the best fit for the experimental spectra.

Determination of solution access to copper using ^{19}F NMR. Solution access to copper in 2SAC-Cu and 2SGT-Cu was studied by methods similar to those described above for SOD inhibition. In this experiment the relaxation of the ^{19}F NMR signal of 20 mM fluoride by 1 μM copper (II) was monitored as a function of added ligand. The experiments for 2SAC-Cu and 2SGT-Cu were both conducted at pH 5 using an acetate acid buffer prepaid as described above.

2SAC-Cu superoxide redox cycling. The effect of superoxide on the steady state ratio of Cu^{2+} to Cu^{+} was determined by measuring the effects of the superoxide generating compounds NADH/PMS on the ^{19}F NMR relaxation rate of the fluoride ion. A concentrated sample of $Cu(NO_3)_2$ was added to a pH 5.0 NMR buffer (preparation described above) until the ^{19}F NMR relaxation rate was around 100 s^{-1}. Aliquots of NADH and PMS solutions were added to 500 μL samples of buffer/Cu solution. The final concentrations of NADH and PMS were 78 and 3.3 μM respectively. The added NADH and PMS solutions had a negligible effect on the total volume. The time after the PMS addition was monitored using a stopwatch. The relaxation rate (R_2) of the ^{19}F resonance was determined periodically using the CPMG experiment (described earlier) until a stabile value was obtained. For the 2SAC-Cu data the procedure was repeated using 500 μL of

the same stock buffer/Cu solution except 2SAC was added from a concentrated solution to give 1 mM 2SAC with negligible change in volume.

2SAC-Cu/2SGT-Cu cyclic voltammetry. Cyclic voltammograms were recorded using a 2 mm^2 gold working electrode and Ag/AgCl reference electrode. Ionic strength maintained at 0.1 with acetate buffer. A scan rate of 50 mV/s was used for all voltammograms. The pH was maintained at pH 5 with a 0.1 M acetate buffer.

2SAC-Cu/2SGT-Cu hydroxyl radical formation. H_2O_2 was added to a solution containing 2 mM of 2SAC or 2SGT, 0.2 mM Cu^{2+}, 20 µM rhodamine B, and 0.1 M acetate solution at pH 5. The final concentration of H_2O_2 was 3.5%. The rhodamine B absorbance at 555 nM was recorded over the course of approximately 20 minutes.

Application of Methods to Study Metal Ion Participation in Complication of Diabetes

Results and Discussion

2SAC and 2SGT acid dissociation constants. From the titration data we were able to determine three protonation constants for 2SAC and five were found for 2SGT. The pK_a ($-\log(1/K_H)$) values corresponding to these protonation constant are given in Table 5. The three pK_a values found for 2SAC most likely arise due to deprotonation of the three carboxylic acids.

Species	pK_{a1}	pK_{a2}	pK_{a3}	pK_{a4}	pK_{a5}
2SAC	2.57 ± 0.06	3.48 ± 0.03	4.6 ± 0.2	-	-
2SGT	2.43 ± 0.07	3.13 ± 0.02	3.83 ±0.03	4.898 ± 0.001	10.25 ± 0.09

Table 5: pK_a values for 2SAC and 2SGT found from titrations with NaOH

For 2SGT, the first four pK_a values are thought to correspond to the four carboxylic acids while the fifth pK_a is thought to correspond to the amine. These assignments are consistent with known pK_a values for carboxylic acids and amines (typically found between 2 and 5, and between 9 and 10 respectively).[34]

2SAC-Cu stability constant. Titrations of 2SAC in the presence and absence of copper (II) allowed the determination of the 2SAC-Cu stability constants. The stability constant for the 2SAC copper (II) complex was found to be $\log(K_{Cu(II)\text{-}2SAC}) = 3.59 \pm 0.05$ (results given in Table 6). This value makes the stability constant for 2SAC-Cu an order of magnitude larger than the stability constant for the corresponding complex of succinic acid ($\log(K_s) = 2.6$).[25] This increased stability reflects an increased negative charge on the ligand and suggests that 2SAC may coordinate to the copper by more than just the succinic acid moiety.

complex	$\log K_s$ I = 0.1 M
Cu(II)-2SAC	3.59 ± 0.05[a]
Cu(II)-2SGT	10.9 ± 0.2[b]

Table 6. Metal binding constant for 2SAC and 2SGT

a)KNO_3 salt b) KCl salt

2SGT-Cu stability constant. The spectral data indicates that more than one metal/ligand species was present over the course of the 2SGT-Cu(II) titrations. As shown in Figure 36, the spectra for 2SGT-Cu(II) titrations did not display isosbestic behavior. Panel B shows normalized absorbance (to the maximum for each wavelength) at 350 and 600 nm (red triangles and blue squares respectively) over laid on the pH data from the titration. The absorbances at these two

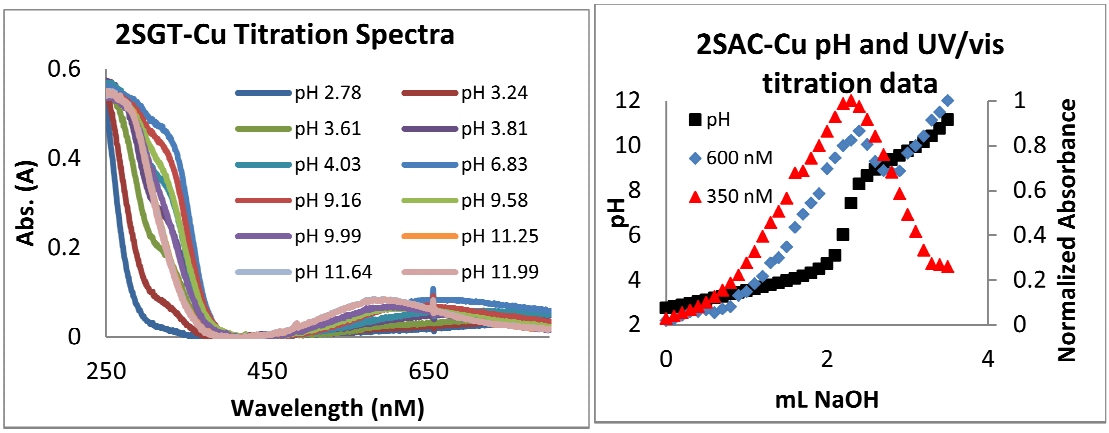

A) B)

Figure 36: A) UV/Vis spectra for 2SGT-Cu(II) titration. B) Selected normalized absorbance at selected wavelengths overlaid on experimental pH data for a 2SGT-Cu(II) titration.

wavelengths increase with added base until the first five equivalences of NaOH were added. If there were only one species, the absorbance would either continue to increase or level off at this point. Instead, we observed a decrease in the absorbance from this equivalence point indicating at least a one additional species is formed.

$$(2SGT - Cu)^{2-} \rightleftharpoons (2SGT - Cu)^{4-} + 2H^{+} \qquad (37)$$

The pH data obtained from titrations of 2SGT and copper (II) (Figure 37), displayed inflections at 5 and 7 equivalents of NaOH, indicating shows that 2SGT has two additional acidic protons in the presence of copper (II) than in its absence. We attribute this behavior to coordination of copper by two peptide amide nitrogens. This is consistent with a crystal structure

that showed glutathione binds copper via two amide nitrogens when crystals were obtained at pH 11.[33] It is likely 2SGT binds copper in a similar manner under alkaline conditions. If this is occurring, then the equilibrium for the second species is given in Equation 37. At lower pH the complex involves the deprotonated carboxylic acid and amine groups ($(2SGT\text{-}Cu(II))^{2-}$, Equation 30).

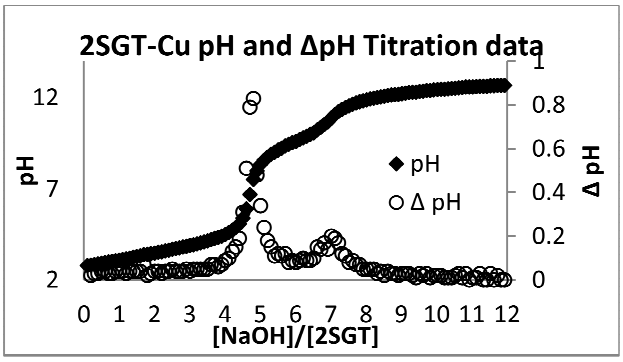

Figure 37: Experimental titration of 2SGT with copper shows equivalence points at 5 and 7 equivalences of NaOH.

The amide bound 2SGT-Cu(II) species ($(2SGT\text{-}Cu(II))^{4-}$) is only likely to be of physiological importance since it is formed at high pH. The binding constant for the $(2SGT\text{-}Cu(II))^{2-}$ complex was established using the method described above for 2SAC-Cu(II). Only data from samples with a pH less than 6.5 was used in the calculation to ensure that $(2SGT\text{-}Cu(II))^{4-}$ had a negligible influence. Figure 38 shows the distribution of species determined from this calculation overlaid on the pH data. The binding constant was determined to be $\log(K_{2SGT\text{-}Cu(II)}) = 10.9 \pm 0.2$ from this distribution of species.

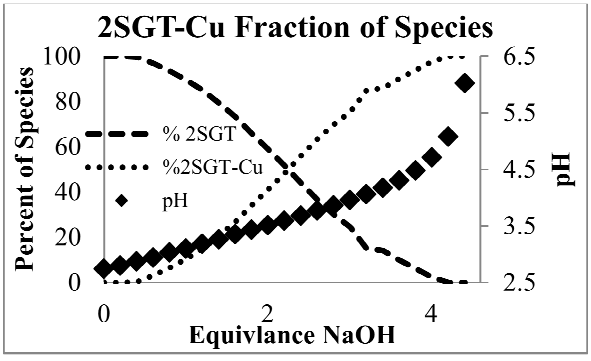

Figure 38: Fraction of each species calculated for titrations of 2SGT-Cu overlaid on the experimental pH data.

Electrochemistry of the 2SAC and 2SGT copper complexes. The electrochemistries of 2SAC-Cu and 2SGT-Cu were studied by cyclic voltammetry. Figure 39A shows the voltammogram for copper in an acetate buffer (pH 5) without added ligand. There are two

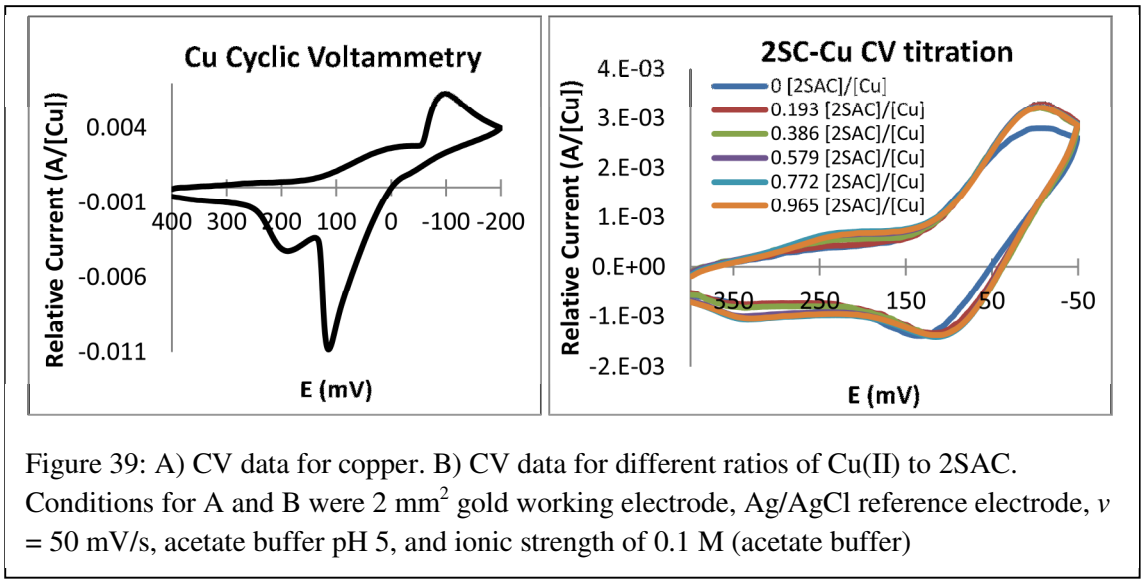

Figure 39: A) CV data for copper. B) CV data for different ratios of Cu(II) to 2SAC. Conditions for A and B were 2 mm^2 gold working electrode, Ag/AgCl reference electrode, *v* = 50 mV/s, acetate buffer pH 5, and ionic strength of 0.1 M (acetate buffer)

cathodic and two anodic peaks. We attribute these peaks to the reduction of copper (II) to copper (I) then to copper metal in two discrete steps. The reverse sweep shows the oxidation of copper metal to copper (I) then to copper (II) again in two discrete steps. Because we are interest in the interactions of 2SAC with copper (II) and copper (I), voltammograms were limited to a potential range of 400 to -50 mV range to prevent the deposition of copper metal. Figure 39B shows voltammograms in this potential range for different ratios of Cu(II) to 2SAC. The similarity of the voltammograms indicates that there are no significant differences between the redox activities of the Cu-2SAC complex and free copper (discussed below). Since the reduction potential for the Cu(II) to Cu(I) is 153 mV, and within the range specified

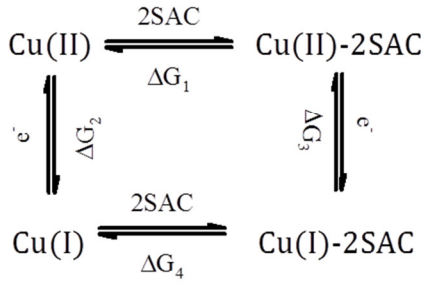

Figure 40. Hesse's Law diagram for the reaction of 2SAC with Cu(II) and Cu(I)

by Boukhalfa *et al*., thermodynamically the 2SAC-Cu complex should be able to catalyze the Haber-Weiss Cycle (Equations 1-4). We have confirmed this prediction experimentally (discussed later).[34,29]

The similarity of the voltammograms in the presence and absence of 2SAC also indicates that the stability constants for the copper (II) and copper (I) complexes of 2SAC are similar. This is illustrated by considering the reaction diagram shown in Figure 40. Hess's law requires that ΔG_4 is related to ΔG_1 according to Equation 38. Since the voltammograms were not affected by addition of 2SAC, ΔG_2 must be similar to ΔG_3 and ΔG_4 must be similar to ΔG_1 (Equations 38-40).

$$\Delta G_{4\,=} \; -\Delta G_2 + \Delta G_1 + \Delta G_3 \tag{38}$$

$$\Delta G^0 = -nFE^0 \tag{39}$$

$$\Delta G^0 = -RT \ln K \tag{40}$$

The voltammograms recorded for solutions containing 2SGT and copper (II) are shown in Figure 41. These voltammograms were run over the larger potential range then for 2SAC because the cathodic peak observed at approximately 10 mV in the 2SAC and copper voltammograms was not as pronounced in the 2SGT and copper voltammograms. As shown in Figure 41, voltammograms of solutions containing 2SGT and

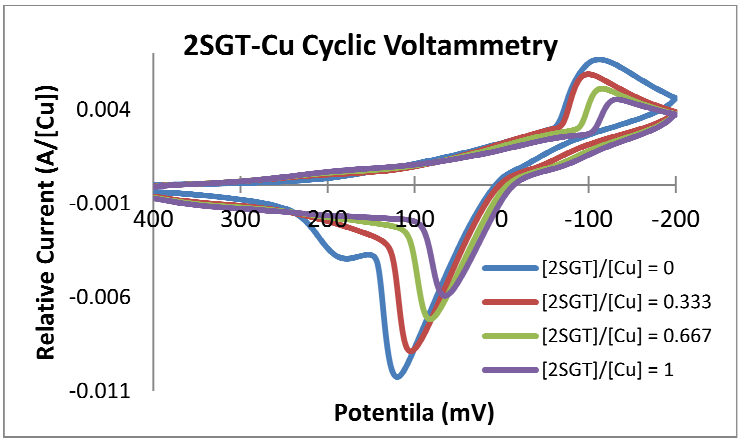

Figure 41: CV data for different ratios of 2SGT and Cu(II). Conditions were 2 mm^2 gold working electrode, Ag/AgCl reference electrode, v = 50 mV/s, acetate buffer pH 5, and ionic strength of 0.1 M (acetate buffer) at pH 5.

copper (II) show a cathodic peak decreasing in intensity with added 2SGT. Also, there are two anodic peaks shown in the pure copper (II) sample. With the addition of 2SGT the anodic peaks shift to more negative potentials with the peak initially at c.a. 190 mV almost disappearing in the 1:1 sample. We believe the difference between the voltammograms in the two experiments is due to kinetic effects which may have been due to different surface preparation of the electrodes. Since addition of the ligands to copper show mostly kinetic effects in the voltammograms, rather than significant changes in the redox potential, effort was not put into reconciling the differences between the two experiments.

2SAC-Cu and 2SGT-Cu metal access determined by ^{19}F NMR. Metal access in copper complexes of 2SAC and 2SGt were studied by 19F NMR. As shown in figure 42A, the NMR relaxation activity of 1 μM copper (II) decreases with increasing concentration of 2SAC. However, even with three orders of magnitude higher concentration 2SAC than copper (II) there still remains around 10 % activity. This result indicates that the 2SAC-Cu(II) species must also contribute to the relaxation of the fluoride.

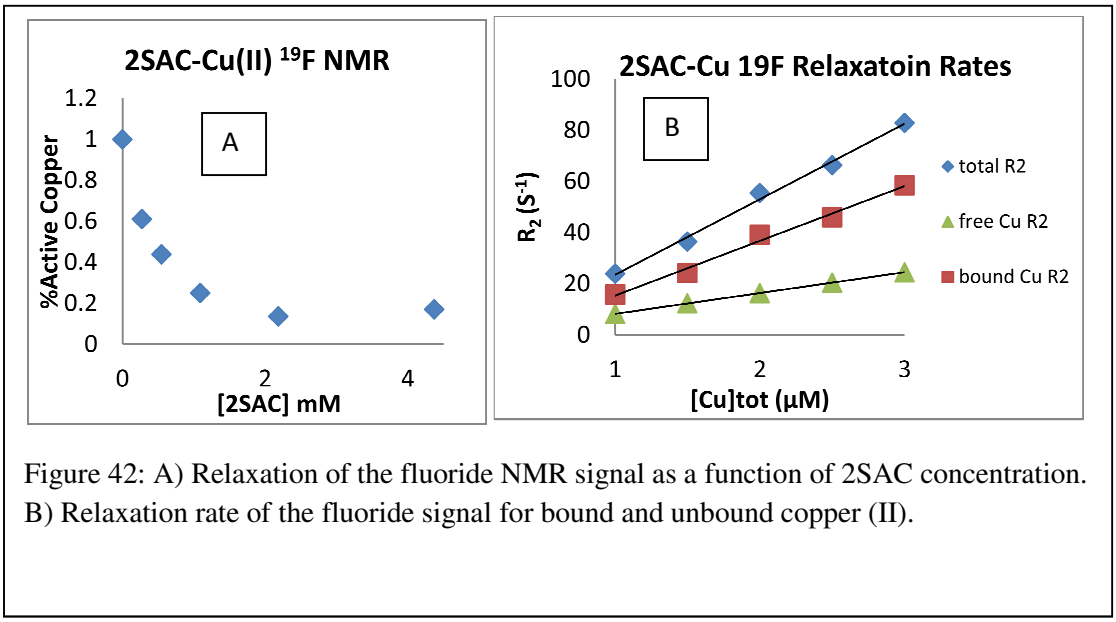

Figure 42: A) Relaxation of the fluoride NMR signal as a function of 2SAC concentration. B) Relaxation rate of the fluoride signal for bound and unbound copper (II).

A separate experiment was run to determine the extent to which 2SAC-Cu(II) species contributes to ^{19}F relaxation. In this experiment the concentration of 2SAC was held constant at 10 mM and the concentration of copper (II) was varied from 1 μM to 3 μM (Figure 42B). The concentration of unbound copper was calculated using the binding constant for 2SAC and copper (II). The contribution of unbound copper (II) to the relaxation rate is shown in Figure 42B as green triangles. The difference between the observed relaxation rate (blue diamonds) and that due to free copper (shown as red squares in Figure 42B) is due to the relaxation of the fluoride by the 2SAC-Cu(II) species. Using the calculated concentrations of the free copper (II) and the know relaxation rate of free copper (*c.a.* 2.5 X 10^8 R_2/M) the molar relaxation rate of 2SAC-Cu(II) was found to be 2.0 X 10^7 R_2/M.

Since the 2SAC-Cu(II) species causes relaxation of the fluoride, we conclude that fluoride ions must be able to access the bound copper. By analogy, other small molecules such as the superoxide ion and H_2O_2 should be able to access the copper ion in the 2SAC-Cu complex.

The affets of 2SGT on the ^{19}F NMR relaxation enhancement of copper (II) is shown in Figure 43. This experiment shows that upon addition of the 2SGT, NMR relaxation the activity of the copper drops to essential zero very quickly (60 μM and higher 2SGT with 2 μM Cu(II) gives less than 10 % activity). This result indicates that the 2SGT ligand wraps around the copper (II) ion, preventing access to the fluoride ion. By analogy, other small molecules such as superoxide or H_2O_2 would also not be able to contact the copper in the 2SGT-Cu complex.

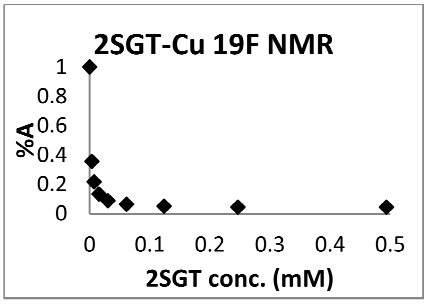

Figure 43. Relaxation of the fluoride signal as a function of 2SGT concentration.

Reactions of superoxide with 2SAC-Cu. Using the ^{19}F assay described earlier, we were able to determine that 2SAC-Cu is reduced to copper (I) by superoxide but is not re-oxidize. Thus 2SAC-Cu will not catalyze the disproportionation of superoxide. In this experiment we used NADH/PMS to generate superoxide and monitored its effect on ^{19}F relaxation by either free copper (II) or 2SAC-Cu(II). As described earlier, redox cycling would result in a steady state concentration of copper (II) which would be detected from its relaxation activity. Figure 44 shows that upon addition of NADH/PMS relaxation rate drops to essentially zero, indicating the copper (initial in its +2 oxidation state) is reduced to copper (I), for both the control and sample with 2SAC.

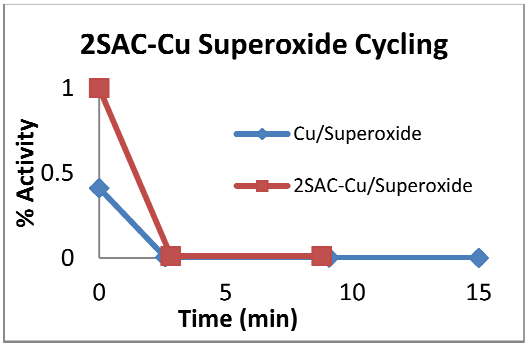

Figure 44. Upon addition of superoxide generating reagents the copper (II) is reduced to copper (I) and is not re-oxidized.

Hydroxyl radical formation. We investigated the ability of 2SAC-Cu and 2SGT-Cu to catalyze hydroxyl radical formation from H_2O_2. These experiments show that 2SAC-Cu will catalyze the formation of the hydroxyl radical from H_2O_2 while the 2SGT-Cu compound will not.

The formation of hydroxyl radicals was investigated by monitoring the 555 nm absorbance of rhodamine B. It has been demonstrated that reactions with hydroxyl

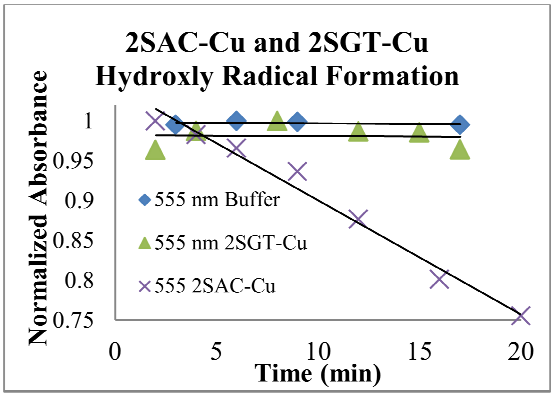

Figure 45. rhodamine B absorption at 555 nm. In the presence of hydroxyl radical producing species the absorbance of rhodamine B decreases.

radicals bleaches the 555 nm absorbance of rhodamine B.[35] Figure 45 shows the experimental data from solutions containing 2SAC-Cu(II), 2SGT-Cu(II), and a control sample. Upon addition of H_2O_2 the rhodamine B absorbance at 555 nm decreases in the sample containing 2SAC-Cu(II) but not in the samples containing 2SGT-Cu. It has been reported that certain metal complexes catalyze the disproportionation of $2H_2O_2$ to $2H_2O$ and O_2 via a radical mechanism.[37] Our results suggest that 2SAC-Cu catalyzes the disproportionation of H_2O_2 via a radical mechanism as describe by Equations 41 and 42. In the case of 2SGT-Cu, no significant change in the rhodamine B absorption at 555 nm was observed. This result indicates that 2SGT-Cu does not catalyze the formation of the hydroxyl radical. This result combined with the ^{19}F result suggests that metal accessibility is necessary for catalytic reactions that form the hydroxyl radical.

$$2Cu^{2+} + H_2O_2 \rightarrow 2Cu^{+} + O_2 + 2H^{+} \quad (41)$$

$$Cu^{+} + H_2O_2 \rightarrow Cu^{2+} + OH^{-} + OH\cdot \quad (42)$$

Application of Methods to Study Metal Ion Participation in Complication of Diabetes

Conclusion

We have synthesized the compounds 2SAC and 2SGT and have determined their copper (II) binding constants. Using ^{19}F NMR assays, we have shown that the metal in 2SAC-Cu is accessible to small atoms/molecules while the metal in 2SGT-Cu is not. This accessibility allows 2SAC-Cu to catalyze further reactions involving small molecules. We demonstrated that 2SAC-Cu(II) reacts with superoxide to give the corresponding copper (I) complex. We have also shown

that 2SAC-Cu(I) reacts with H_2O_2 to give the hydroxyl radical. Since the Haber-Weiss reaction is the sum of these reactions, these experiments indicate that 2SAC-Cu will catalyze the Haber-Weiss reaction. The inaccessibility of the metal in the 2SGT-Cu species appears to prevent metal catalyzed reactions involving superoxide and H_2O_2. These results suggest that the 2SC-Cu complexes in vivo might catalyze the Haber-Weiss reaction depending on whether other coordinating groups are present in the specific ligand.

REFERENCES

1) Gutteridge, J.M.C., *FEBS Letters*, **1985**, 185, 19

2) Richter, C., Gogvadze, V., Laffranchi, R., Schlupbach, R., Schweizer, M., Sutter, M., Walter, P., Yaffee, M., *Bichim. Biophys. Acta.,* **1995**, 1271, 67.

3) Radi, R., Beckman, J. S., Bush, K. M., Freeman, B. A., *J. Biol. Chem.*, **1991**, 266, 4244

4) Rakhit, R., Cakrabartty, A., *Bichim. Biophys. Acta.*, **2006**, 1762, 1025

5) Hileman, E.O., Liu, J., Albitar, M., Keating, M. J., Huang, P., *Cancer Cemother. Pharmacol*., **2004**, 53, 209-219.

6) a) Piddington, D. L., Fang, F. C., Laessing T., Cooper A. M., Orme I. M., Buchmeier N. A., *Infect. Immun.*, **2001**, 69, 4980-4987. b) Edwards K.M., Cynamon M.H., Voladri R.K., Hager C.C., DeStefano M.S., Tham K.T., Lakey D.L., Bochan M.R., Kennodle D.S., *Am. J. Respir. Crit. Care Med.,* **2001**, 164, 2213-2219. c) Seyler, R. W., Olson, J., W., Maier, R. J., *Infect. Immun*., **2001**, 69, 4034-440. d) Nathan C., Shiloh M.U., *Proc. Natl. Acad. Sci*., U S A., **2000**, 97, 8841-8848.

7) Kohanski, M. A., Dwyer, D. J., Hayete, B., Lawrence, C.A., Collins, J. J., *Cell*, **2007**, 130, 797-810.

8) Huang, P., Feng, L., Oldham, E. A., Keating, M. J., Plunkett, W., *Nature*, **2000**, 407, 390-395.

9) Ewing, J.F., Janero, D.R*., Anal. Biochem*, 1995, 232, 243

10) Soulere, L., Delplace, P., Davioud-charvet, E., Py, S., Sergheraert, C., Perie, J., Richard, I., Hoffmann, P., Dive, D., *Bioorg. Med. Chem*., **2003**, 11, 4941-4944.

11) Viglino, P., Rigo, A., Stevanato, R., Ranierei, G. A., Rotilio, G., Calabrese, L., *J. Mag. Res*., **1979**, 34, 265-274.

12) Valentine, J. S., *Biological Inorganic Chemistry: Structure and Reactivity*, Gray, H. B., Stiefel, E. I., valentine, J. S., Bertini, I., editors. University Science Books, 2007, Chapter XI, 331.

13) Webb, M. R., Ebeler, S.E., *Biochem. J.,* **2004**, 384, 527-541.

14) Matter, W.F., Brown, R. f., Vlahos, C. J., *Biochem. Biophys. Res. Comm*., **1992**, 186, 624-631. b) Davies, S. P., Reddy, H., Caivano, M., Cohen, P*., Biochem. J*., **2000**, 351, 95-105.

15) McGovern, S. L., Cselli, E. Grigorieff, N., Shoicket, B. K., *J. Med. Chem*., **2002**, 45. 1712-1722.

16) Lucia Banci, Ivano Bertini, Claudio Luchinat, Maria Silvia Viezzoli, *Inorg. Chem.*, **1993**, *32* (8), 1403–1406

17) Combined Chemical Dictionary, **2011**, vol. 15.1, retrieved from http://ccd.chemnetbase.com/

18) Huheey, J.E., Keiter, E.A., & Keiter, R.L. (1993*). Inorganic chemistry: principles of structure and reactivity*. HarperCollins College Publishers.

19) Pietta P., *J. Nat. Prod*, **2000**, 63, 1035-1042

20) Van Acker, S. A. B. E., Van Der Berg, D. J., Tromp, M. N. J. L., Griffione, D. H., Van Bennekom., W. P., Van Der Vijgh, W. J. F., Bast A., *Free Radical Biology and Medicine*, **1996**, 20(3), 331-342

21) Khare, S. D., Dokholyan, N. V., *Proc. Natl. Acad. Sci. USA*, **2006**, 103(9), 3147–3152

22) Vlassara, H., Palace, M.R., *Mt. Sinai J. Med.* 70, **2003**, 232-241

23) Baynes, J.W., *Clin. Chem. Lab. Med*. 41, **2003**, 1159-1165

24) Alderson, N.L., Wang, Y., Blatnik, M., Frizzell, N., Walla, M.D., Lyons, T.J., Alt, J., Carson, J.A., Nagi, R., Thorpe, S.R., Bayens, J.W., *Arch. Bio. Biophy.*, 450, **2006**, 1-8

25) Martell, A. E., and R. M. Smith. *Critical Stability Constants. Vol. 3: Other Organic Ligands.* New York, NY: Plenum, **1977**, 108.

26) Arrington, M.E., *Superoxide Dismutase inhibitor Screening and Characterization using 19F NMR,* Master's of Science Thesis*,* Western Carolina University, **2010**.

27) Brown, J. E., Khodr, H., Hider, R. C., Rice-Evans, C.A., *Biochem*. J., **1998**, 330, 1173-1178.

28) Perron, N. R., Hodges, J. N., Jenkings, M., Brumaghim, J. L., *Inorg. Chem*., **2008**, 47, 1653-1661.

29) Boukhalfa H., Crumbliss A. L., *BioMetal*s, **2002**, 15, 325-339.

30) Billo, E. J., *Excel for Chemist: a Comprehensive Guide*. (2nd ed.). New York: Wiley-VCH, **2001**, 329-372.

31) Maritim A. C., Sanders R. A., Watkins J. B., *J Biochem Molecular Toxicology*, **2003**, 17(1), 24-38.

32) Hargis, Larry. *Analytical Chemistry Principles and techniques*. Englewood Cliffs: Prentice-Hall, **1988**, 424-425.

33) Miyoshi K., Sugiura Y., Ishizu K., Iitaka Y., Nakamura H., *J. Am Chem. Soc.* 102(19), **1980**, 6130-6136.

34) Haynes, W. M. *CRC Handbook of Chemistry and Physics*. 92nd. Boca Raton: CRC Press, **2011**. eBook. <http://www.hbcpnetbase.com/>.

35) Yu F., Xu D., Lei R., Li N., Li K. A., *J. Agric. Food Chem.*, **2008**, 56, 730-735.

36) Harisch G., Kretschmer M., Richter T., Pickel M., *J. Vet. Med.*, **1989**, A 36, 576-584

37) Haber F., Weiss J., *Proc. R. Soc. Lond.*, **1934**, 147, 332-351

APPENDIX A

(Matlab Code)

Alternating Least Squares Multi Curve Resolution

```
%this is the als engine to interatively refine guesses in C or K matrix
% currently this function only works with Ki guesses
%
%usage:  [K, C] = alsKgf(A,Ki,options,tolerance)
% notes:
% all spectra are row vectors
% options is a column vector of flags
% $$$  options = [1;%non negativity in C
% $$$             1;%non negativeity in K
% $$$             1;% closer in C
% $$$             1;% unassigned
% $$$             1;% unassigned
% $$$             1;% unassigned
% $$$             1;% unassigned
% $$$             1];% unassigned


function [K, C] = alsKgf(A,Ki,options,tolerance)
Ki = mkrow(Ki);
[npc, npts] = size(Ki);
[nspec, npts] = size(A);

C = zeros(nspec,npc);
K = Ki;
%begin convergence test loop
decide = 10000000;
RSDold = 10000000;
while abs(decide) > tolerance

 C = A*K'*inv(K*K');
 %closer constraint for C
 if (options(3) == 1)
   for i = 1:nspec
     C(i,:) = ccr(C(i,:),1)';
   end
 end
 %non negative constraint in C
 if (options(1) == 1)
   for i = 1:npc
     C(:,i) = cnn(C(:,i))';
   end
 end
 K = inv(C'*C)*C'*A;
 %non negative constraint in K
  if (options(2) == 1)
```

```
   for i = 1:npc
     K(i,:) = cnn(K(i,:))';
   end
 end
 Ag = C*K;
 RSD = sum(sqrt((sum(A-Ag).^2)/(nspec-2)));
 decide = (RSD-RSDold)*100;
 disp([num2str(abs(decide(1,1))) ' must be less than '
num2str(tolerance)])
 RSDold = RSD;   %see Anal. Chem. vol 72 no 9 1956-1963
End
```

Non-Negativity Constraint

```
%this function will apply the non-negativity constraint to a row vector
%usage: rowvecout = cnn(rowvecin)

function out = cnn(v)
v = mkrow(v);
[nr,nc] = size(v);
out = v;
for i = 1:nc
  if v(1,i) < 0.0001
    out(1,i) = 0.00000;
  end
end
return
```

Closer Constraint (Normalize Concentration or Spectra to Approximately 1)

```
%this function will apply the closer constaint to a row vector
%usage: rowvecout = ccr(rowvecin, Formal_concentration)
%
function out = ccr(v,conc)
v = mkrow(v);
[nr,nc] = size(v);
out = v;

scale = sum(v(1,:))/conc;
if (sum(v(1,:)) ~= 1)
  out(1,:) = v(1,:)/scale;
end

return
```

Principal Component Analysis Using Percent Error

```
%This function will produce the percent error for different PC of a
%spectral matrix A using svd
% A(nspec,npts) = scores(nspec,nlv)loadvec(nlv,npts)
% usage:  [stdv] = svdpcastdv(A,nlv)
function [pct] = svdpcapct(A,nlv)
[nspec, npts] = size(A);
[U,S,V] = svd(A);

for a = 1:nlv;
loadvec = V(1:npts,1:a);
s = A*inv(V');
scores = -1*s(1:nspec,1:a);
loadvec = -1*loadvec';
err=(A-(scores*loadvec));
pct(a,1)=1-(sum(sum(abs(err))))/(sum(sum(abs(A))));

end
```

APPENDIX B

(2SAC AND 2SGT SPECTRA)

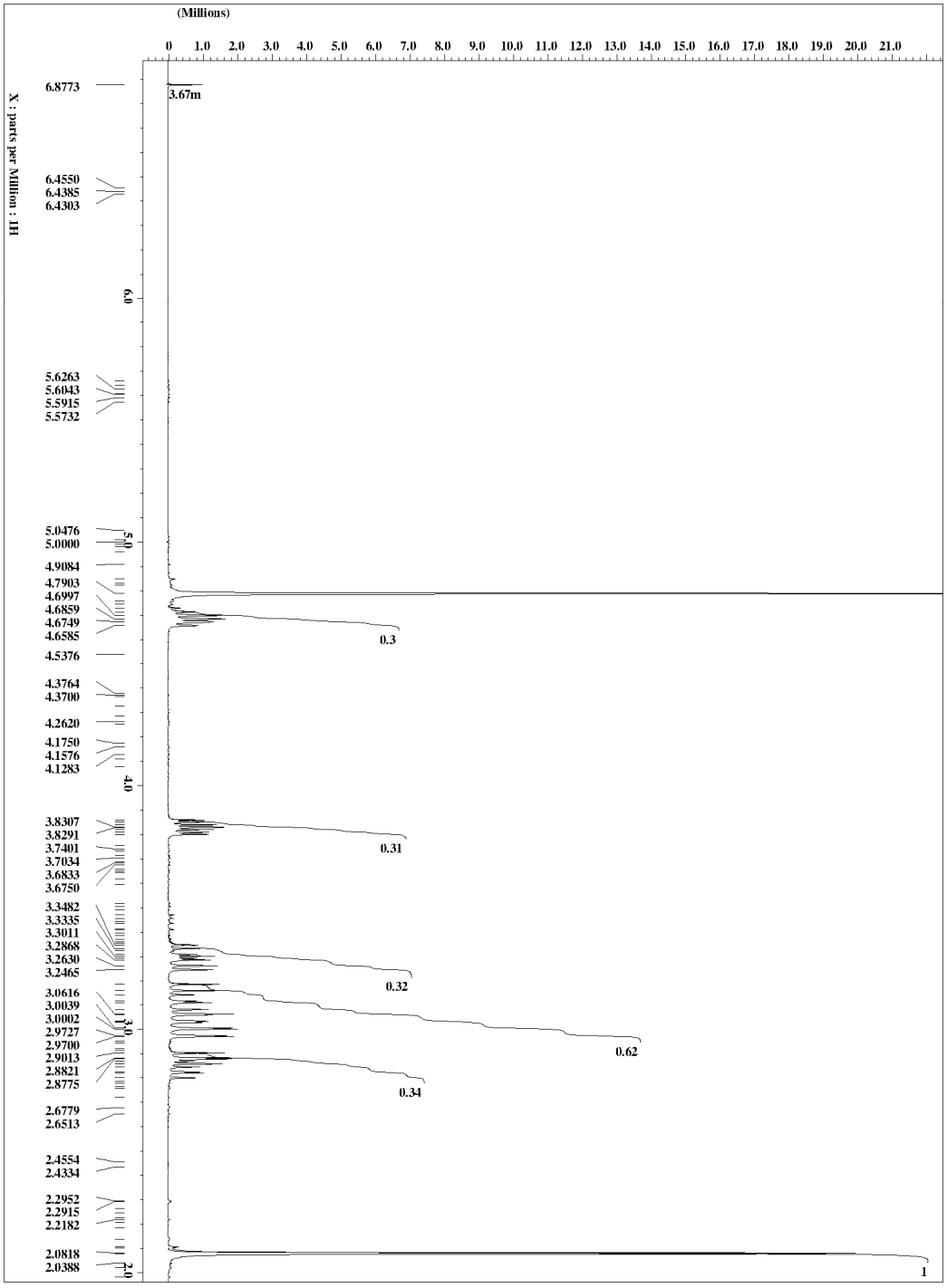

Figure 46: 2SAC ^{1}H NMR Spectrum

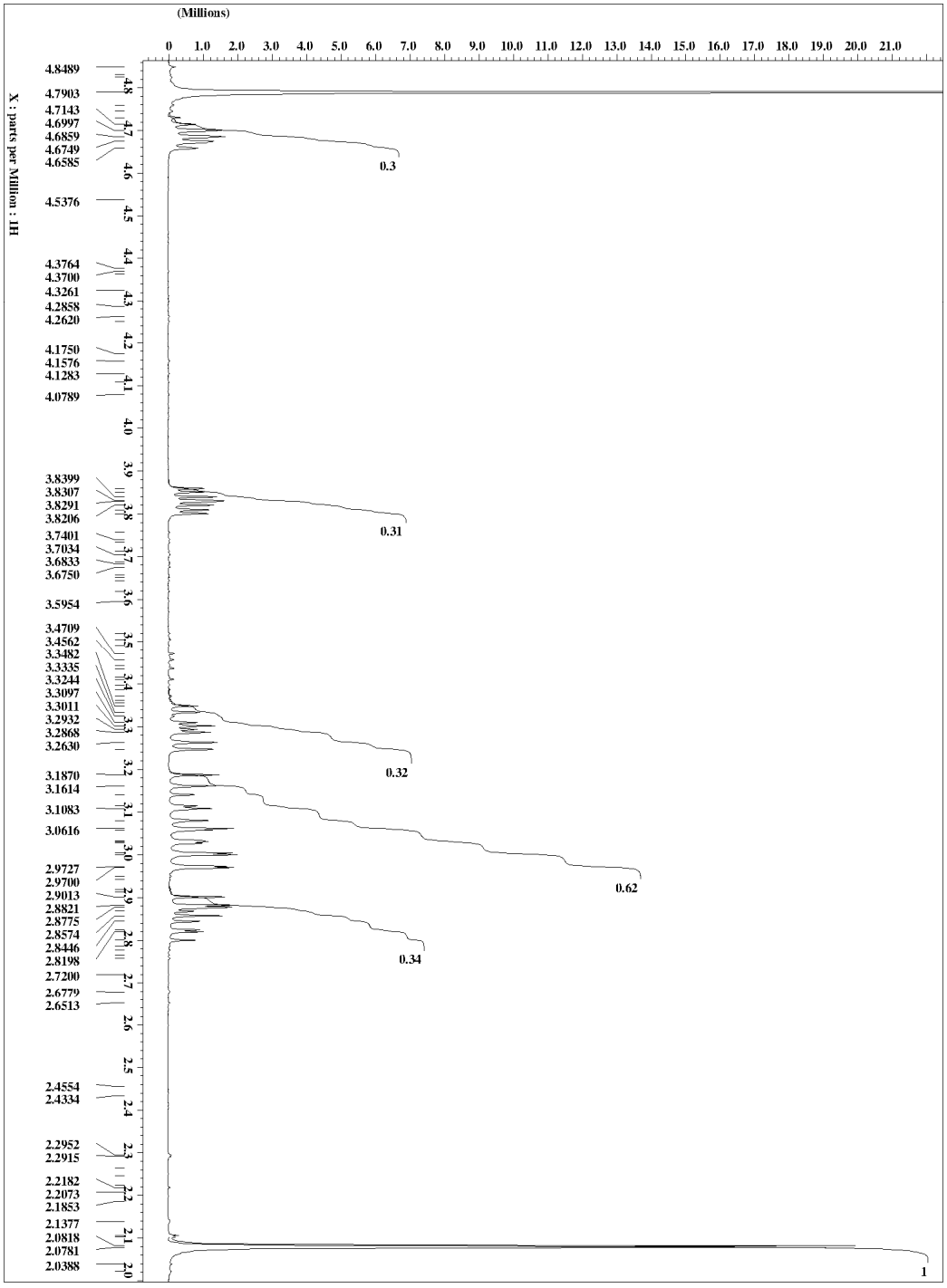

Figure 47: 2SAC ^{1}H NMR Spectrum zoom 1

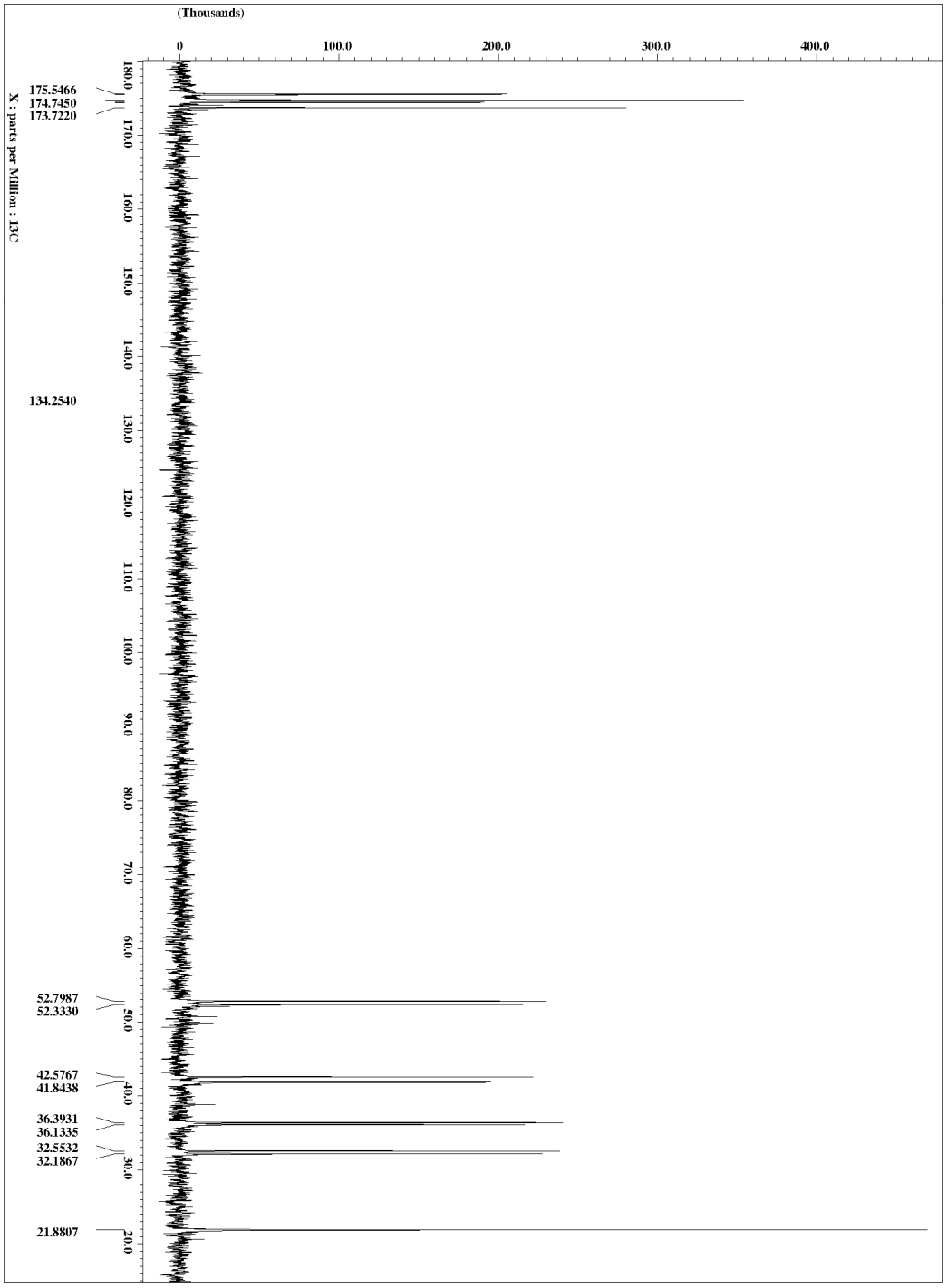

Figure 48: 2SAC ^{13}C NMR Spectrum

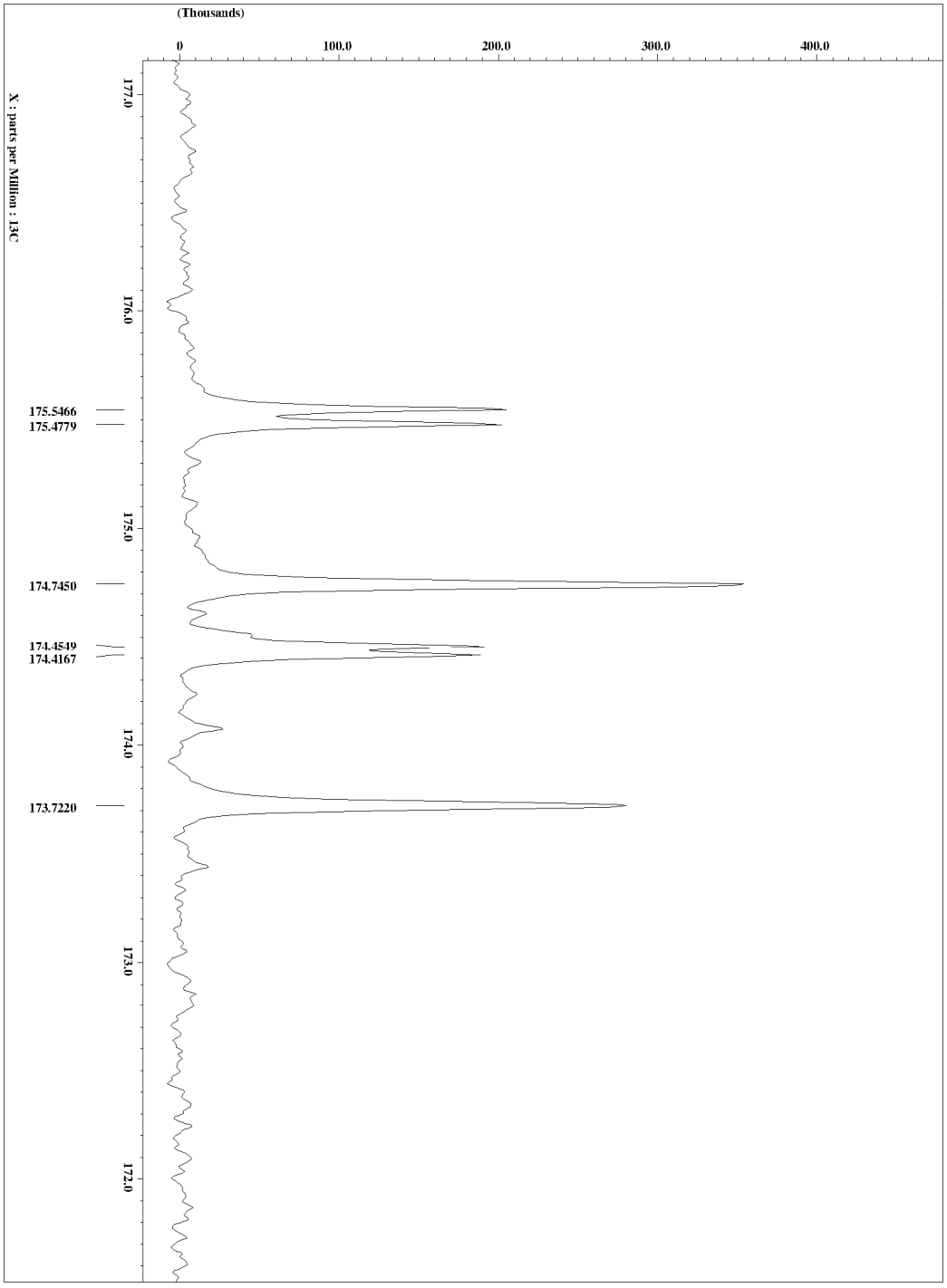

Figure 49: 2SAC ^{13}C NMR Spectrum (zoom 1)

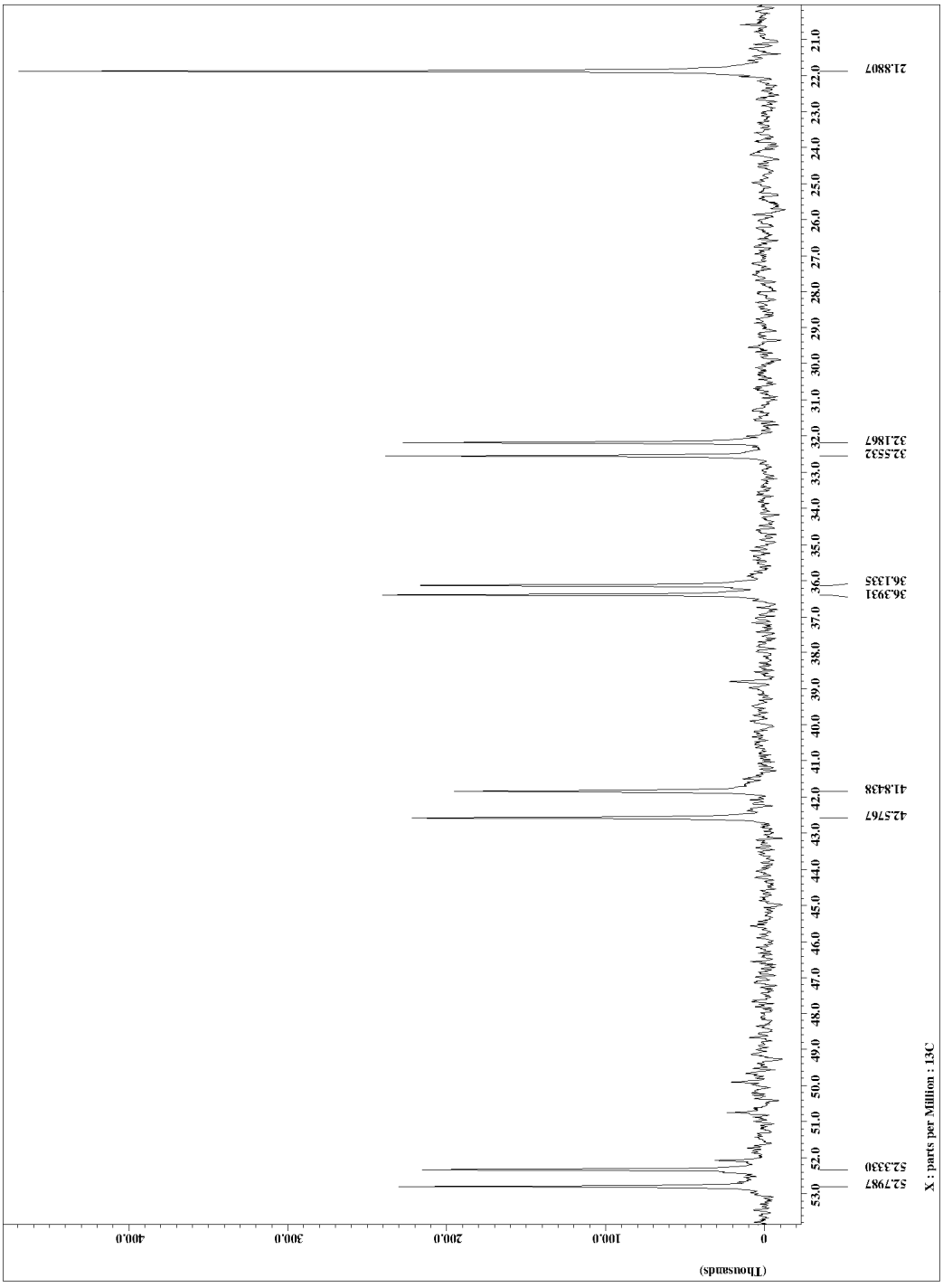

Figure 50: 2SAC ^{13}C NMR Spectrum (zoom 2)

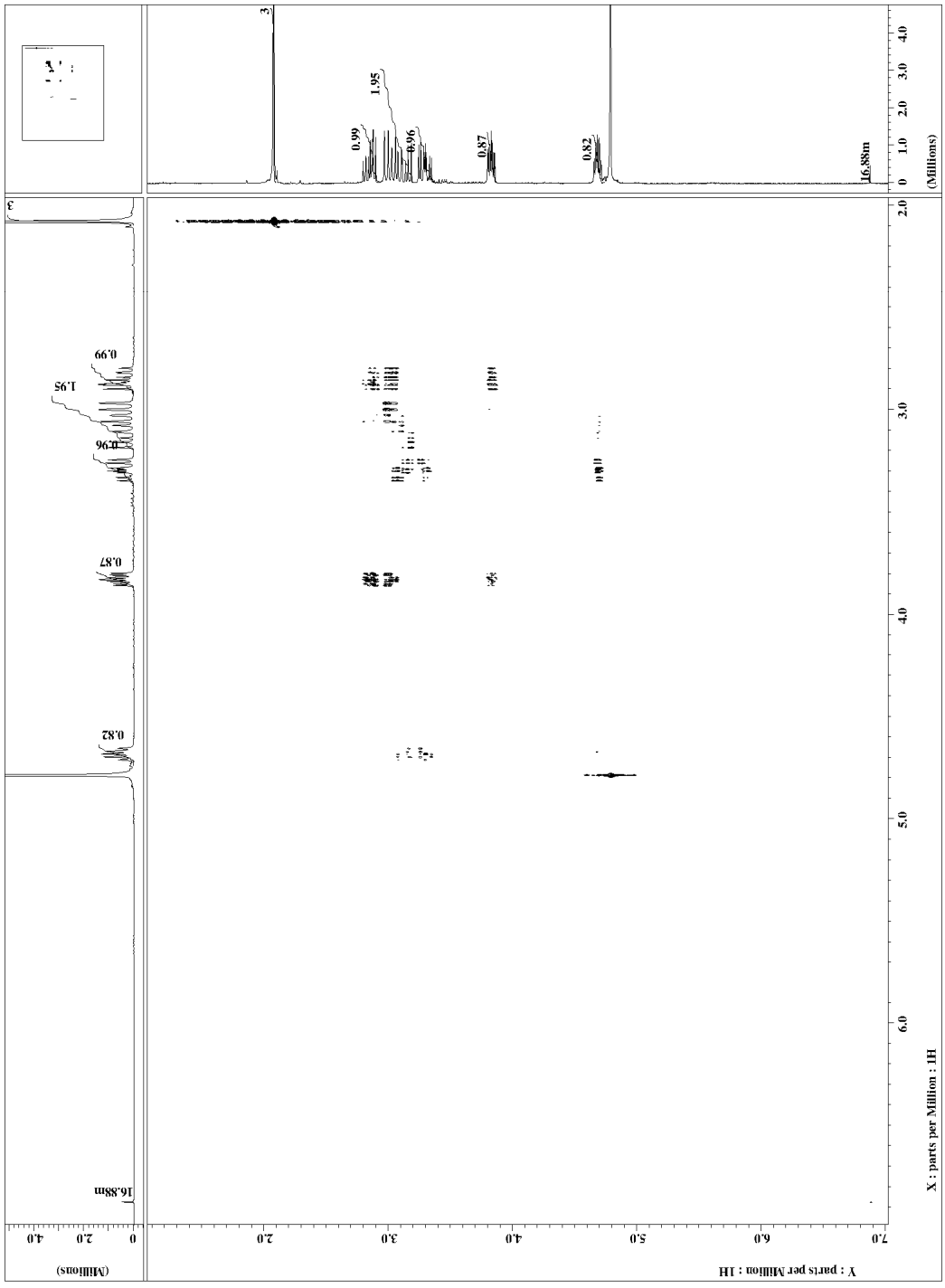

Figure 51: 2SAC COSY Spectrum

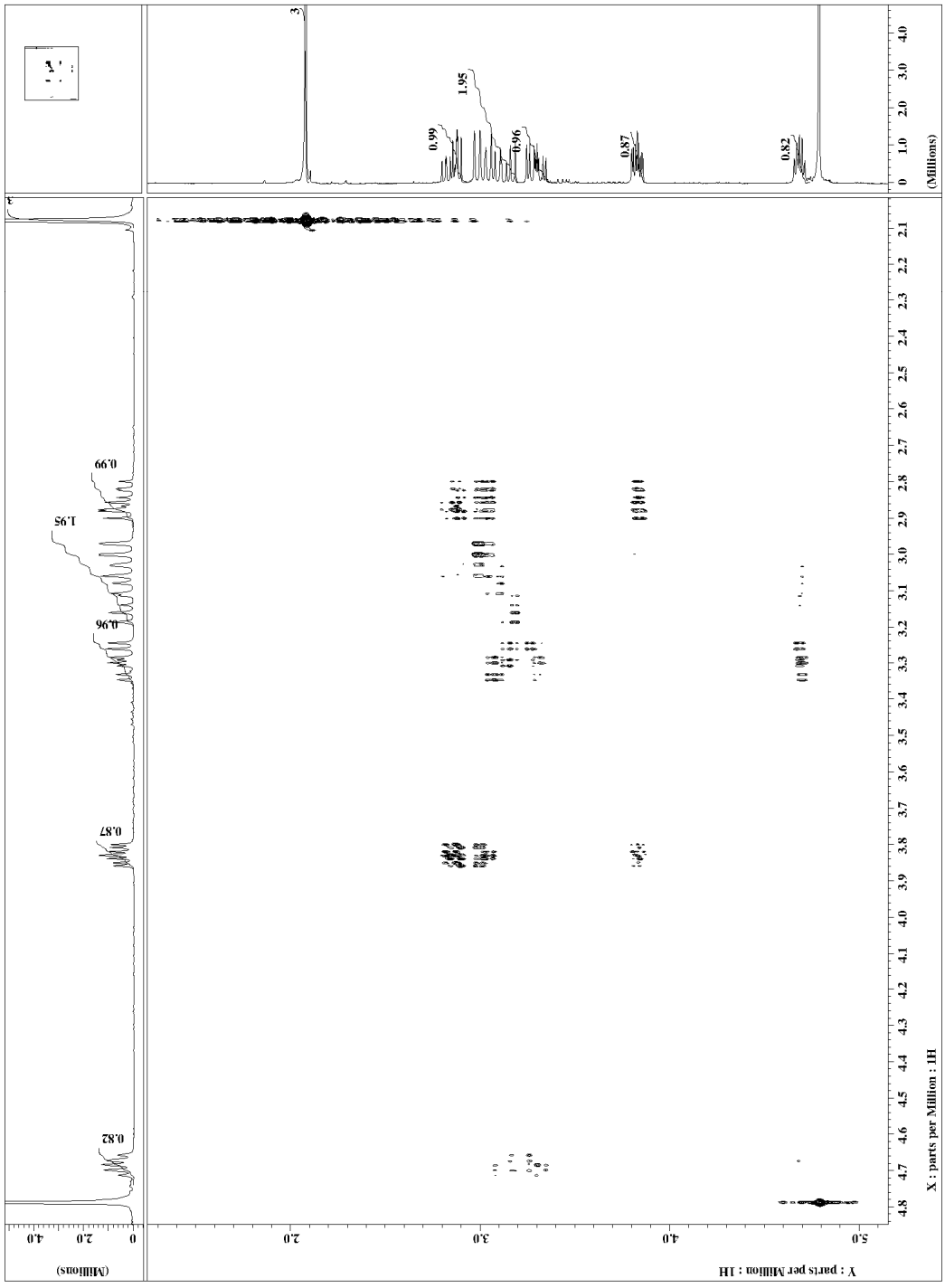

Figure 52: 2SAC COSY Spectrum (Zoom 1)

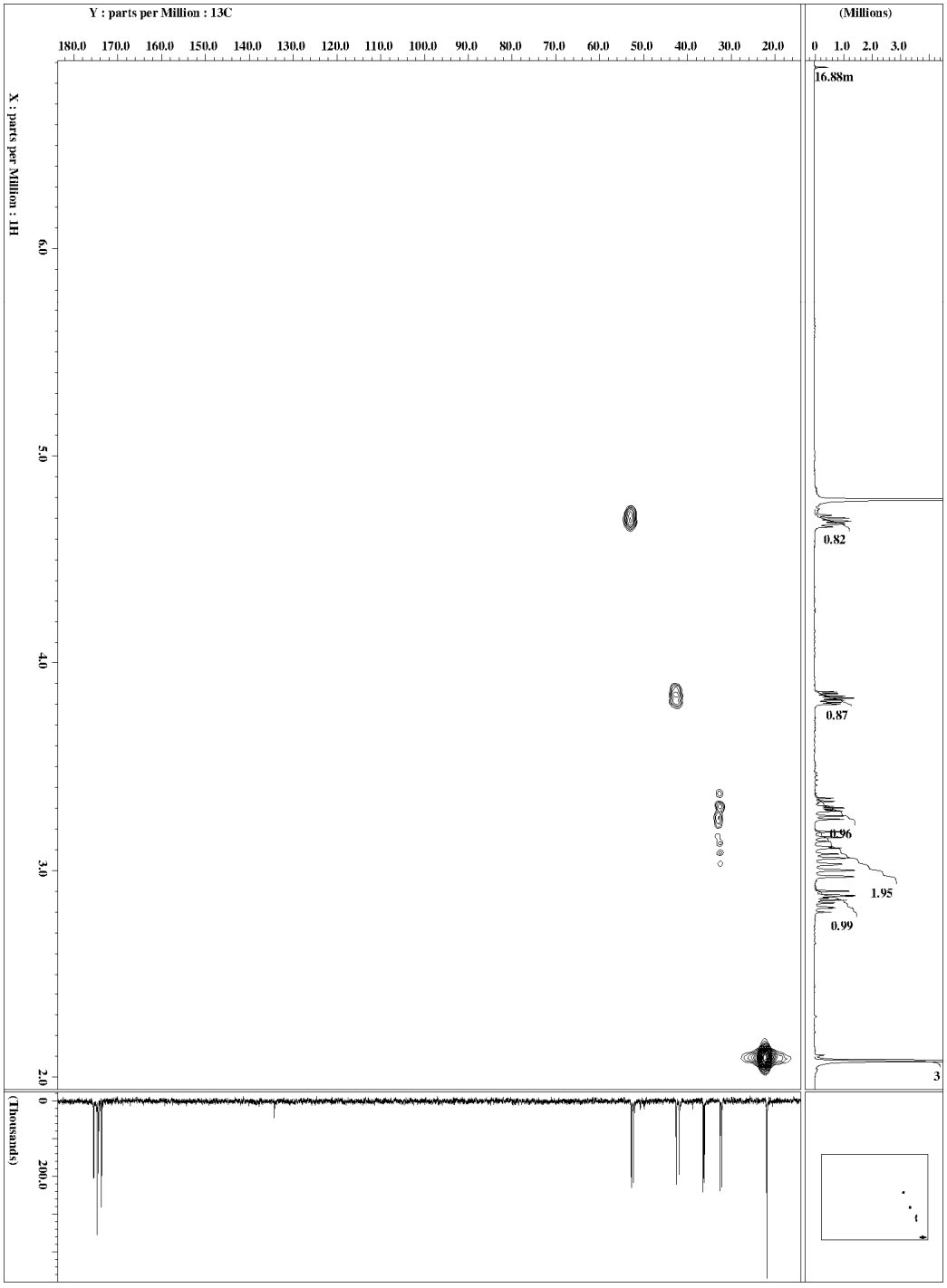

Figure 53: 2SAC HSQC Spectrum

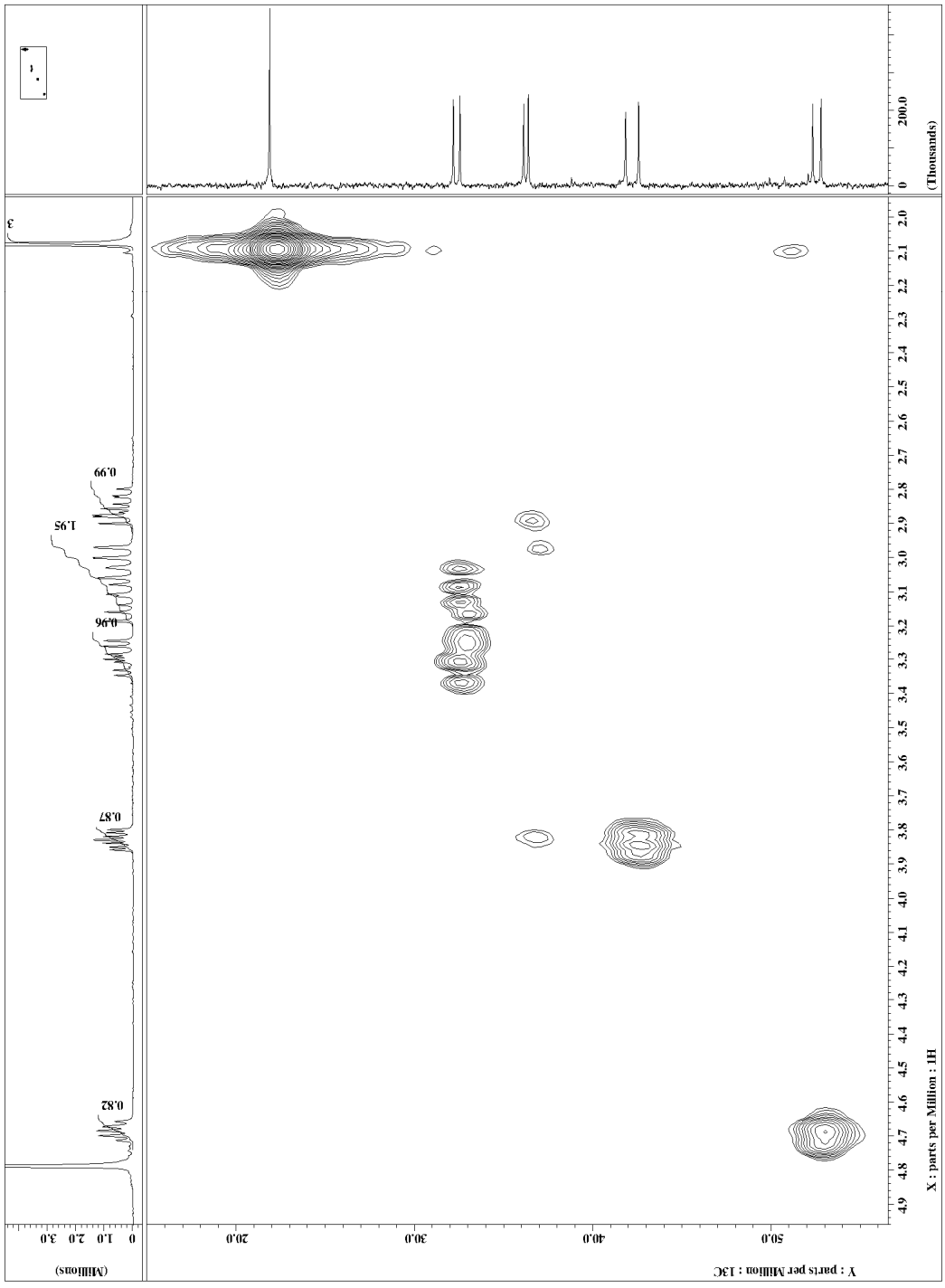

Figure 54: 2SAC HSQC Spectrum (zoom)

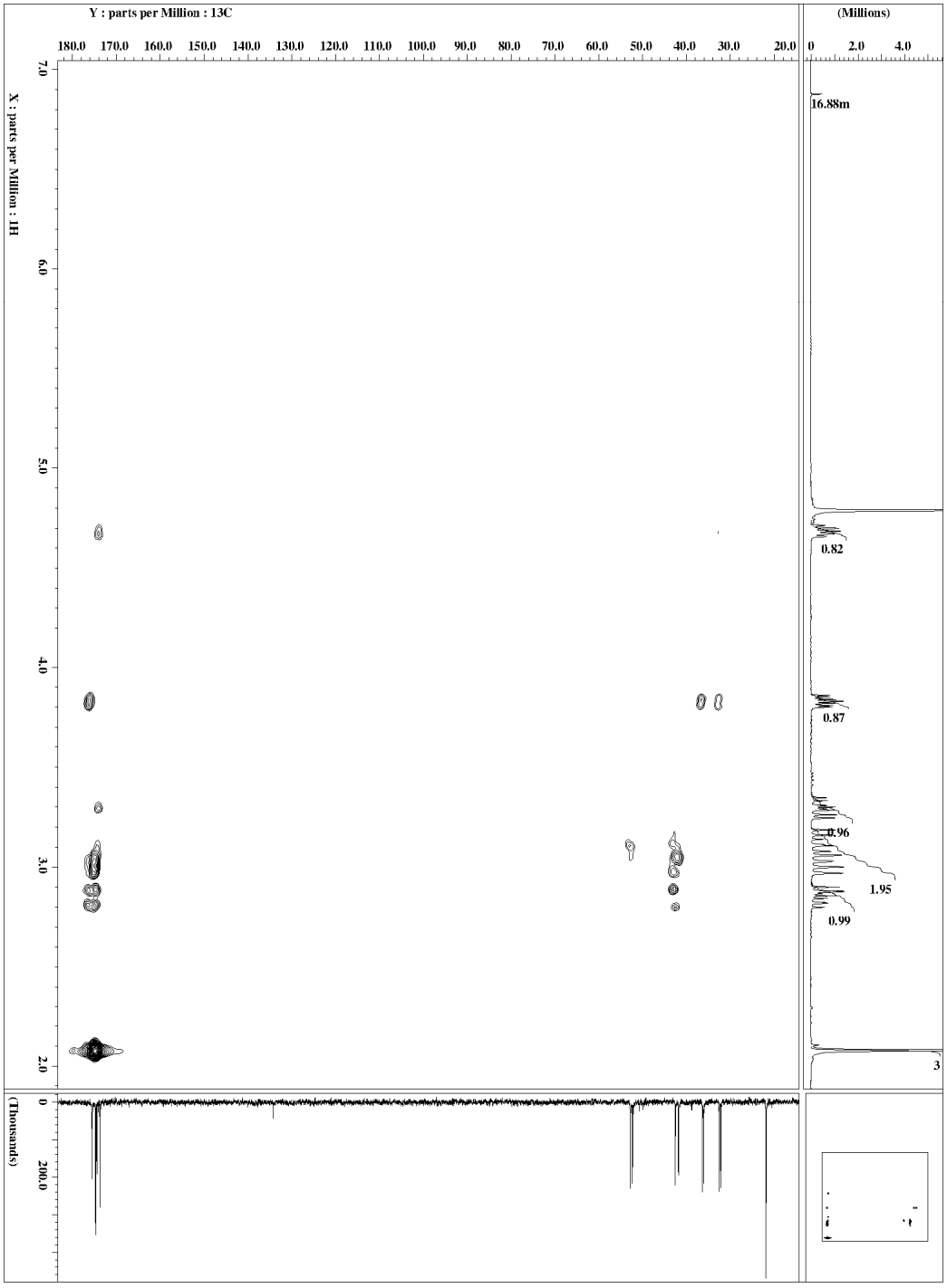

Figure 55: 2SAC HMBC Spectrum

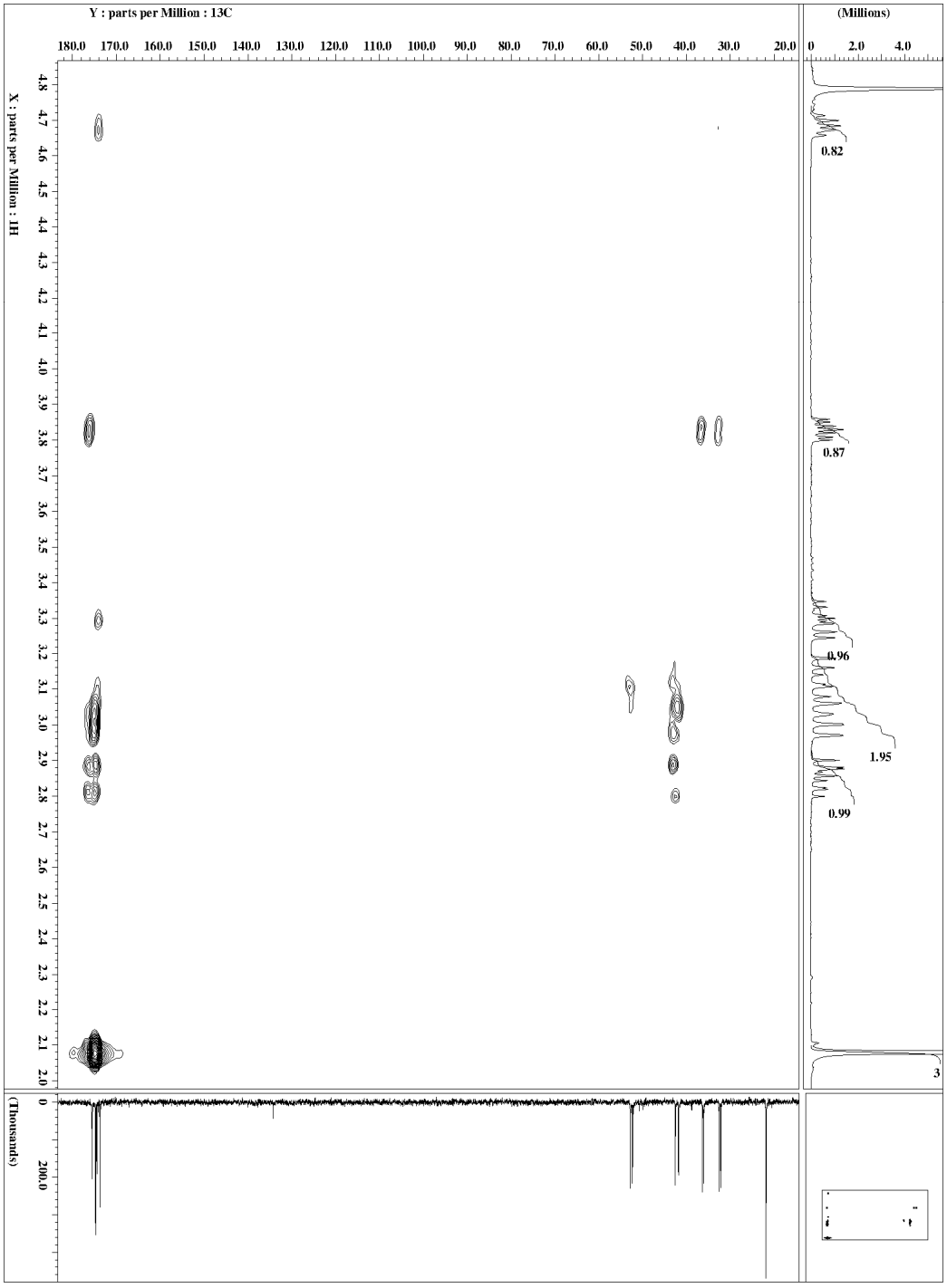

Figure 56: 2SAC HMBC Spectrum (zoom 1)

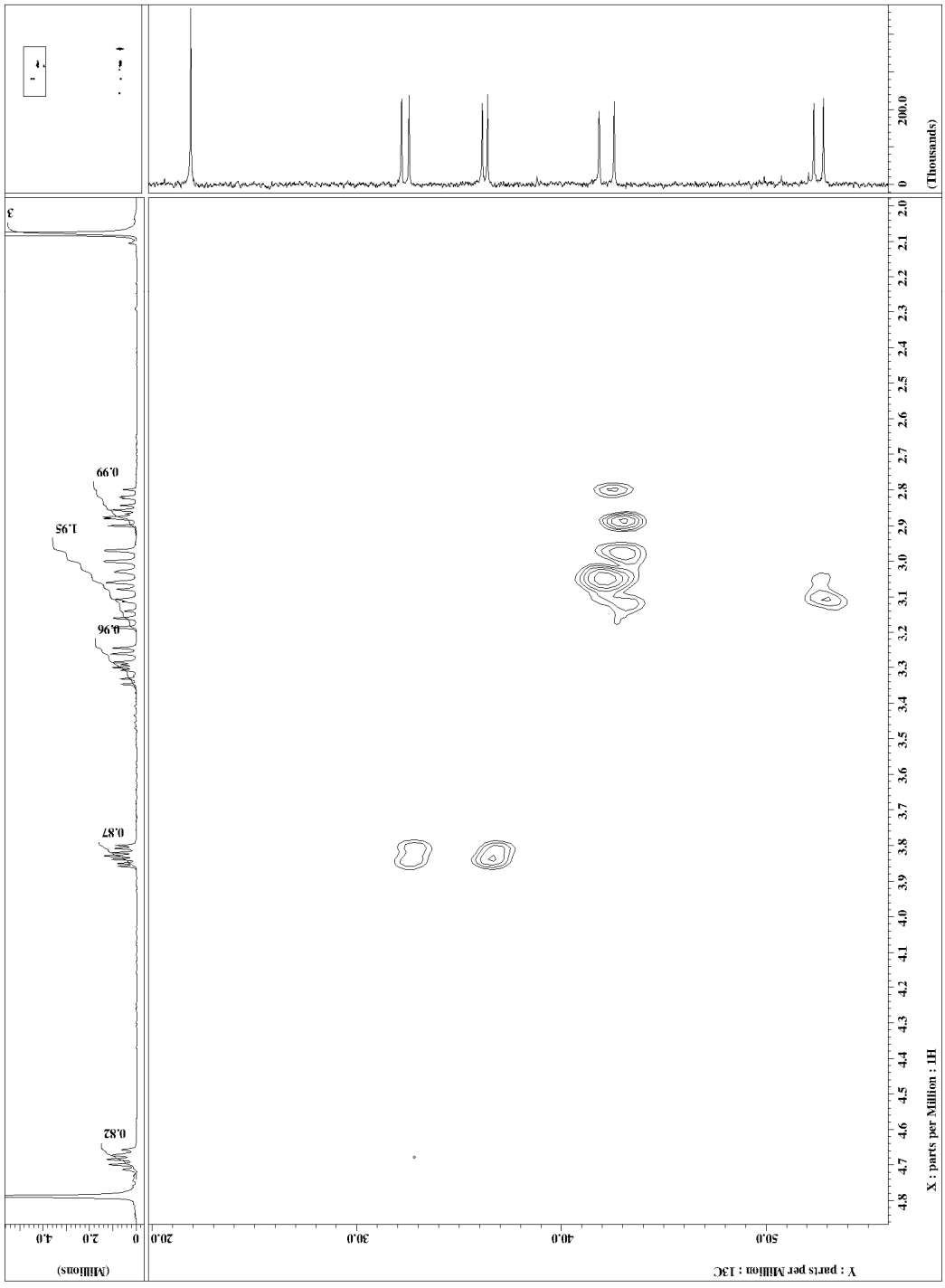

Figure 57: 2SAC HMBC Spectrum (zoom 2)

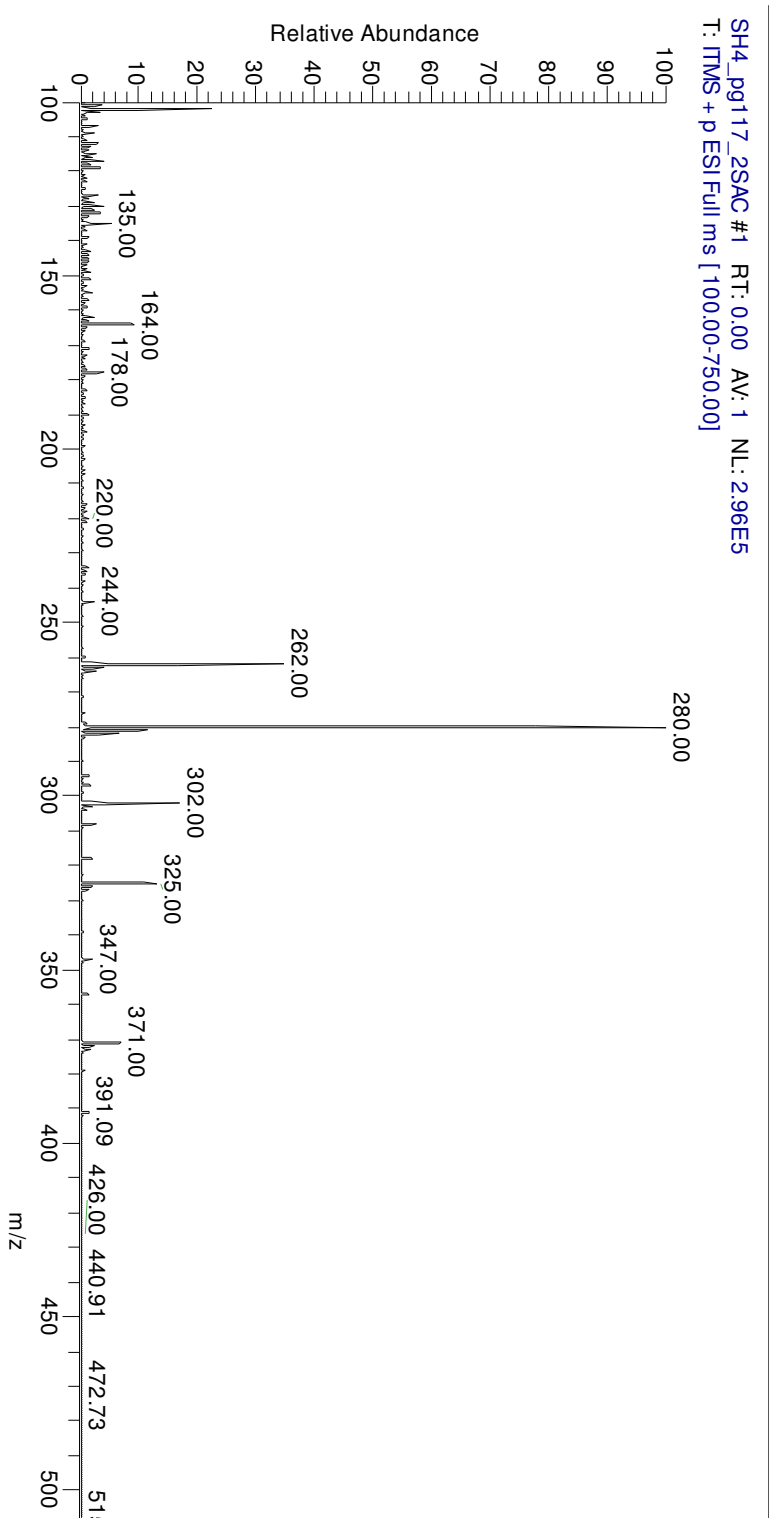

Figure 58: 2SAC ESI Mass Spectrum. Positive ion mode, tuned to m/z = 280, 50 µL/min flow rate

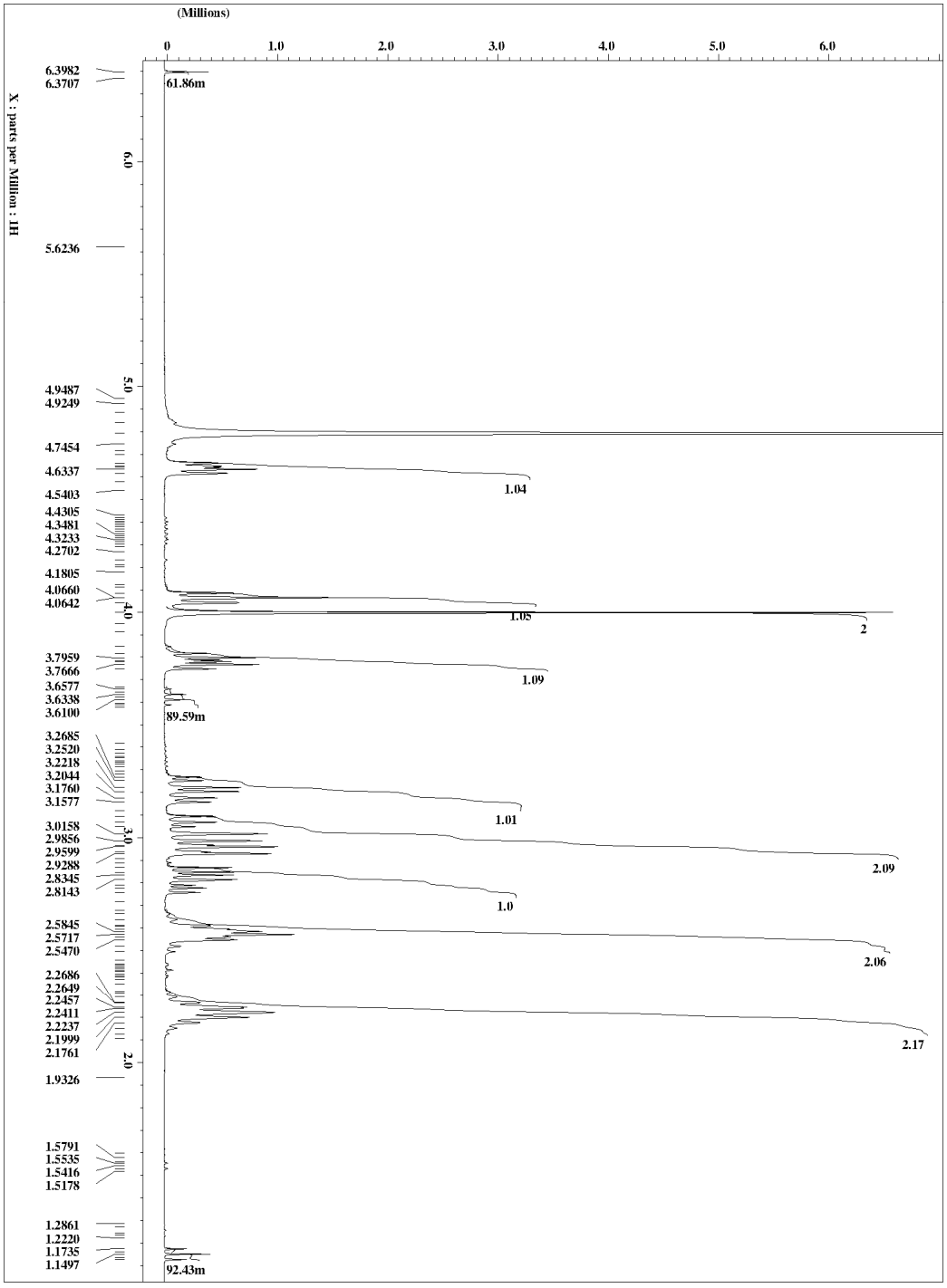

Figure 59: 2SGT ^{1}H NMR Spectrum

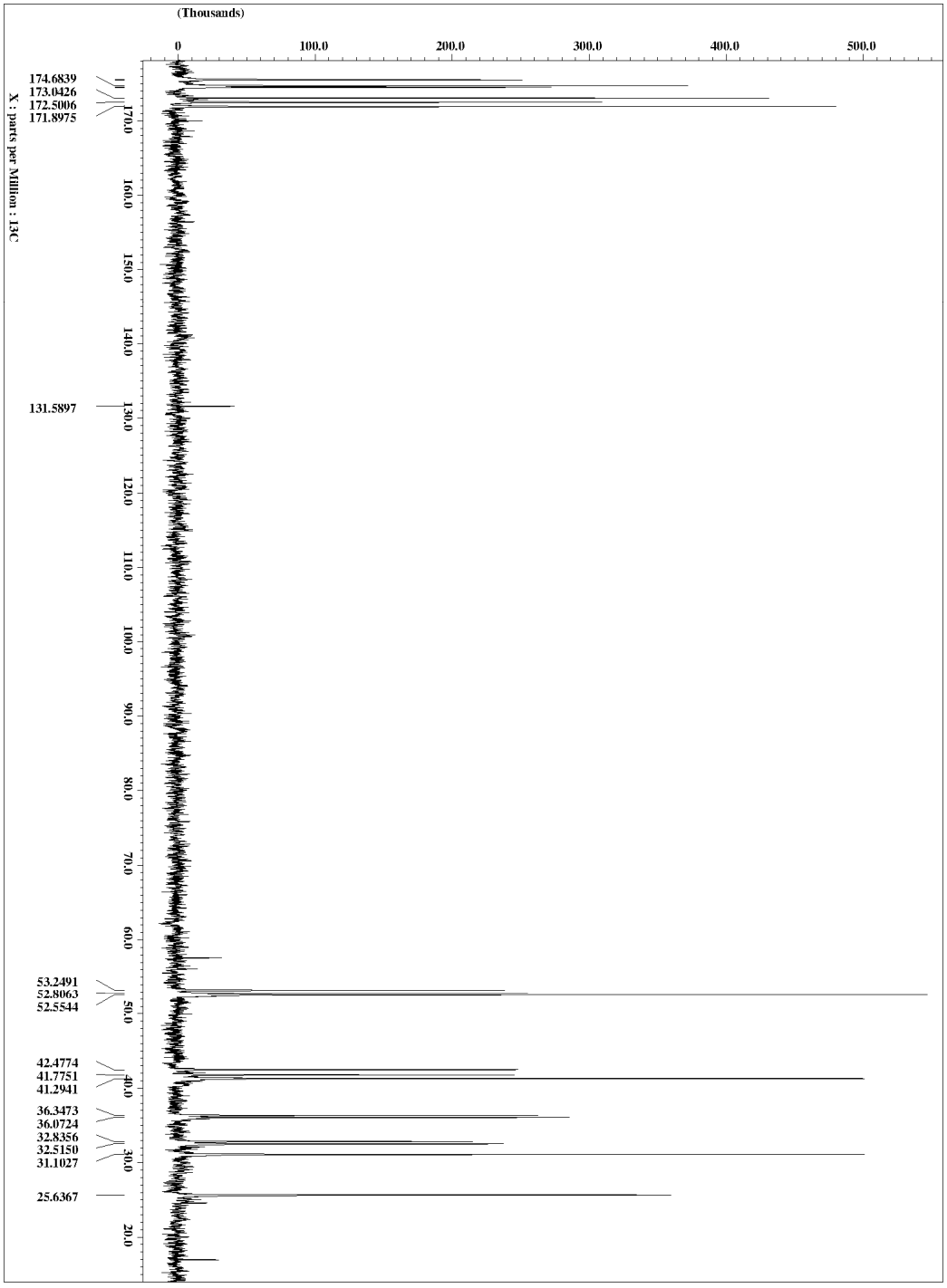

Figure 60: 2SGT ^{13}C Spectrum

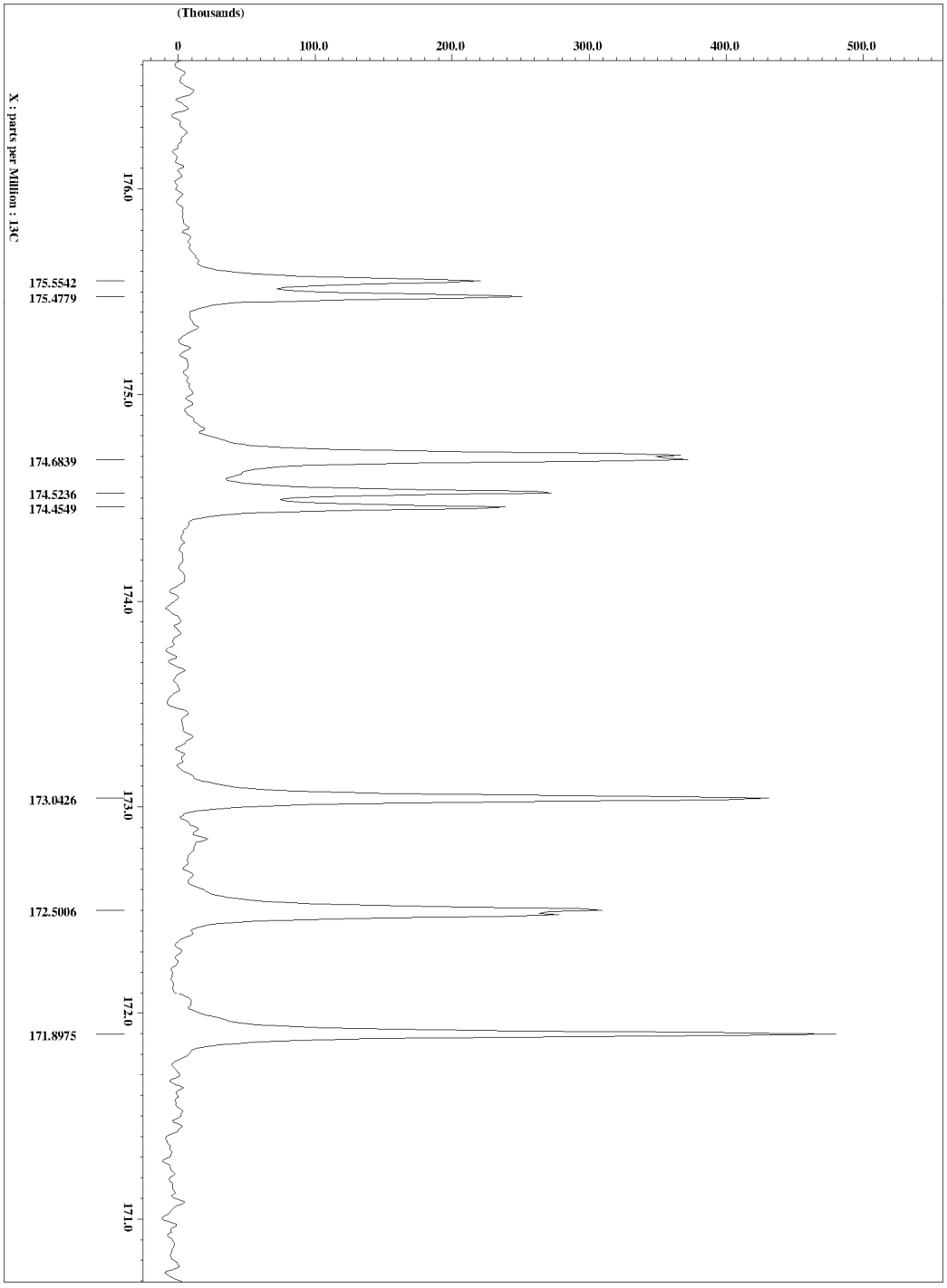

Figure 61: 2SGT ^{13}C Spectrum (Zoom 1)

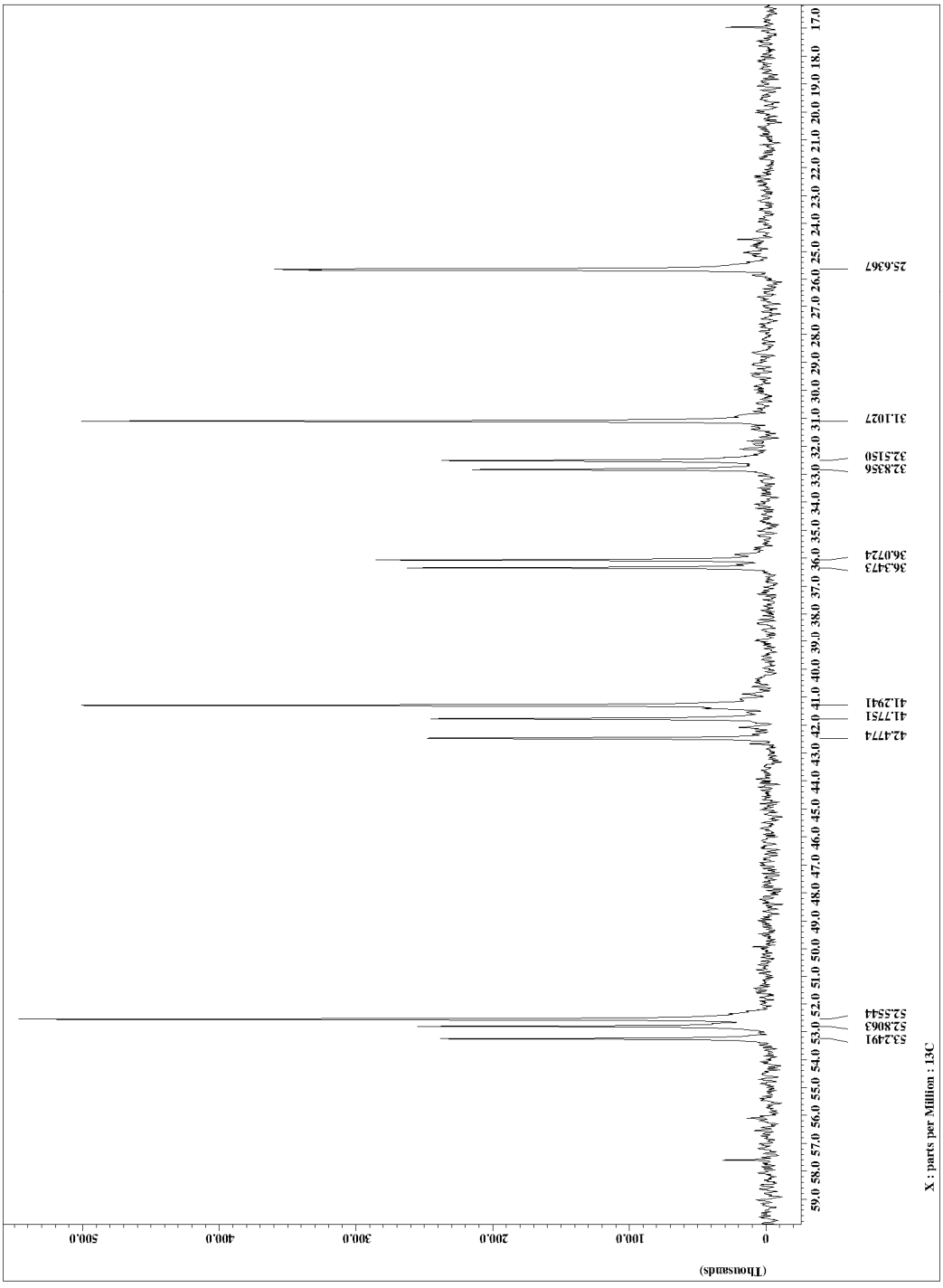

Figure 62: 2SGT ^{13}C Spectrum (Zoom 2)

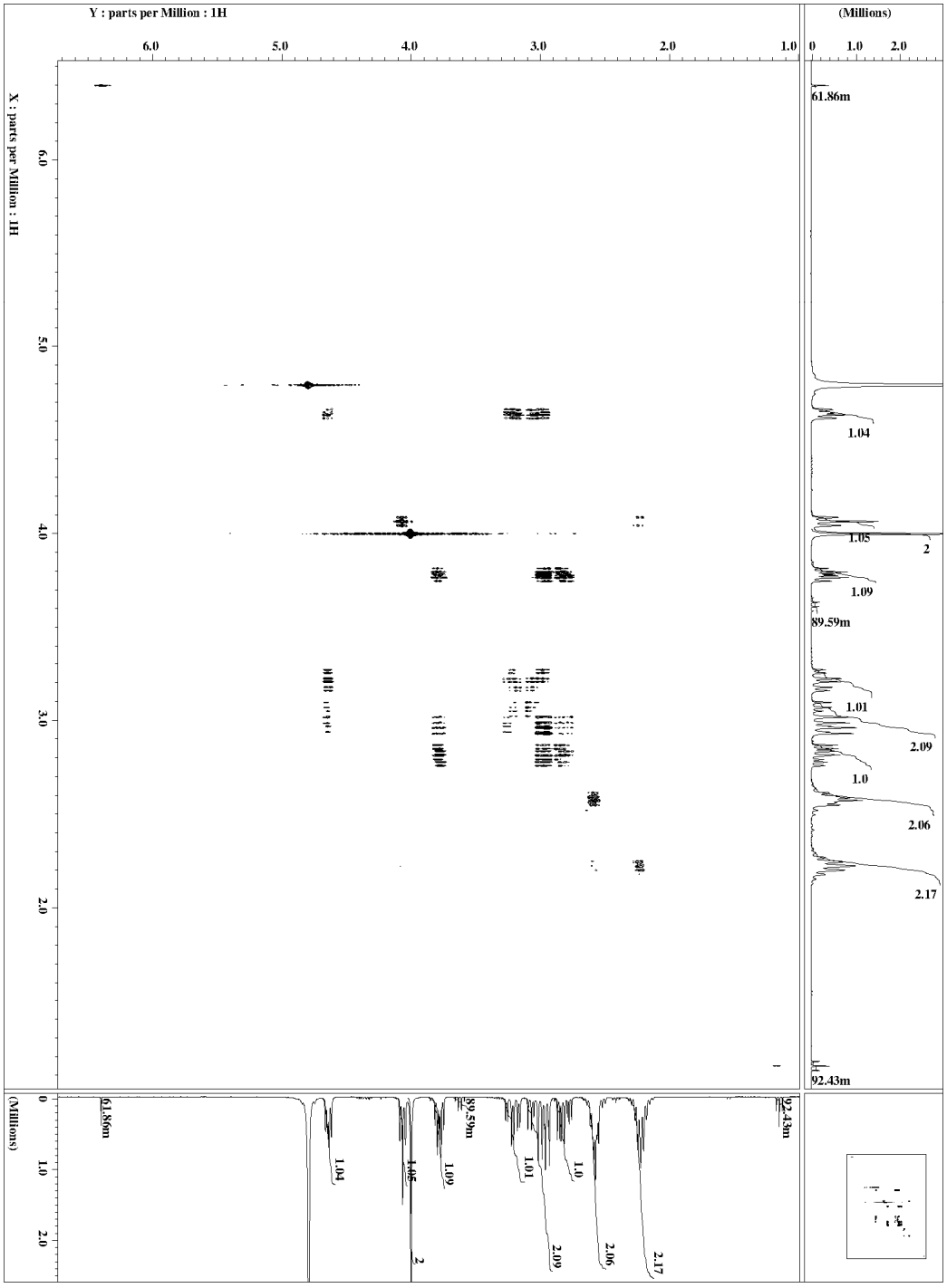

Figure 63: 2SGT COSY Spectrum

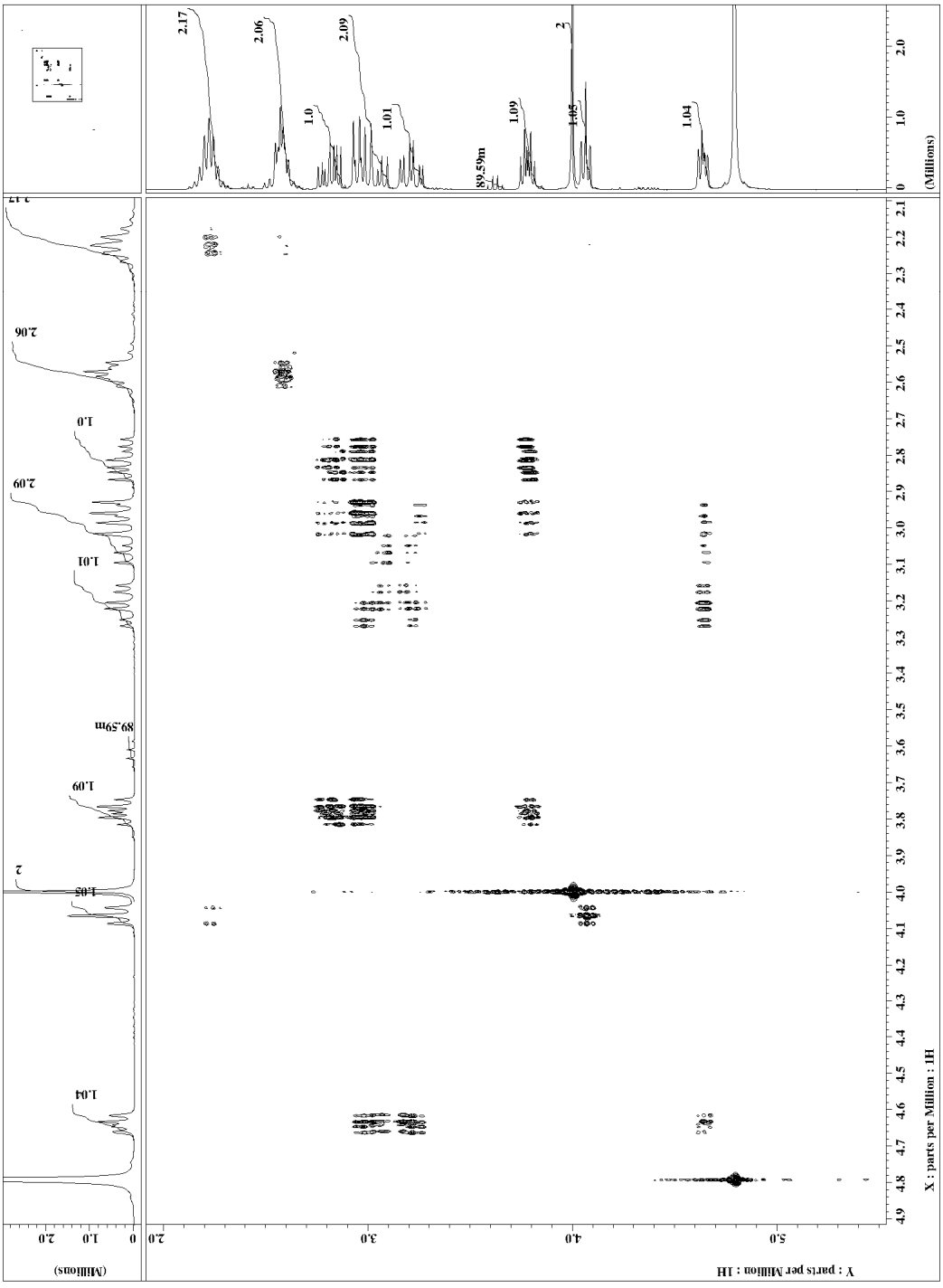

Figure 64: 2SGT COSY Spectrum (Zoom 1)

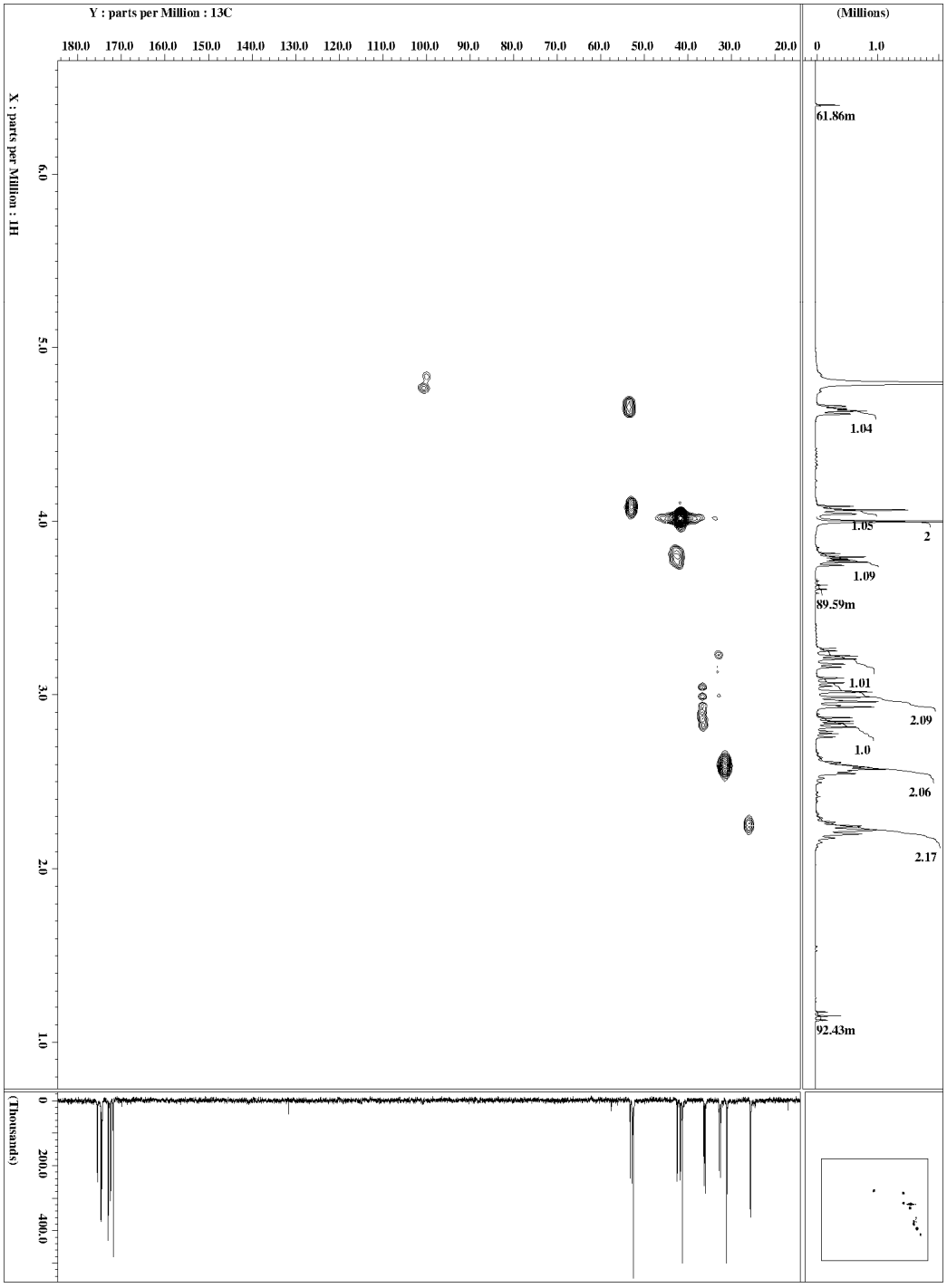

Figure 65: 2SGT HSQC Spectrum

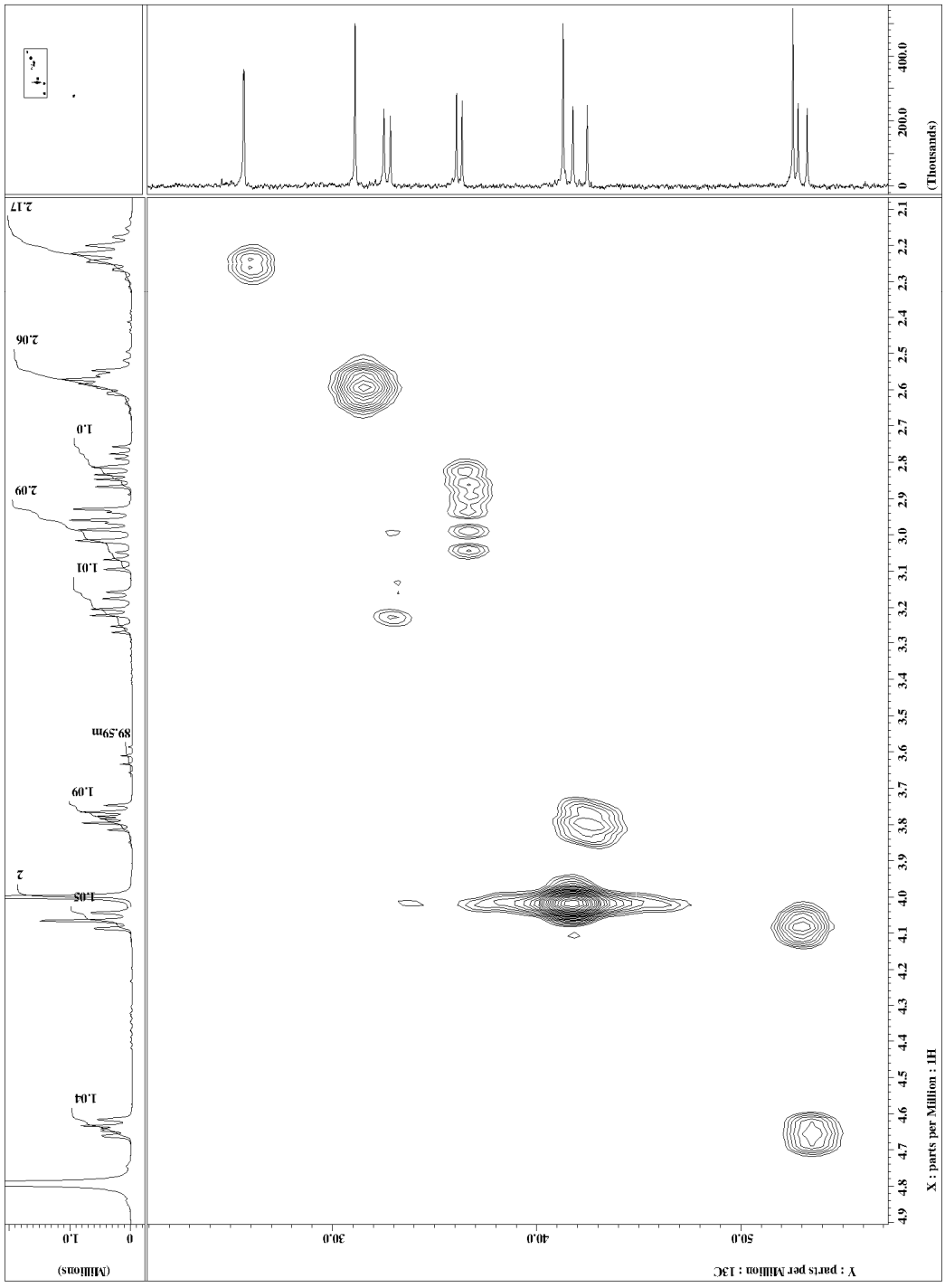

Figure 66: 2SGT HSQC Spectrum (Zoom 1)

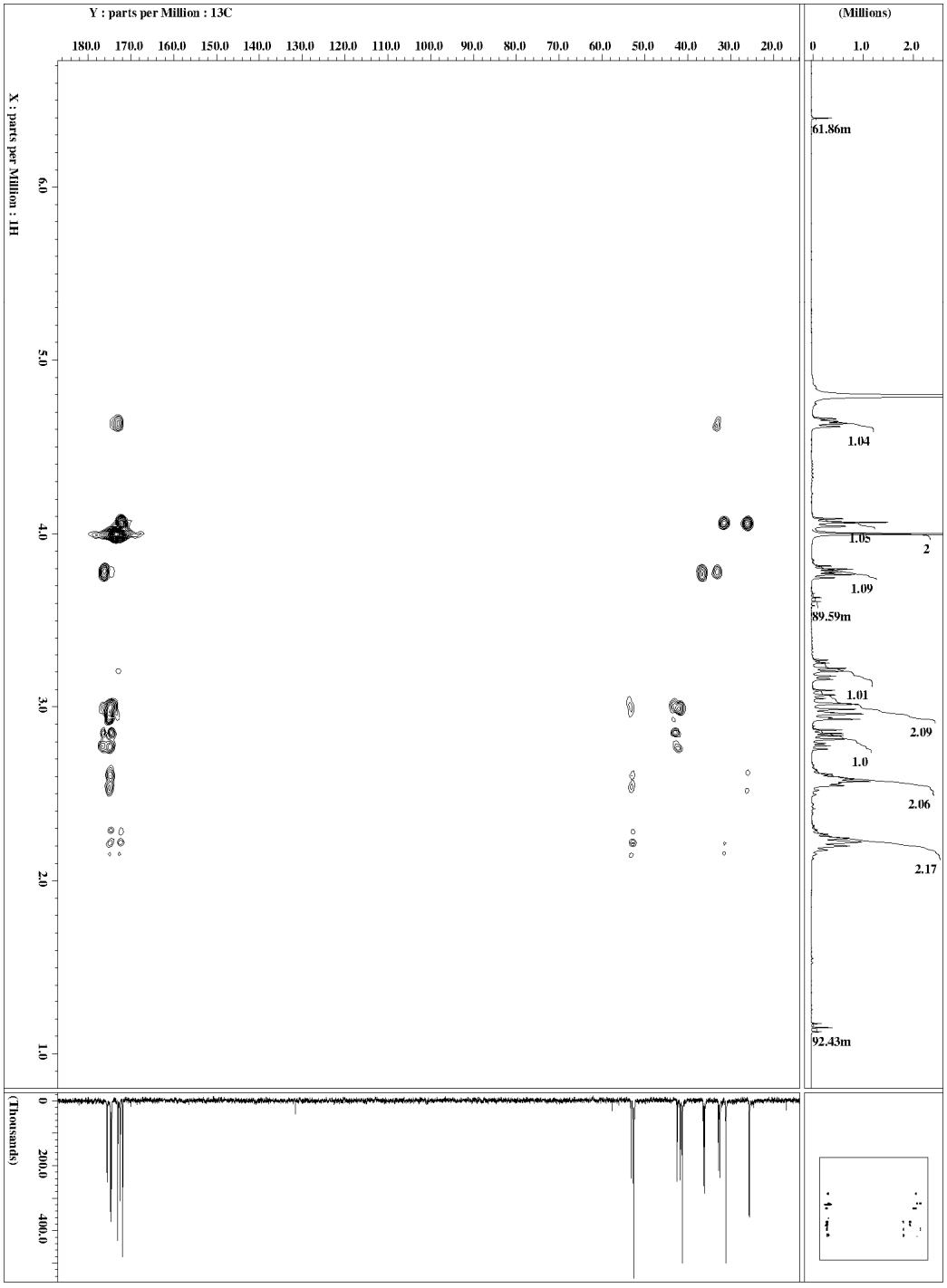

Figure 67: 2SGT HMBC Spectrum

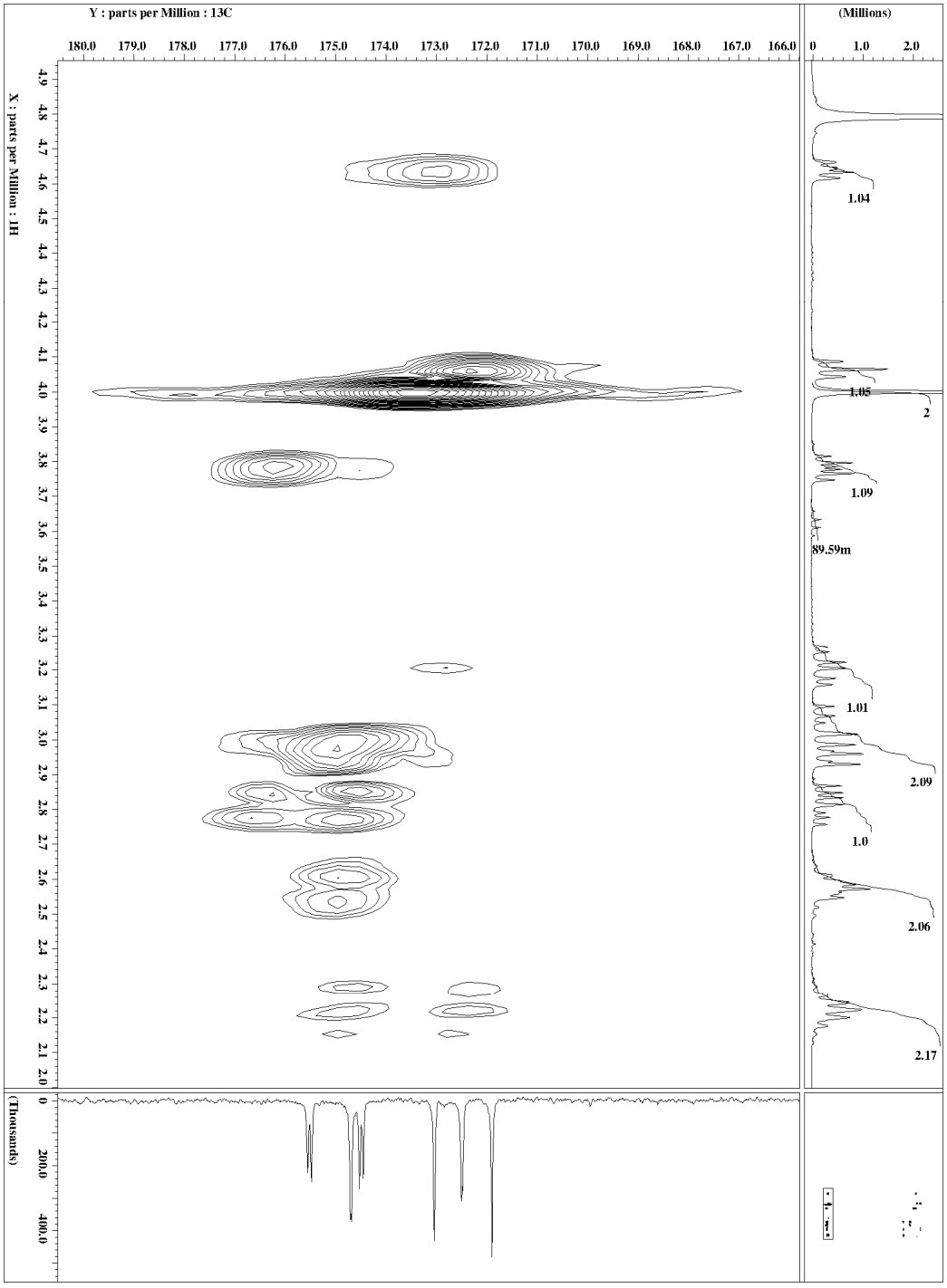

Figure 68: 2SGT HMBC Spectrum (Zoom 1)

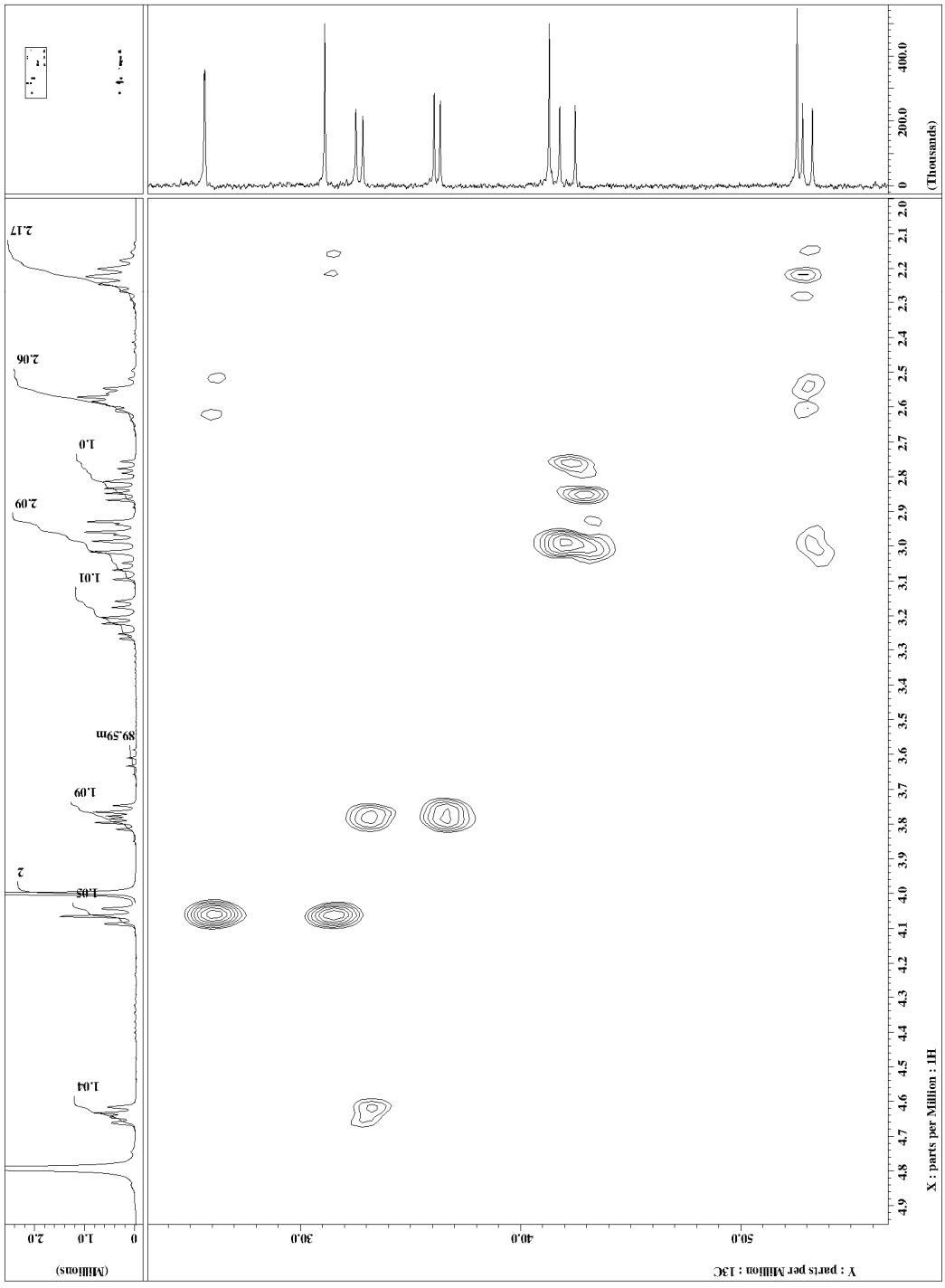

Figure 69: 2SGT HMBC Spectrum (Zoom 2)

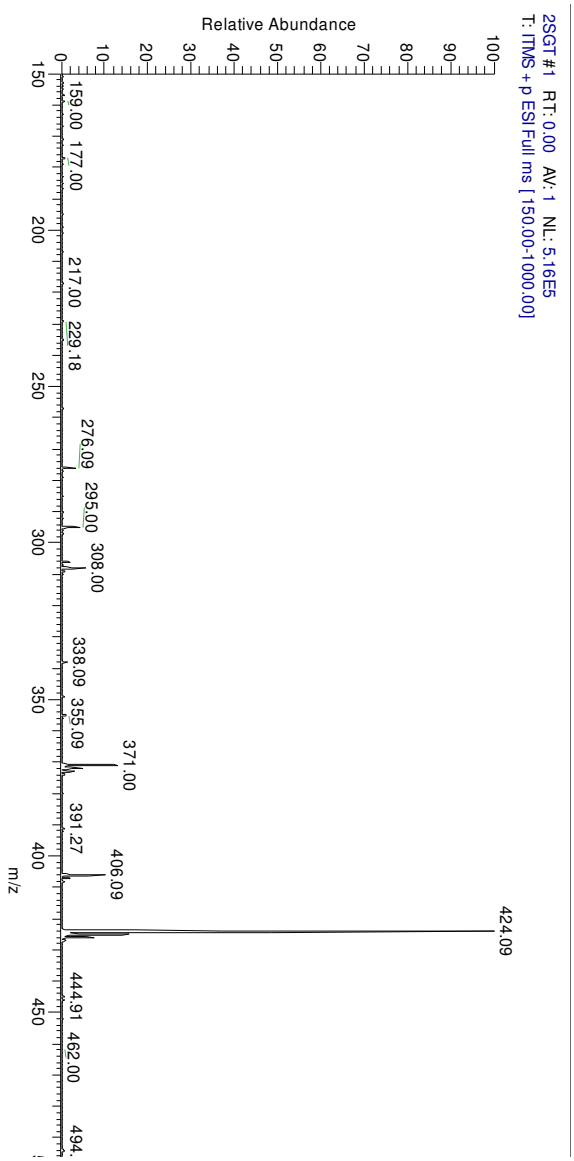

Figure 70: 2SGT ESI Mass Spectrum. Positive ion mode, tuned to m/z = 424, 10 µL/min flow rate

APPENDIX C

(TITRATION SETUP – HARDWARE)

Shown below is a typical setup for titrations. This setup allow for recording of the pH and UV/Vis spectra while titrating in a solution in an anaerobic. The setup includes a three neck flask sealed with rubber septa, a syringe pump for injection of the titrant; a peristaltic pump connected to a flow cell to record UV/Vis spectra, a pH meter sealed with a rubber o-ring and screw cap, and a vacuum hose connected to a Schlenk line to maintain an inert environment (shown below).

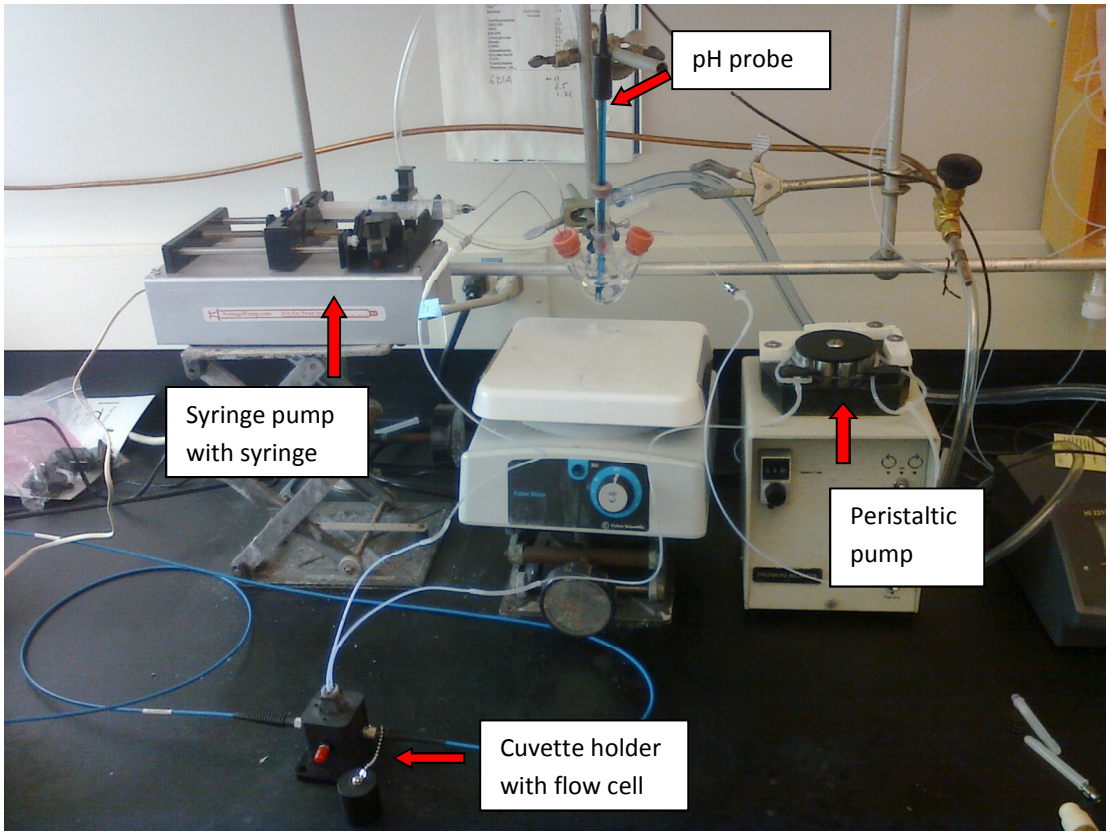

Figure 71: Titration hardware setup.

A closer view of the three neck flask is shown below. Syringe needles are used to inject the titrant from the syringe pump, as well as going to and from the peristaltic pump/flow cell. The

pH electrode is connected to a glass adapter with a rubber o-ring and screw cap. The Schlenk line is also connected to a gas hose fitting on the glass adapter (shown below).

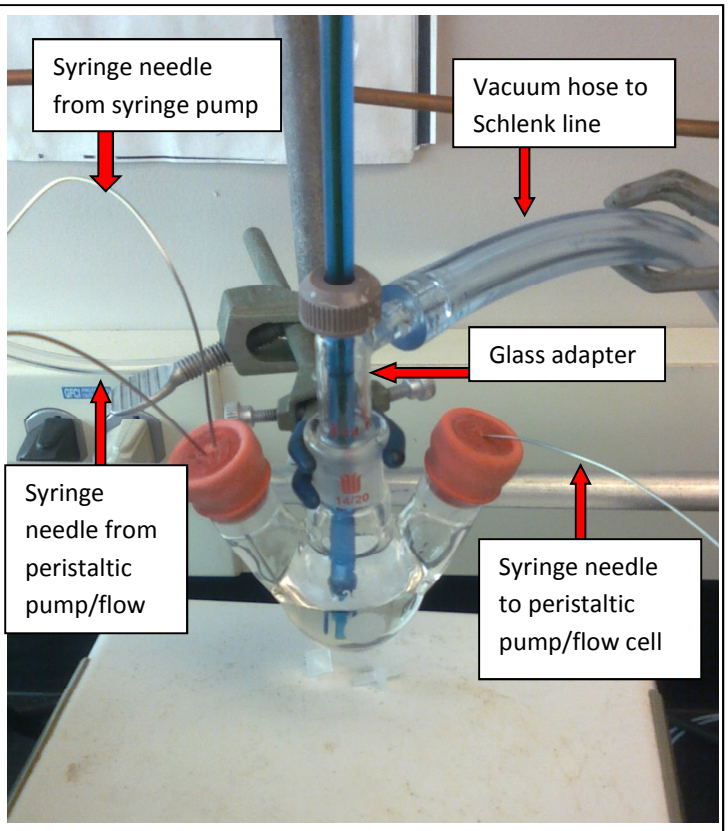

Figure 72: Three neck flask setup for titrations.

APPENDIX D

(TITRATION SOFTWEAR SETUP)

To run a one of the titrations described in this thesis usually three programs were used: SyringePumpPro, HI92000 (pH meter), and BWSpec (UV/Vis spectrometer). This appendix describes the basic use of these programs and how they are coordinated to run a titration.

Syringepumppro

The first program to be described is the SyringPumpPro. This program requires that first a pumping program be created using the supplied Excel template (indicated below with a red arrow).

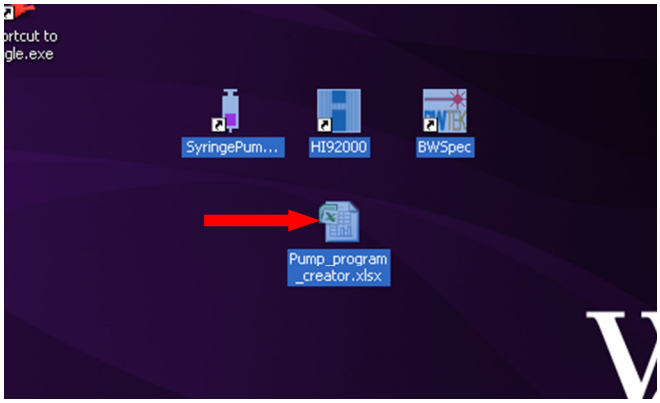

Figure 73: Pump program creator Excel sheet.

Once opened the pump program creator is somewhat self explanatory. The Excel template has two sheets. The first is shown below and is where the details of the pumping program are entered. It should be noted that the maximum time a pause function can last is 99 seconds also the maximum number of loops in one loop function is 99. If more time or loops are need then multiple loops must be set up.

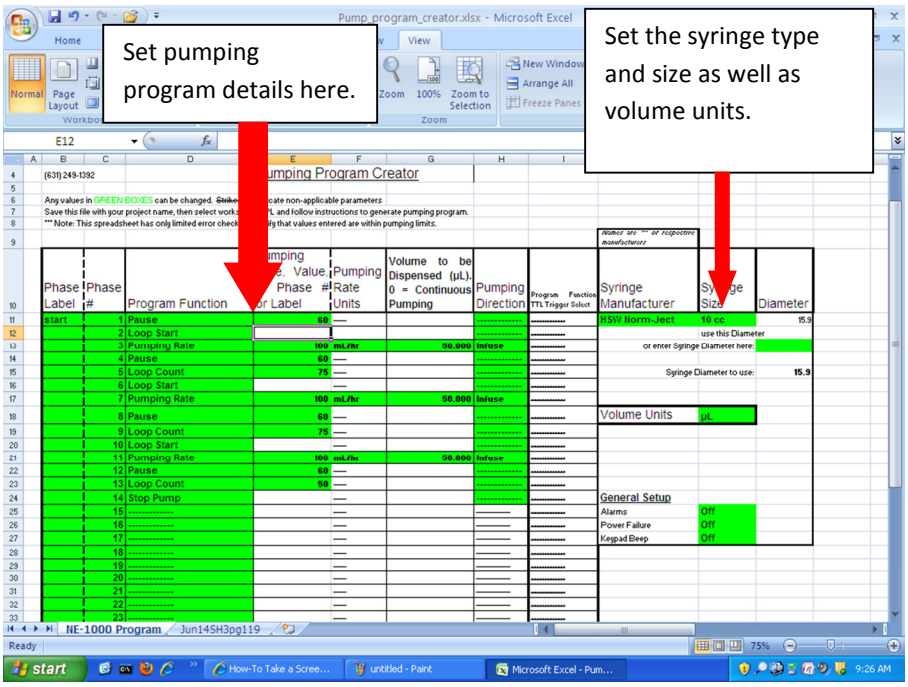

Figure 74: Pump program creator sheet 1.

The details of the pumping program created on sheet one are automatically copied to sheet two (shown below). Instructions on how to save the pump program are given at the top of the second sheet. Each pumping program should be saved as a *.PPL file.

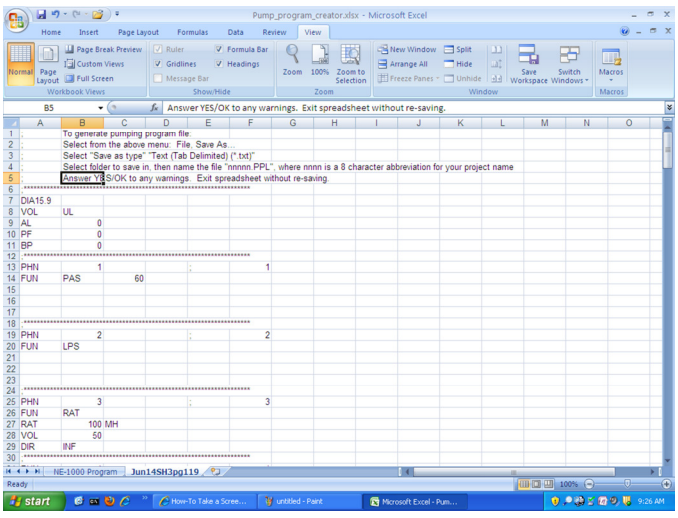

Figure 75: Second sheet of the pump program creator excel template.

Once the pumping program is saved then open the SyringPumpPro program (indicated below by the red arrow).

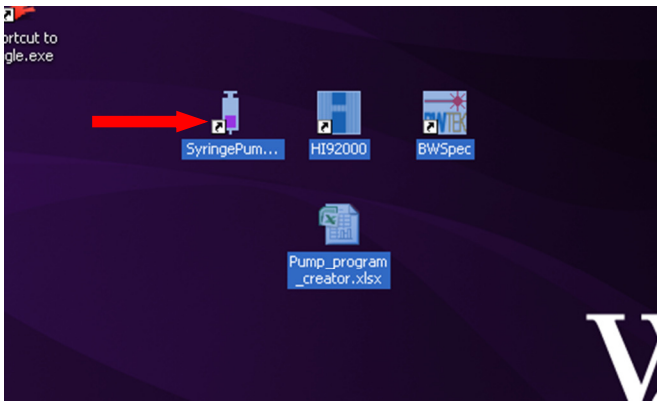

Figure 76: Pump program creator Excel sheet.

Once open the SyringPumpPro program should look like the screen shot shown below. At the top of the screen the program should say “2 pumps licensed” and “Pump 00” should be displayed in the white box on the top half of the screen.

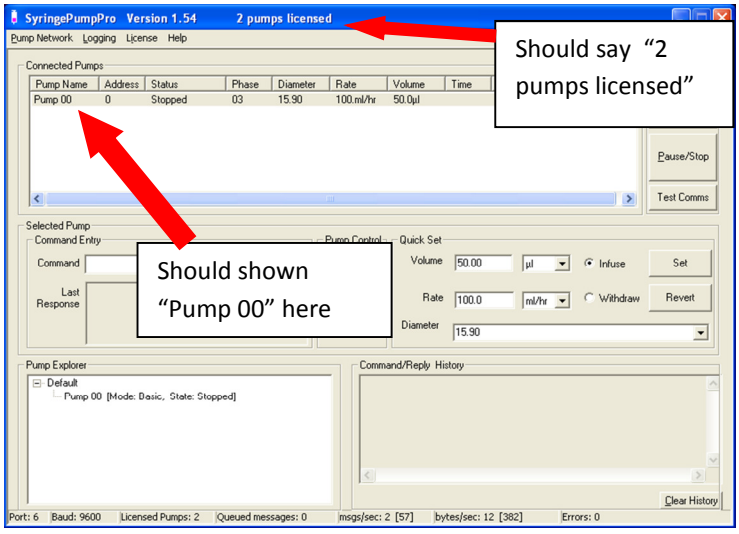

Figure 77: SyringPumpProg program.

If the “2 pumps licensed” is not displayed then you probably need to log off and have an administrator log on (Dr. Summers). If no pump is displayed in the white box in the top half of

the screen then go to the Pump Network tab and click on the Auto Detect Pump Network (red arrow below). It should take about 5 seconds before it finds the pump

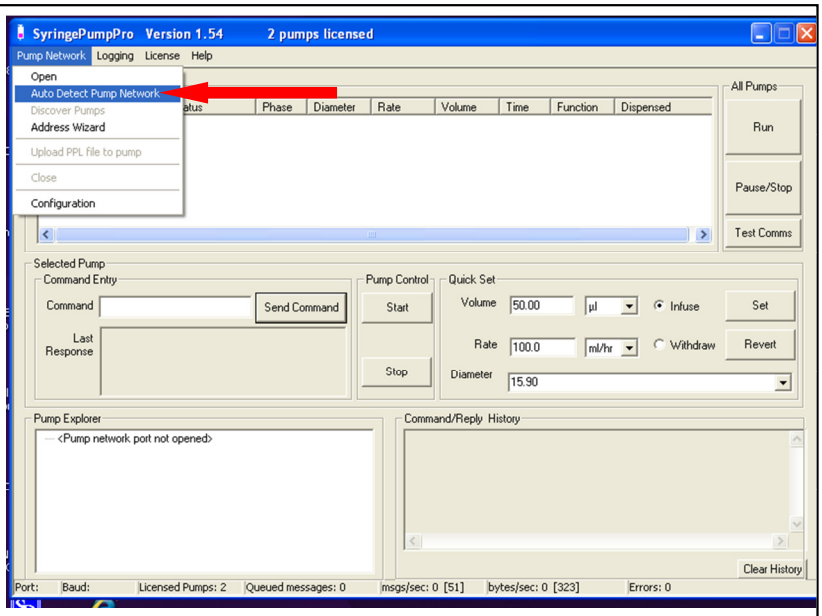

Figure 78: Select "Auto Detect Pump Network" if now pumps are shown.

Once the pump is ready to go, right click on Pump 00 in the white box in the top half of the screen. In the pop up text box, click on the Program/PPL File (as show below) to upload the pump program.

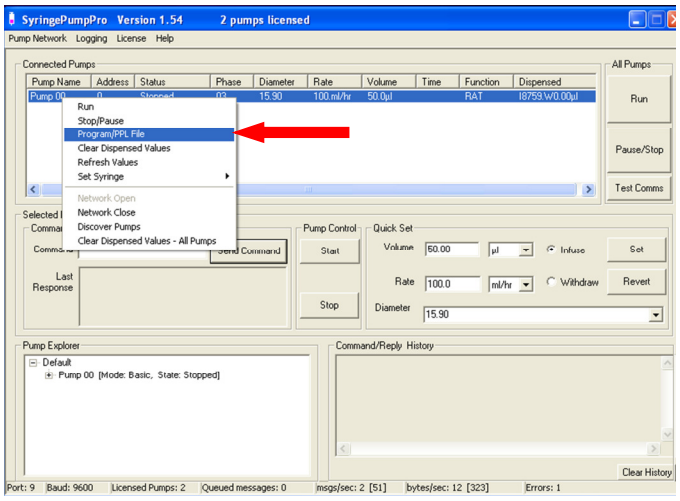

Figure 79: Select "Program/PPL File" to upload a pump program.

Once the pumping program is uploaded you can simply run the program by clicking "Run" on the right hand side of the screen. However if you want to record the pH and/or UV/Vis spectra you should wait to coordinate the timing of each program.

HI92000 (pH Meter)

To set up the pH meter to record the pH over the course of a titration fist click on the HI9200 icon (red arrow in panel A in the figure below). There will be a pop up window as shown in panel B in the figure to the below. Click on the "Real Time Logging" option.

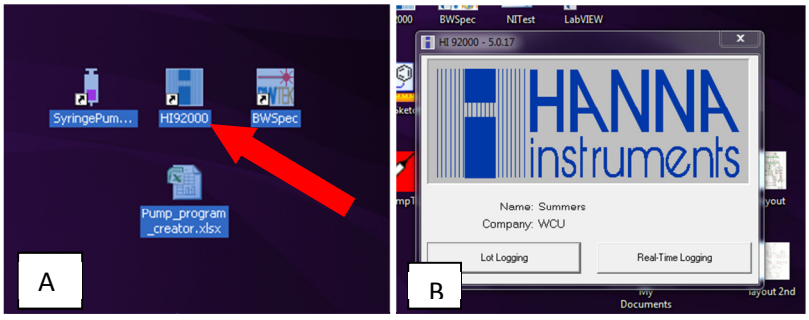

Figure 80: A) pH meter desktop icon. B) Select "Real Time Logging" for titrations.

Once open the screen looks as shown below. To adjust the communications port, baud rate, and time interval at which the pH data is taken go to the Setup tab as indicated by the red arrow below.

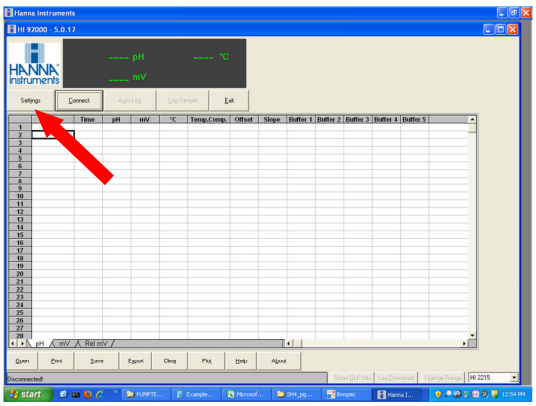

Figure 81: Select the “Setup” tab to adjust the communications port, baud rate, and time interval.

The Setup screen for the pH meter is shown below. There are two areas of this screen that should be adjusted: the Communications area and the Auto Log area. For the Communications area, first of all make sure the communications port is correct. If you’re not sure you can click on the “Detect Selected Instrument” button and the software will find the correct port. Next make sure the Baud rate is set to 9600.

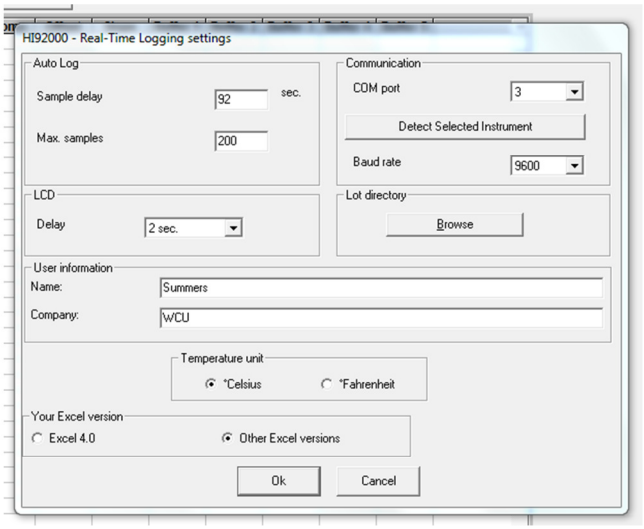

Figure 82: Setup screen for HI92000 software.

For the Auto Log area there are two options that must be adjusted. Fist the Sample delay, which is the amount of time between each pH reading. Second is the Maximum sample number,

which is the total amount of data points that will be taken. It should be noted that there is a time zero reading which should be taken into account when setting the maximum sample number. These options will need to be set to suit each titration.

Once the settings are correct hit Ok, this will bring you back to the main screen. Once ready click the Connect button (shown in figure A below). This will connect the software to the pH meter. Once connected the Auto Log button will be available (shown in figure B below). Click the Auto Log button when ready to start collecting data. This will start reading the pH (at time zero) at the selected time interval and for the selected number of data points.

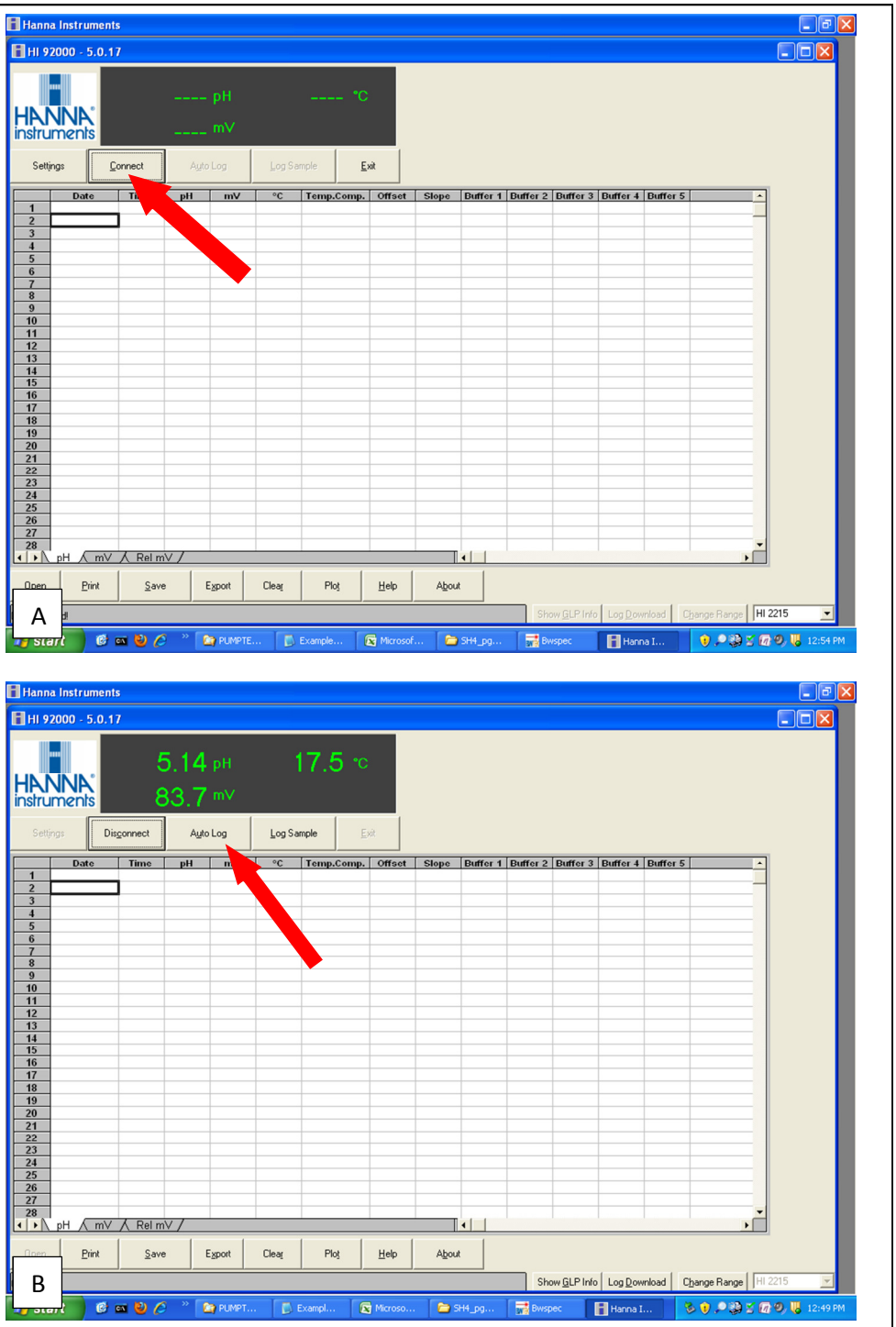

Figure 83: A) Select “Connect” once the settings in the “Setup” tab are adjusted. B) Select “Auto Log” to start logging data.

BWSPEC (UV/VIS Spectrometer)

To open the UV/Vis spectrometer click on the BWSpec icon shown below.

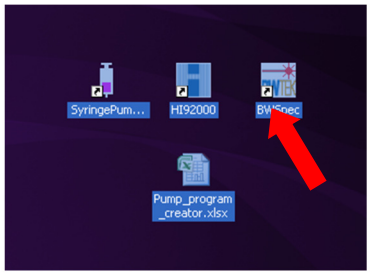

Figure 84: Desktop icon for the BWSPEC spectrometer.

Once opened the UV/Vis spectrometer looks as shown below. Befor taking a single spectra or a series of spectra for a titration there are two controls that must be set. The fist is a Dark scan and the second is a Reference scan. To set these controls use the buttons at the top-center of the screen. For the dark scan the shutter should be closed on the light source. Then simply click the dark scan button (Figure 85). Once the Dark scan is taken, open the shutter on the light source

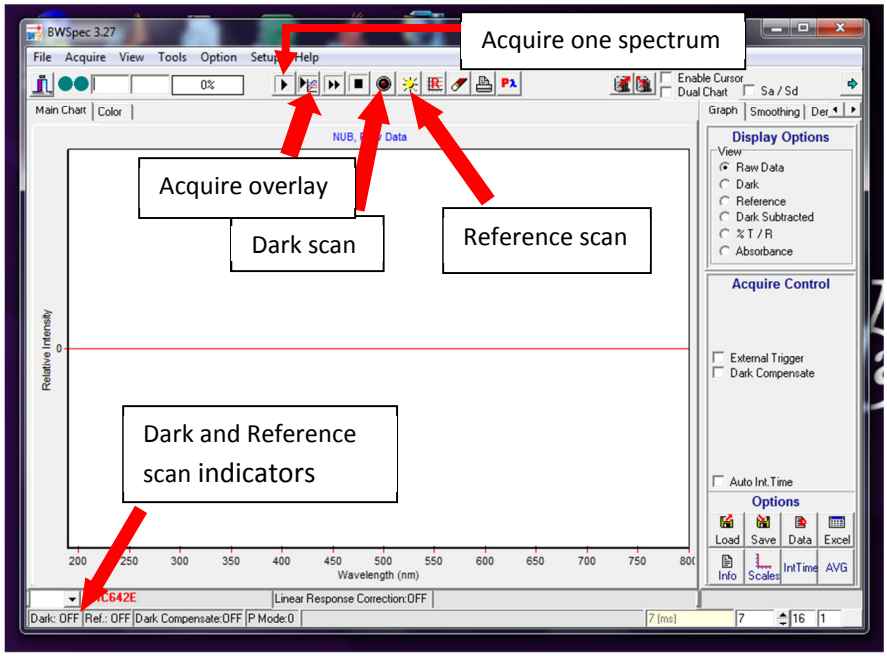

Figure 85: Software screen for the BWSpec spectrometer.

and place a cuvette with a reference solution in the cuvette holder. Then click the Reference scan button (Figure 85). At the bottom right hand of the BWSpec screen there is two indicators to let you know that the Dark and reference scans have been taken.

Once the Dark and Reference scans have been taken you can take a single scan by clicking on the Acquire One Spectrum button (shown above), take an overlaid spectrum by clicking the Acquire Overlay button (shown above), or take a spectrum at a set time interval. The third option is what will be used for titrations.

To set-up the spectrometer to acquire data for a titration go to the Acquire tab at the top right of the screen. Under the Acquire tap click on the Timeline… option (shown below).

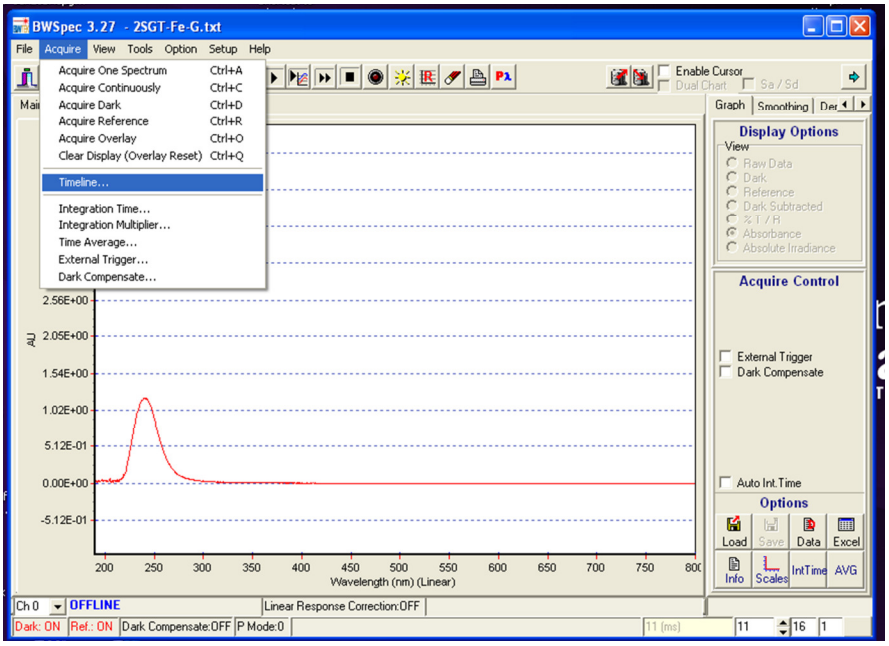

Figure 86: Select “Timeline” from the “Acquire” tab for to take spectra at a selected time interval.

Initially the Timeline window looks as shown below. Click on the green down arrow (shown below) to show more options.

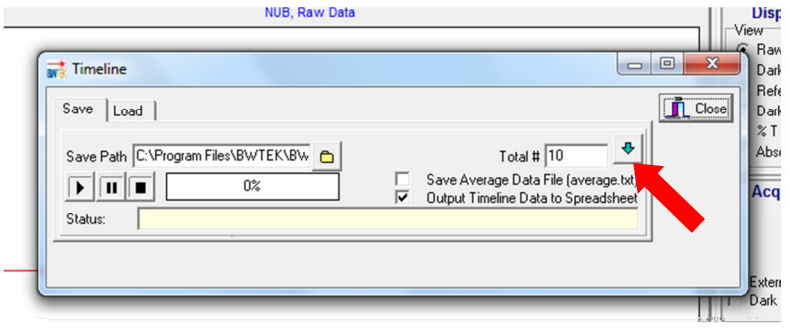

Figure 87: Select the green down arrow for more options in the "Timeline" window.

After clicking on the green down arrow, the Timeline window looks as shown below. There are four things to that should be set in this window: the Save Path, the Total #, Internal Pacer, and the Output Timeline Data to Spreadsheet check box. The Save Path is simple the location which the spectra will be saved, the Total # is the total number of spectra that will be taken (including a time zero spectrum), the Internal Pacer is the time interval between each spectrum taken, and the Output Timeline Data to Spreadsheet check box will export the spectra to an Excel sheet once all

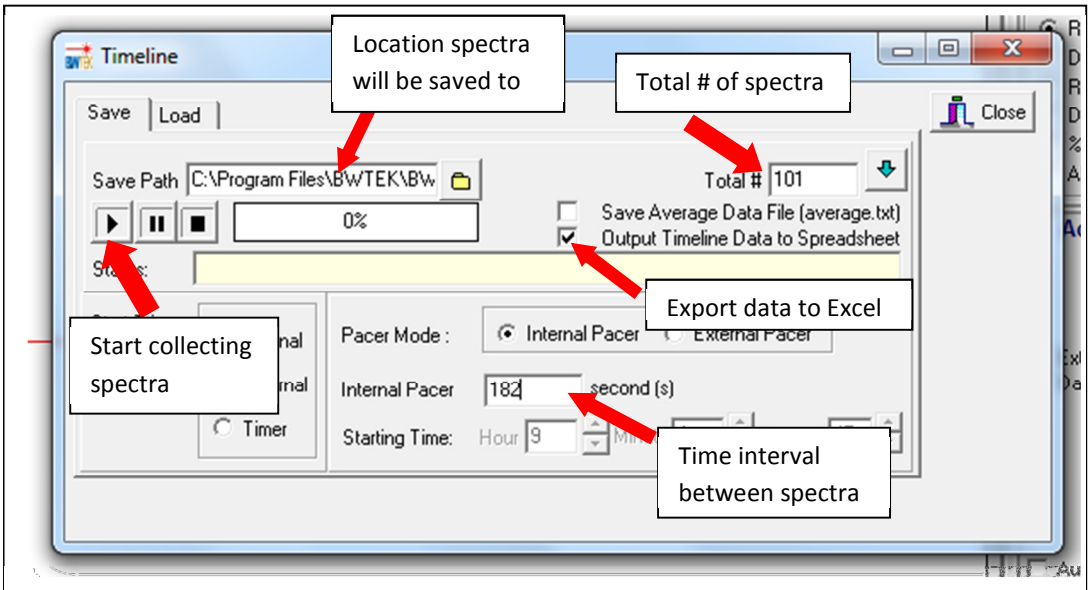

Figure 88: Settings to be adjusted in the "Timeline" window.

the data is collected if checked.

Once the Timeline settings have been adjusted the data collection can be started by clicking the go button as shown above.

Coordinating Titration Software

To run the three programs together simply coordinate the start timing of each program using a stopwatch. It is convenient to program a pause (30 seconds) initially in the pumping program to allow easier coordination of the pH meter and spectrometer.